ACOUSTIC INERTIAL CONFINEMENT FUSION:

CHARACTERIZATION OF REACTION CHAMBER

A Thesis

Submitted to the Faculty

of

Purdue University

by

Adam Butt

In Partial Fulfillment of the

Requirements for the Degree

of

Master of Science in Nuclear Engineering

December 2005

West Lafayette, Indiana

Dedicated to my parents Nasir and Patricia,

My brother Dan,

And my wife Marianne,

For their continuous love, encouragement, and support.

ACKNOWLEDGMENTS

TABLE OF CONTENTS

LIST OF TABLES

Table   Page

LIST OF FIGURES

Figure   Page

Figure   Page

Figure   Page

Figure   Page

ABSTRACT

Butt, Adam. MSNE, Purdue University, December, 2005. Acoustic Inertial Confinement Fusion: Characterization of Reaction Chamber. Major Professors: Rusi P. Taleyarkhan (School of Nuclear Engineering) and Ivana Hrbud (School of Aeronautical and Astronautical Engineering).

The purpose of the present research was to characterize existing Acoustic Inertial Confinement Fusion (AICF) reaction chambers and develop a modeling approach that could be used for preconceptual reactor design. The finite element method code FEMLAB™ was used to create a multiphysics modeling approach capable of simulating the fluid-structure interactions of existing reaction chambers. In order to validate the numerical results a series of lab experiments were performed to which the results could be benchmarked. The final modeling result predicted a chamber resonant frequency within 3% of the experimentally observed value (17.7 kHz compared to 18.2 kHz). Additionally, the multiphysics AICF chamber modeling approach was benchmarked against a similar study performed by S. Cancelos et al. at the Rensselaer Polytechnic Institute *(10)*. The developed modeling approach predicted a resonant frequency within 3% of both the RPI numerical result (using ATILA™) and experimental result. Additionally the predicted Q-value was within 13% of the RPI experimental value. The developed modeling approach was used to perform a preconceptual reactor design, with the intent of providing researchers with starting point for future scaling experiments. Using conservative values for fusion power density and experimentally determined scaling parameters, six designs were created using three different fusion reactions. Much work remains to be done and series of improvements to the multiphysics modeling approach were suggested. The

proposed reactor designs should provide a starting point to determine the experimental parameters necessary for future scaling analyses.

CHAPTER 1: INTRODUCTION

As the world's supplies of economically recoverable energy is rapidly declining and the population of Earth is both expanding and industrializing, new sources of energy need to be developed. On top of the need for a new energy source to be robust enough to cope with increasing demand, it will need to be environmentally friendly to avoid further poisoning our world. One such energy source, nuclear fusion, is considered to be nearly inexhaustible. Nuclear fusion, the reaction that powers the stars, would utilize heavy hydrogen here on Earth (also known as Deuterium) which is found in about 1 part in 6000 in the world's lakes and oceans. There is enough energy in just 1 cubic km of seawater to provide for the projected energy needs if the US for more than a thousand years. As well as a plentiful supply of energy, most fusion reactions produce less radioactive waste than fission reactions, and the resultant waste is radioactive for tens of years as opposed tens of thousands of years. Research into producing controlled fusion reactions has been ongoing for more than 50 years without success, but a new approach, Acoustic Inertial Confinement Fusion, may provide the right direction towards commercial fusion energy production.

1.1 Background on Thermonuclear Fusion

To date, all controlled net energy gains from nuclear reactions has come from fission reactions. Uncontrolled energy release from fission and fusion reactions exist in the form of the atomic bomb and the hydrogen bomb, respectively. Compared to fusion, fission is a relatively easy reaction to initiate. Room temperature or 'thermal' neutrons are all that are needed to initiate a fission reaction. With the proper amount and arrangement of moderators (such as water and boron) a fission reaction can be controlled and can be made to undergo a continuous, or chain, reaction. However, the conditions necessary for fusion reactions are more extreme. Thermonuclear fusion (a.k.a. hot fusion) is the reaction that powers the stars. At the center of the Sun temperatures can exceed $1,000,000^oC$ and the immense gravitational field can produce very high pressures. Typical reactions of interest include,

$$D + T \rightarrow {}^4He(3.5MeV) + n(14.1MeV) \tag{1}$$

$$D + D \xrightarrow{\ 50\%\ } T(1.01MeV) + p(3.02MeV)$$
$$D + D \xrightarrow{\ 50\%\ } {}^3He(0.82MeV) + n(2.45MeV) \tag{2}$$

$$D + {}^3He \rightarrow {}^4He(3.6MeV) + p(14.7MeV) \tag{3}$$
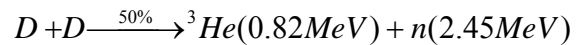
Where D and T are isotopes of Hydrogen known as Deuterium and Tritium, ^{4}He is a Helium nucleus also known as an alpha particle, n is a neutron, p is a proton, and ^{3}He is an isotope of Helium. The D-T reaction is the easiest fusion reaction to initiate because compared to other fusion reactions the lowest temperature is needed. The D-T reaction is followed by the D-D and D-^{3}He reactions. The D-D reaction is usually chosen as the first reaction explored in a research program because the fuel, Deuterium, is relatively easy to obtain and is not radioactive (like tritium). Deuterium, or heavy hydrogen, can be found in about 1 part in 6000 in both ocean and fresh water *(3)*.

In order for a sustained fusion reaction to occur a favorable combination of three parameters must occur: Confinement time, fuel density, and temperature must be achieved or exceeded (the Lawson Criterion). It has proved to be very difficult to achieve the appropriate conditions for controlled, net energy fusion here on Earth. This is a testament to the many billions of dollars and untold research hours spent on trying to achieve these conditions over the past fifty-plus years in projects such as the ZETA machine, Stellarator, Joint European Torus (JET), Russian Tokamaks, Lawrence Livermore National Lab's (LLNL) Nova laser fusion and National Ignition Facility (NIF) programs, and the soon to be constructed International Thermonuclear Experimental Reactor (ITER). Researchers face a great challenge in recreating the conditions at the center of the Sun. Researchers lack the benefit of the intense gravitational field that provides adequate densities and confinement times. To make up for these deficiencies, temperatures in excess of $100,000,000^{o}C$ are needed to satisfy the Lawson Criteria on Earth, further complicating the problem.

Two main techniques have been pursed over the years to achieve controlled fusion reactions: 'magnetic' and 'inertial' confinement fusion. The first technique, magnetic confinement fusion (MCF), utilizes intense magnetic fields to both compress and confine the very hot plasma. The two main methods to achieve this goal are tokamaks (transliteration of the Russian words for toroidal chamber in magnetic coils) and mirror devices.

The concept behind the tokamak devices is to produce a plasma in a toroidal shaped chamber, which is wrapped with electric coils. A strong current flowing through the coils produces an intense magnetic field which focuses the plasma towards the center of the torus, compressing and keeping it away from the chamber walls. The external magnetic field induces an electric current in the plasma itself which serves to heat and confine the plasma. In actual practice this has proven to be a very difficult task, mainly due to the fact that the plasma does not like to be intensely compressed and many hydrodynamic instabilities result, preventing adequate confinement times.

The other main magnetic confinement devices, known as magnetic mirror reactors, are linear devices that utilize shaped magnetic fields that are strongest at the end points to reflect particles that would otherwise escape back to the main body of the plasma. Again, this is easier said than done. It is difficult to confine enough particles for the plasma to be dense enough to sustain the reaction.

The other major technique that has been pursued to attain controlled thermonuclear fusion is known as Inertial Confinement Fusion (ICF). Essentially, this technique relies on an imparted inertia into the fuel itself in order to compress, confine, and heat the fuel to the necessary conditions. The main approach used, also known as 'laser' fusion, incorporates a number of very powerful lasers arranged around a spherical chamber to zap tiny fuel pellets in the center of the chamber. A tiny (~1mm) frozen fuel pellet is shot to the center of the chamber and once it reaches the center all of the surrounding lasers fire at once to, as uniformly as possible, compressing the target.

If the energy imparted to the surface of the target is sufficient and the compression is uniform enough, an extremely intense spherically converging shock wave will produce the conditions necessary for fusion to occur. The major challenge to this approach is, again, the instabilities that result from non-uniform compression. Even with the 196 lasers of the NIF (capable of delivering a 500 trillion watt pulse at full power), it is analogous to trying to squeeze a golf ball to an extremely small size with a set of needles. The other main challenge when using this technique is that in order to generate sustained energy the ICF laser reactor would need to zap many targets per second (perhaps as many as 100). Unfortunately, the current refresh times for these laser systems are on the order of days to weeks, not milliseconds as would be needed.

1.2: Acoustic Inertial Confinement Fusion

In 2002 an international team, consisting of Rusi P. Taleyarkhan, C.D West, J.S. Cho, R.T. Lahey Jr., R.I. Nigmatulin, and R.C. Block, published a paper in the Journal *Science* detailing the discovery of a new approach to generating the conditions for controlled thermonuclear fusion *(1)*. The paper, entitled 'Evidence for Nuclear Emissions During Acoustic Cavitation', detailed the new approach, also known as sonoluminescent fusion, bubble fusion, and sonofusion. The necessary conditions for fusion in this approach are achieved in a similar manner to ICF. Instead of using lasers, a much more simple mechanical system is used. Hence the term acoustic inertial confinement fusion (AICF) is used to describe the process.
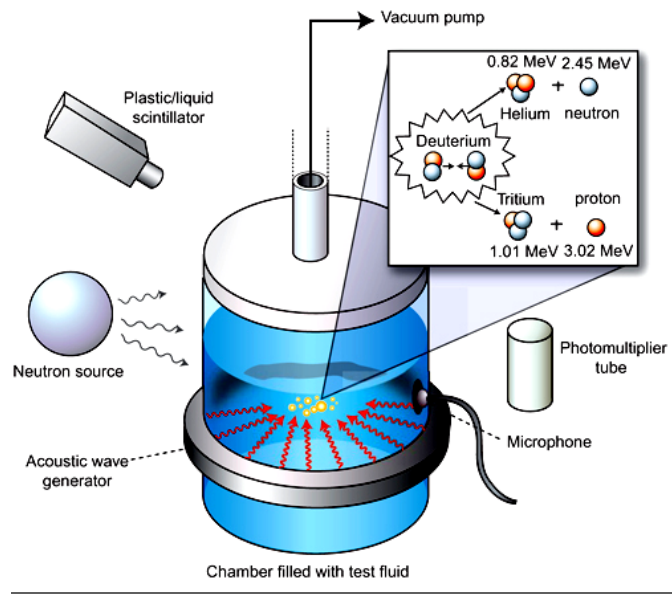
Figure 1.4: AICF schematic

During the AICF process, tiny nanometer-sized bubbles are created by nucleating a degassed fluid in a glass chamber with either neutrons from a pulsed neutron generator (PNG) or an isotopic source (such as PuBe, or Cf-252). The bubbles then expand and collapse under the presence of a very strong

acoustic field, created by a piezoelectric ring being driven at approximately 20 kHz. With the right combination of deuterated fluid, drive amplitude and frequency, and chamber geometry the result is nuclear emissions in the form of ≤2.45 MeV neutrons and the production of tritium gas. Both of those products are key signatures of deuteron-deuteron (D-D) fusion.

The driving mechanism behind this approach is similar to the ICF laser devices, except in this case the bubble walls are driven by surrounding uniform fluid-wall, allowing for intense compression and minimizing the chances of instabilities forming.

Taleyarkhan et al. recorded on the order of 10^5 neutrons and tritons being produced per second, using deuterated-acetone (C_3D_6O) and a driving power of only about 40 W (1, 2). While this level of fusion production is still well below the 10^{13} n/s needed for breakeven (as much energy produced as being expended) or 10^{15} n/s needed for a commercial reactor, it still indicates a tremendous amount of potential, given the simplicity of the design and approach. The main factor involved in the production of energy in AICF is the temperature at which the compressed core of the bubble reaches.

The amount of fusion energy produced is dependant on the temperature, since the cross-section (which is the probability of the reaction occurring) is a strongly dependant function of temperature. In fact, for the D-D reaction, the fusion cross-section increases by a factor of 10^9 for a temperature change of 10 million degrees. That means that the probability of D-D reactions occurring at 10,000,000 $^\circ$C is 10^9 times greater than at 1,000,000 $^\circ$C. The main factors that affect the temperature in AICF are the sphericity and intensity of the bubble implosion. The more spherical the implosion is the better the energy will be focused to the bubble core. Further, the more intense the implosion is the stronger the resulting shock and the higher the core temperature attained.

Acoustic pressure oscillations, controlling the expansion and compression of bubbles, are the main drivers for the intensity of bubble implosion. The greater the acoustic pressure oscillations are the more the bubbles are stretched. Once the compression phase begins, the resulting implosion is that much more violent.

The main focus of this research will be to model the acoustic fields responsible for creating the conditions necessary for the bubble implosions and to determine the parameters necessary for breakeven and beyond reactors based on the AICF approach to controlled thermonuclear fusion.

1.3: Motivation for Research

Stated in the previous sections nuclear energy has many benefits over chemical energy, the primary benefit being a vastly improved energy density. Although fusion reactions are much more difficult to initiate and control than fission reactions, fusion benefits from higher energy densities and, depending on the reaction, offers the possibility of producing far fewer radioactive substances. Furthermore, the approach to controlled thermonuclear fusion, known as AICF, has additional advantages over the other proposed methods of MCF and. AICF compares favorably because it does not require a tremendous amount of supporting hardware (such as superconducting magnets and largest lasers in the world), it requires significantly less energy to initiate (it relies on simple mechanical energy and not intense magnetic fields or laser pulses), and perhaps most importantly, it is orders of magnitude less expensive.

CHAPTER 2: RESEARCH OUTLINE

This chapter will detail the proposed research to analyze existing AICF reaction chambers and to provide the first step towards scaled designs. Previous research conducted in the area of AICF is detailed in the References *(1, 2, 9)*. At the advent of this proposed research, a substantial amount of experimental work had been done, but not much numerical work, specifically concerning the acoustics of the system. The acoustics refer to the pressure fluctuations created in the fluid as the piezoelectric ring is activated and harmonically compresses the chamber wall at a specified frequency. As previously mentioned, this harmonic compression establishes an acoustic pressure field in the fluid. Bubbles are then created (nucleated) at the location in the fluid where the compression is the highest, called the pressure anti-node. In theory, the greater the tension in the fluid, the more the bubbles will expand, resulting in a more violent implosion. The more violent the implosion is, the greater the strength of the imploding shock wave, resulting in a greater compression of the bubble core. Additionally, the higher the core temperature of the bubble is, the greater the probability of fusion reactions taking place.

The primary focus of the proposed research will be an acoustics analysis to establish a modeling approach capable of accurately simulating the varying acoustic pressure field in the fluid, based on previous and concurrent experimental research. The secondary goal of the acoustics analysis will then be to design reaction chamber models capable of predicting the necessary dimensions and conditions for the first approximation of breakeven and beyond AICF reactors.

Additional aspects of the proposed research include,

- Pressure mapping experiments against which the numerical acoustics results can be benchmarked.
- Fusion fuel analysis to determine the different system requirements needed for Deuteron-Deuteron (D-D), Deuteron-Triton (D-T), and Deuteron-Helium-3 (D-^{3}He) thermonuclear fusion.
- Shielding analysis

2.1 FEMLAB™ AICF Chamber Analysis

In order to simulate the acoustics of the experimental AICF reactors and in order to develop a modeling approach that could be used to design a next generation chamber, the finite element program FEMLAB™ was chosen. FEMLAB™ is an acronym that stands for Finite Element Modeling Laboratory. This program was developed by the Swedish company Comsol. Recently, the name of the program was changed to Comsol Multiphysics™, however throughout the body of this document it will be referred to as Femlab.

The reason this program was chosen over other finite element programs was its proclaimed ability to be able to simultaneously solve a multitude of different physics, as well as an easy to use interface. As the physics involved in the experimental AICF chambers consists of structural mechanics, acoustics, the electromagnetics of the piezoelectric, and all of their related interdependencies, Femlab was deemed a good choice to handle the modeling.

The modeling framework for Femlab consists of a number of Standard Applications Modes that include acoustics, diffusion, electromagnetics, fluid dynamics, heat transfer, structural mechanics, and a partial differential equation mode. Within each of these application modes there are more sub-modes.
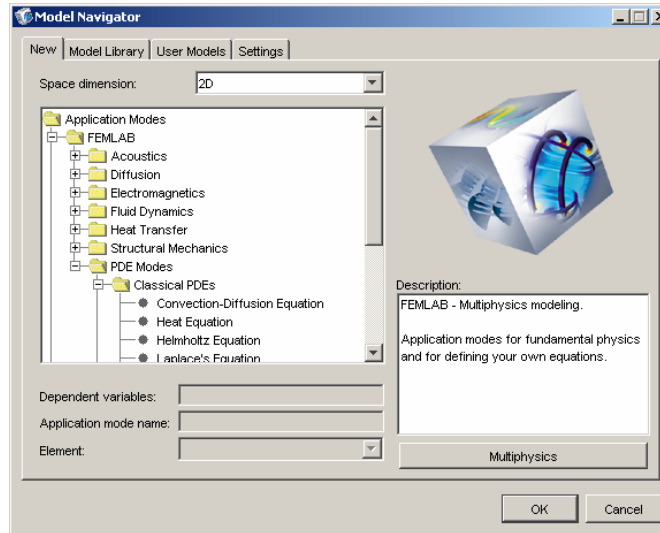
Figure 2.1: FEMLAB™ Model Navigator showing the various Application Modes
(12)

Each of the application modes and sub-modes has a predefined set of basic
equations to model that particular type of physics. Additionally, the user has the
ability to completely control and modify these equations, as well as the ability to
add more equations. There is also a built in CAD tool which allows for rapid
creation models and the ability to import geometries from various other standard
CAD programs *(12)*. Comsol has also released a number of add-on specialized
modules for Chemical Engineering, Earth Science, Electromagnetics, Heat
Transfer, MEMS, and Structural Mechanics. Each of these specialized modules
contain additional application modes specific to that type of physics. There is
also built-in support for the Matlab programming language, and an extensive
model library.

The following is a generalized list of the steps needed to create a model in FEMLAB™:

- Decide whether to model in 1-D, 2-D, 2-D Axisymmetric, or 3-D.

- Select the particular physics or set of physics needed to create the desired model. This is done by selecting one or more of the preset application sub-modes.

- Create the geometry using either the built in CAD tool or import from various other standard CAD programs.

- Define the material properties of the sub-domain(s). A model may consist of several sub-domains all with different properties, if desired. An example would be liquid flowing through a pipe, where the pipe and liquid are separate sub-domains, each with separate material properties.

- If the model consists of multiple types of physics each sub-domain needs to be specified to a type of physics that will be modeled in that particular sub-domain. For example, structural mechanics might be used to model the pipe and fluid dynamics for the liquid.

- The boundary and initial conditions need to be specified. For the above example, the pipe could be fixed on the right end and the liquid may enter through the right side of the pipe at a specified velocity.

- For a parametric analysis the parameter in question needs to be defined, in addition to the desired range and incremental step used to create solutions.

- For a time dependant analysis the range of time and time step need to be defined.

- The finite element mesh is automatically defined, but can be refined, or made more coarse, depending on the area of interest within the solution or to improve computation time.

- Any additional changes can be made to the governing equations.

- The model can now be solved. Femlab includes a number of powerful post-processing tools that can then be used to explore the calculated results.

The goal of this Femlab AICF chamber analysis is to develop a modeling framework that is capable of accurately simulating the acoustic pressure response of the fluid to the harmonic compression from the piezoelectric ring.

2.2 Pressure Mapping and Power Experiments

In order to verify the Femlab acoustic analysis results a series of experiments were performed to which the numerical results were benchmarked. A version of the experimental AICF reactor was set up so that a pressure transducer could be used to map a pressure profile along the central axis of the chamber. This was done by incrementally moving the pressure transducer along the central axis and recording the resulting pressure for a specified power to the piezoelectric ring. A map was then generated depicting the various acoustic modes of the system, including the resonant mode.

Additionally, a set of experiments was performed to determine the electrical resonance of the circuit and the actual power being delivered to the piezoelectric ring. These results were then used to help predict the performance of future systems.

2.3 Fusion Fuel Analysis

The three fusion reactions described in Eq.(1), (2), (3) were analyzed for use with the proposed AICF chamber designs. The results for all three reactions were then compared and the pros and cons of each, weighed. Additionally, a few words will be said about the engineering issues that will need to be addressed for each fuel type.

2.4 Preconceptual AICF Reactor Design

Using the multiphysics modeling approach developed from the previous chapters, a series of preconceptual reactor designs will be made. The intent of these designs will be to provide a starting point for future experimental scaling work.

2.5 Shielding Analysis

Once the appropriate designs were made for excess energy producing AICF reactors, a shielding analysis was performed to determine the thickness necessary for a shield to reduce radiation to acceptable levels

CHAPTER 3: ANALYTICAL AND EXPERIMENTAL SETUP

3.1 FEMLAB™ Setup

The finite element program FEMLAB™ was chosen to perform the acoustic analysis needed to predict chamber response and to model breakeven and beyond capable reactors. The following section will detail the various aspects of developing a FEMLAB™ modeling approach that will then be extended to reactor design.

As the geometry of the experimental reactors (see Figure 1.1) is mostly cylindrical, the 2-D Axis-symmetric space dimension was chosen to simplify the modeling process. The Structural Mechanics, Acoustics, and Fluid Dynamics application modes are chosen to model various aspects of the system.

3.1.1 Application Modes

The chamber was modeled in a multiphysics approach and is essentially designed in two parts, the structure and the fluid. The structure was modeled using the Structural Mechanics Module and the fluid using the Acoustics and Fluid Dynamics Modules. The following sections are intended to provide a more in-depth understanding of the capabilities of each module and to begin building the framework for the AICF chamber modeling approach.

3.1.1.1 Structural Mechanics

3.1.1.1.1 Theory

     For a 3-dimensional structure with the deformation components (u, v, w), the relationship between strain and displacement is given by the following equation,

$$\varepsilon = \varepsilon_{el} + \varepsilon_{th} + \varepsilon_o \qquad (4)$$

Where ε is the total strain, and ε_{el}, ε_{th}, ε_o elastic, thermal, and initial strains respectively. Shear strain can be expressed in either a vector (ε_{xy}, ε_{yz}, ε_{xz}) or engineering form (γ_{xy}, γ_{yz}, γ_{xz}). Using the small displacement assumption, the normal strain and shear strain components as functions of the deformation variables are as follows,

$$
\begin{aligned}
\varepsilon_x &= \frac{\partial u}{\partial x} & \varepsilon_{xy} &= \frac{\gamma_{xy}}{2} = \frac{1}{2}\left(\frac{\partial u}{\partial y} + \frac{\partial v}{\partial x}\right) \\
\varepsilon_y &= \frac{\partial v}{\partial y} & \varepsilon_{yz} &= \frac{\gamma_{yz}}{2} = \frac{1}{2}\left(\frac{\partial v}{\partial z} + \frac{\partial w}{\partial y}\right) \\
\varepsilon_z &= \frac{\partial w}{\partial z} & \varepsilon_{xy} &= \frac{\gamma_{xz}}{2} = \frac{1}{2}\left(\frac{\partial u}{\partial z} + \frac{\partial w}{\partial x}\right)
\end{aligned}
\qquad (5)
$$

The symmetric strain tensor ε consists of both the normal and shear strain components,

$$
\varepsilon = \begin{bmatrix}
\varepsilon_x & \varepsilon_{xy} & \varepsilon_{xz} \\
\varepsilon_{xy} & \varepsilon_y & \varepsilon_{yz} \\
\varepsilon_{xz} & \varepsilon_{yz} & \varepsilon_z
\end{bmatrix}
\qquad (6)
$$

The stress in a given material is described by the symmetric stress tensor,

$$
\sigma = \begin{bmatrix}
\sigma_x & \tau_{xy} & \tau_{xz} \\
\tau_{yx} & \sigma_x & \tau_{yz} \\
\tau_{zx} & \tau_{zy} & \sigma_x
\end{bmatrix}
\quad \tau_{xy} = \tau_{yx} \quad \tau_{xz} = \tau_{zx} \quad \tau_{xz} = \tau_{zx}
\qquad (7)
$$

where (σ_x, σ_y, σ_z) are the normal stresses and (τ_{xy}, τ_{yz}, τ_{xz}) are the shear stresses for a symmetrical case. The stress-strain relationship neglecting thermal effects is,

$$\sigma = D\varepsilon_{el} + \sigma_o \tag{8}$$

The elasticity matrix D for an isotropic material is defined as,

$$D = \frac{E}{(1+v)(1-2v)} \begin{bmatrix} 1-v & v & v & 0 & 0 & 0 \\ v & 1-v & v & 0 & 0 & 0 \\ v & v & 1-v & 0 & 0 & 0 \\ 0 & 0 & 0 & \frac{1-2v}{2} & 0 & 0 \\ 0 & 0 & 0 & 0 & \frac{1-2v}{2} & 0 \\ 0 & 0 & 0 & 0 & 0 & \frac{1-2v}{2} \end{bmatrix} \tag{9}$$

where E is the modulus of elasticity or Young's modulus and υ is Poisson's ratio.

Implementation of the above equations is done through what is called the equilibrium equations, which expressed in terms of the 3-D stresses are,

$$-\frac{\partial \sigma_x}{\partial x} - \frac{\partial \tau_{xy}}{\partial y} - \frac{\partial \tau_{xz}}{\partial z} = F_x$$

$$-\frac{\partial \tau_{xy}}{\partial x} - \frac{\partial \sigma_y}{\partial y} - \frac{\partial \tau_{yx}}{\partial z} = F_y \tag{10}$$

$$-\frac{\partial \tau_{xz}}{\partial x} - \frac{\partial \tau_{yz}}{\partial y} - \frac{\partial \sigma_z}{\partial z} = F_z$$

where F is a volume force (body force). Using a more compact notation Eq.(10) can be described as,

$$-\nabla \cdot \sigma = \vec{F} \tag{11}$$

This equation is also known as Navier's equation. Substituting in the stress-strain and strain-displacement relations from Eq.(4) and Eq.(8) yields Eq.(11), Navier's equation, expressed for displacement *(12)*.

3.1.1.1.2 Frequency Response Analysis

As the AICF chamber analysis pertains to the fluid pressure response to the acoustic-structural interactions, it is important to solve the structural mechanics equations in the frequency domain. Harmonic loads are specified by three components, the value F_x, the amplitude F_{xAmp}, and the phase F_{xPh}. The equations for the steady-state response from harmonic excitation loads are,

$$F_{xfreq} = F_x F_{xAmp}(\omega) \cdot \cos\left(\omega t + F_{xPh}(\omega)\frac{\pi}{180}\right) \tag{12}$$

$$F_{freq} = \begin{bmatrix} F_{xfreq} \\ F_{yfreq} \\ F_{zfreq} \end{bmatrix} \tag{13}$$

$$\omega = 2\pi f \tag{14}$$

where ω is the excitation frequency. These equations are derived by assuming a harmonic response with the same angular frequency as the excitation load,

$$u = u_{amp}\cos(\omega t + \phi_u) \tag{15}$$

Damping is a very important aspect of a structural mechanics analysis. For transient problems Newton's second law is introduced,

$$\rho\frac{\partial^2 \vec{u}}{\partial t^2} - \nabla \cdot c\nabla\vec{u} - \vec{F} \tag{16}$$

Within FEMLAB™, Rayleigh damping *(18)* is used to model viscous damping, and specifies two damping coefficients to do so. For a single degree of freedom system, the equation of motion with viscous damping is,

$$m\frac{d^2 u}{dt^2} + \xi\frac{du}{dt} + ku - f(t) \tag{17}$$

Within the Rayleigh damping model, the damping parameter ξ is expressed in terms of the mass m and the stiffness k as,

$$\xi = \alpha_{dM} m + \beta_{dK} k \tag{18}$$

Where α_{dM} is the mass damping parameter, and β_{dK} is the stiffness damping parameter.

This second-order system can be reduced to a first-order system by introducing new variables v = (u_t, v_t, w_t)^t, such that v = (δu/ δt). Furthermore, for a frequency domain analysis, Eq.(11) can be described using complex notation,

$$u = \text{Re}(u_{amp}e^{j\phi_\alpha}e^{j\omega t}) = \text{Re}(\tilde{u}e^{j\omega t}) \quad \text{where, } \tilde{u} = u_{amp}e^{j\omega t} \tag{19}$$

$$\vec{u} = \text{Re}(\vec{\tilde{u}}e^{j\omega t}) \tag{20}$$

$$\tilde{F}_x = F_x F_{xAmp}(\omega)e^{jF_{xPh}(f)\frac{\pi}{180}}e^{j\omega t} = \text{Re}(\tilde{F}_x e^{j\omega t}) \tag{21}$$

$$\text{where,} \quad \tilde{F}_x = F_x F_{xAmp}(f)e^{jF_{xPh}(f)\frac{\pi}{180}} \tag{21}$$

$$\tilde{F} - \begin{bmatrix} \tilde{F}_x \\ \tilde{F}_y \\ \tilde{F}_z \end{bmatrix}$$

Substituting these derived complex equations into Newton's equation of motion along with the damping parameters yields the equilibrium equation for a structural mechanics frequency response analysis *(12)*,

$$-\nabla \cdot c(1 + j\omega\beta_{dK})\nabla\vec{\tilde{u}} - (\omega^2\rho - j\omega\rho\alpha_{dM})\vec{\tilde{u}} = \tilde{F} \tag{22}$$

3.1.1.1.3 Axial Symmetry, Stress-Strain

Due to the cylindrical nature of the AICF chambers, it is possible to model them using a simplified 3-dimensional approach, known as 2-D axis-symmetric. The 2-D axis-symmetric approach assumes that the geometry being modeled only varies in two of the three dimensions.
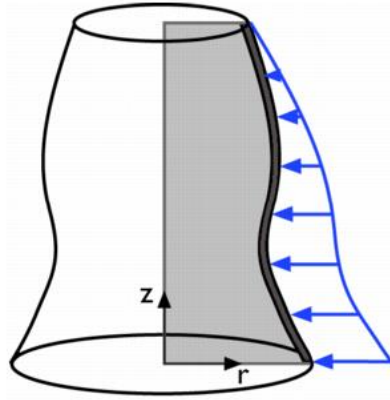
Figure 3.1: Shaded area represents a 2-D geometry used to simplify an axis-symmetric 3-D geometry *(12)*

Simplifying Eq.(10), the equilibrium equations, for the 2-D axis-symmetric case yields,

$$\frac{\partial \sigma_r}{\partial r} + \frac{\partial \tau_{rz}}{\partial z} + \frac{\sigma_r - \sigma_\theta}{r} + K_r = 0$$

$$\frac{\partial \tau_{rz}}{\partial r} + \frac{\partial \sigma_z}{\partial z} + \frac{\tau_{rz}}{r} + K_z = 0$$

(23)

Additionally, the strain-displacement relations for small displacements (Eq.(4)) becomes *(12)*,

$$\varepsilon_r = \frac{\partial u}{\partial r} \qquad \varepsilon_\varphi = \frac{u}{r} \qquad \varepsilon_z = \frac{\partial w}{\partial z} \qquad \gamma_{rz} = \frac{\partial u}{\partial z}\frac{\partial w}{\partial r}$$

(24)

3.1.1.2 Acoustics

In order to model the fluid response to the harmonic structural excitation created by the piezoelectric ring, the Acoustics module is used. A sound wave is modeled using what is known as the Wave equation,

$$\frac{1}{\rho_o c^2}\frac{\partial^2 p}{\partial t^2} + \nabla \cdot \left(-\frac{1}{\rho_o}\nabla p + q\right) = 0$$

(25)

where ρ_o is the density, c is the speed of sound, p is the pressure, and q is the dipole source. For a time-harmonic wave, where the pressure variation with time is,

$$p = p_o e^{i\omega t} \tag{26}$$

the wave equation reduces to a special form known as the Helmholtz equation,

$$\nabla \cdot \left(-\frac{1}{\rho_o}\nabla p + q \right) - \frac{\omega^2 p}{\rho_o c^2} = 0 \tag{27}$$

This equation is defined in the frequency domain, where $\omega = 2\pi f$, and is therefore the equation that will be used to model the fluid response to the harmonic structural excitation *(12)*.

3.1.1.3 Fluid Dynamics

Although the fluid in the AICF chamber is essentially static, it will be shown that the Fluid Dynamics module is necessary for developing an accurate model of the fluid (in conjunction with the Acoustics analysis). The reason for this is that Eq.(27), the Helmholtz equation, is an undamped equation and in real application, fluid damping (viscosity) plays an important role in the dynamics of any fluid response model. A common assumption made when modeling liquids is that the density does not change, also known as an incompressible fluid. This assumption is also made when using the Incompressible Navier-Stokes application mode in FEMLAB™.

This application mode uses the Navier-Stokes equations for fluid flow to solve for the pressure, p, and the velocity vector components,

$$\rho \frac{\partial \vec{u}}{\partial t} - \eta \nabla^2 \vec{u} + \rho(\vec{u} \cdot \nabla)\vec{u} + \nabla p = \vec{F}$$
$$\nabla \cdot \vec{u} = 0 \tag{28}$$

In order to allow for variable viscosity (non-Newtonian fluids) FEMLAB™ uses a generalized version of the Navier-Stokes equations,

$$\rho \frac{\partial \vec{u}}{\partial t} - \nabla \cdot [\eta(\nabla \vec{u} + (\nabla \vec{u})^T)] + \rho(\vec{u} \cdot \nabla)\vec{u} + \nabla \vec{p} = \vec{F}$$

$$\nabla \cdot \vec{u} = 0$$

(29)

Where η is the dynamic viscosity, ρ is the density, **u** is the velocity field, p is the pressure, and **F** is a volume force field (such as gravity) *(12)*.

3.1.2 Boundary Conditions

An essential aspect of any analysis is the definition of the boundary conditions. For a multiphysics analysis they can become even more important as the boundary conditions are in some instances used to couple the various physics together. The boundary conditions can be essential for communication between the different physics being modeled. This section describes the boundary conditions available to the three types of physics being modeled.

3.1.2.1 Structural Mechanics

As was discussed in Section 3.1.1.1.1, the axial-symmetry stress-strain frequency response analysis will be used to model the solid components of the AICF chamber. Boundary conditions are defined in two ways within this application mode, boundary constraint and load.

A boundary is constrained by selecting the desired boundary and applying the necessary constraint. An example would be the deformation of a beam jutting from the side of a building. The side of the beam that is 'attached' to the building wall would be constrained so it was not able to move; however, the rest of the boundaries would remain free, or unconstrained so that the beam was able to deform.

The second type of boundary condition within this application mode is a boundary load. Following the same example as above, a load could be defined across the exposed end of the beam, simulating a weight being attached to it. This load would be defined so it was in the direction of the 'ground'. Aside from defining the material properties of the beam, this model could now be solved and the resulting deformation analyzed.

3.1.2.2 Acoustics

There are a number of available boundary conditions for the Acoustics module,

1. Sound Hard Boundaries (Walls)

   - This condition specifies that the normal component of the velocity is zero on the boundary. This also means that the normal derivative of the pressure is zero on the boundary. This essentially results in a perfectly reflective boundary (idealized wall).

   - $\dfrac{\partial p}{\partial n} = 0$

2. Sound Soft Boundaries

   - This condition states that the pressure at that boundary is equal to zero. This can be used to define the boundary between a liquid and a gas where, because of the vast difference in density, the pressure wave at that interface is essentially reflected, but some acoustic information is still able to transmit through the boundary.

   - $p = 0$

3. Pressure Source

   - This boundary condition can be used to maintain a constant specified pressure, p_o, on the specified boundaries.

   - $p = p_o$

4. Impedance Boundary Condition

- This boundary condition defines the impedance, Z, at that boundary, where Z = ρ*c. This condition can be used when defining the boundary between to fluids of varying density.

- $$n \cdot \left(-\frac{1}{\rho_o} \nabla p + q \right) - \frac{i \omega p}{Z} = 0$$

5. Radiation Boundary Condition

- This boundary condition is used to define a pressure wave in a given direction. The type of wave can be selected from a menu as a plane, cylindrical, or spherical wave.

- $$-n \cdot \left(-\frac{1}{\rho_o} \nabla p + q \right) + \left(\frac{ik}{\rho_o} + \frac{R(|r|)}{\rho_o} \right) p = \frac{(ik + R(|r|) - i(k \cdot n)) p_o e^{-i(k \cdot r)}}{\rho_o}$$

6. Normal Acceleration

- This boundary condition can be used to couple with a structural analysis. The normal acceleration, a_n, represents an external source term, which can be an input from the structural analysis.

- $$n \cdot \left(-\frac{1}{\rho_o} \nabla p + q \right) = a_n$$

7. Axial Symmetry

- The boundary condition is used to define the axis of symmetry for a 2-D axis-symmetric model (at r=0).

8. Continuity

- This boundary condition states that the conditions on either side of this boundary are identical.

- $$n \cdot \left(\left(-\frac{1}{\rho_o} \nabla p + q \right)_1 - \left(-\frac{1}{\rho_o} \nabla p + q \right)_2 \right) = 0$$

3.1.2.3 Incompressible Navier-Stokes

There are also a number of available options for boundary conditions within the Incompressible Navier-Stokes application:

1. Inflow / Outflow Velocity

   • This boundary condition specifies the fluid's velocity field to simulate either an inflow or outflow.

2. Outflow or Pressure

   • This boundary condition allows the user to define a pressure that can either be used to simulate an outlet or couple the pressure to a pressure field defined in the adjacent subdomain.

3. Slip or Symmetry

   • This boundary condition states that the normal component of the velocity is zero and that the tangential component of the viscous force, K, also goes to zero.

   • $\mathbf{n}^{.}\mathbf{u} = 0$

   • $t^{.}\mathbf{K} = 0$

4. No Slip

   • This boundary condition is normally used for walls, and stipulates that the fluid's velocity equals that of the boundary, which is usually zero.

   • $\mathbf{u} = 0$

5. Normal Flow or Pressure

   • This boundary condition defines the conditions necessary for a flow field that is normal to the specified boundary.

6. Neutral

   • This boundary condition acts as if there were no boundary condition. It is basically the same thing as the continuity condition for acoustics.

3.2 AICF Chamber Multiphysics Modeling Approach

The following section will describe the multiphysics approach that was used to model the AICF chambers using the finite element program FEMLAB™. As mentioned in the previous section the application modes that were used included the Structural Mechanics, Acoustics, and Fluid Dynamics application module. Within the Structural Mechanics module, the frequency response analysis option was selected from the axial symmetry, stress-strain mode. Within the Acoustics module, the time-harmonic option was selected. And finally within the Fluid Dynamics module, the incompressible, steady-state, Navier-Stokes mode was used.

3.2.1 Geometry

The 2-D axis-symmetric geometry of the experimental AICF reactor was created using the built in CAD tool and is shown below.
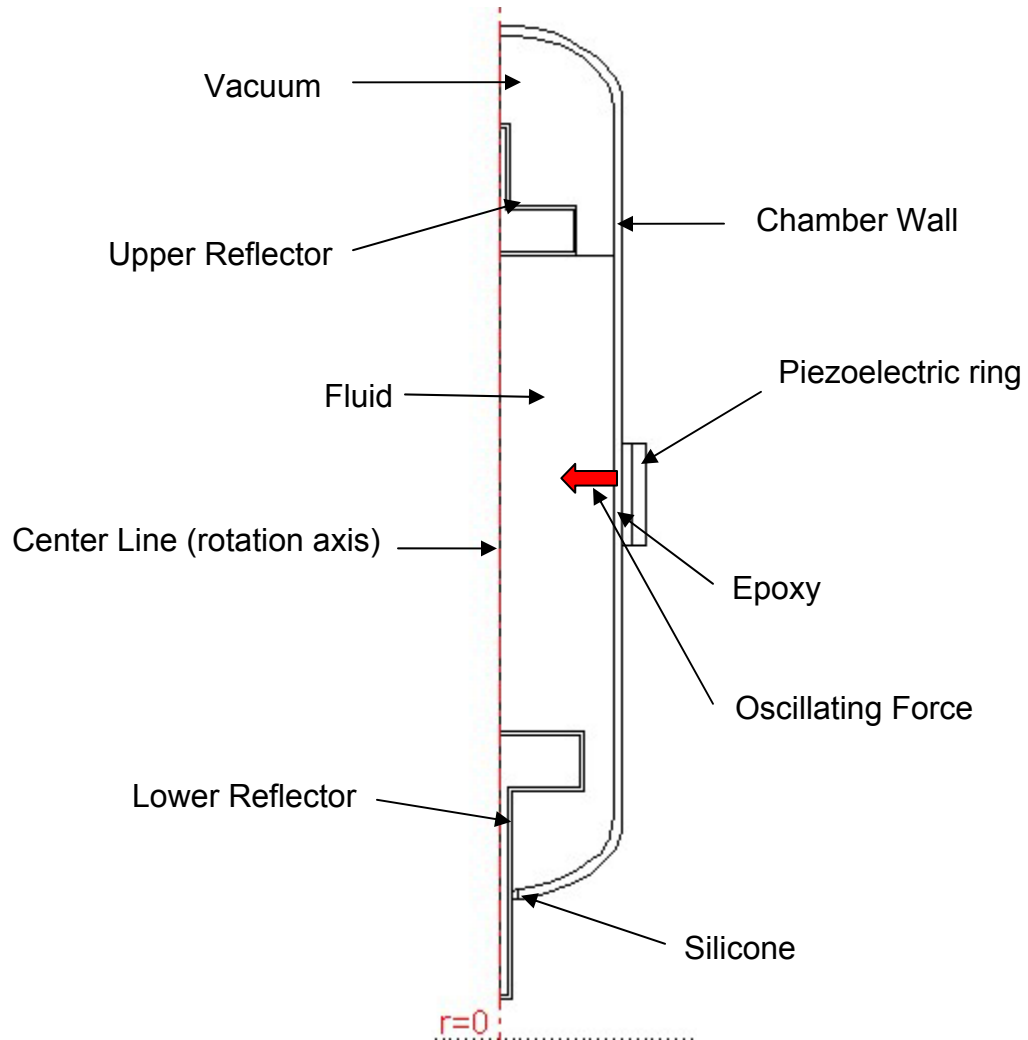
Figure 3.2: The 2-D axis-symmetric FEMLAB™ AICF chamber geometry

The upper and lower reflectors are hollow glass cylinders and are used to establish stable boundaries for the acoustic waves. The distance between them and depends on the fluid being used. In practice, the upper reflector is suspended on the surface of the fluid with a small wire, to decouple its structural response from that of the chamber wall; however, in the model it is essentially

floating on the fluid surface. Silicone is used to attach the lower reflector to the chamber, minimizes the structural coupling, and seals the bottom of the chamber. Epoxy is used to adhere the piezoelectric ring to the outside wall of the chamber.

3.2.2 Physics Settings

3.2.2.1 Structural Mechanics

The first aspect of defining any of the governing physics is to define the sub domain, or material, properties. The material properties that were used for AICF chamber modeling are summarized in Table 3.1.

Table 3.1: Material properties for structural mechanics modeling *(15, 16)*

Component	Young's Modulus [Pa]	Poisson Ratio	Density [kg/m^3]
Boron Silica Glass	73.1×10^9	0.17	2230
PZT Piezoelectric (Type-5800)	6×10^{10}	0.25	7580
RTV Silicone	9×10^7	0.485	1040
Two-part Epoxy	1×10^9	0.3	1215

The secondary aspect that needs to be defined is the boundary conditions. As per Section 3.1.1.1, the two types of boundary conditions that need to be defined for a structural mechanics analysis are the boundary constraints and boundary loads.

In the experimental setup, the AICF chamber is supported on a stand by resting on the lower portion of the piezoelectric ring (PZT). As the harmonic compression of the PZT ring is in radial direction, and there is nothing else supporting the chamber, it can therefore be assumed that the chamber can be modeled with no constraints.

As for the boundary loads, the only boundary that experiences a force is the inside of the chamber wall at the solid-fluid boundary. The forces exerted on the wall are due to the pressure fluctuations in the fluid. Therefore, the boundary load condition on the inside of the chamber walls was set to,

$$F_r = -p \cdot N_r \quad , \quad F_z = -p \cdot N_z \tag{30}$$

where F_r and F_z are the radial and axial forces acting on the chamber wall, p is the acoustic pressure, and N_r and N_z are the normal vectors. This condition stipulates that the pressure exerted on the inner wall is always normal to that wall.

Figure 3.3: Boundaries in red are those defined by Eq.(30)

By using the acoustic pressure, p, to define the force acting on the chamber wall, the structural mechanics physics were coupled to the acoustics physics.

3.2.2.2 Acoustics

The material properties used for the sub domain settings for the Acoustics module are listed in Table 3.2.

Table 3.2: Material properties for acoustics modeling *(17)*

Component	Speed of Sound [m/s]	Fluid Density [kg/m^3]
Acetone @ ~20°C (working fluid)	1175	790
Vapor Pocket (air)	343	1.23

There are three types of boundary conditions that were used for the acoustics modeling. The first was an axial symmetry condition which is defined along the center line from Figure 3.2. This condition indicates to the finite element solver that the 2-D axis-symmetric geometry is revolved around this boundary. The second type of boundary condition used was the sound soft condition from Section 3.1.2.2, which states that the pressure at this boundary is zero. This allows for the pressure waves generated in the liquid to reflect back into the liquid at that boundary, which is a safe assumption, based on the vast differences in liquid/gas density (see Table 3.2). The final boundary condition used was the normal acceleration condition. This condition is also defined in Section 3.1.2.2 and states that the change in pressure at that boundary is proportional to an acceleration of that boundary. In particular, for the AICF chamber modeling, the boundary acceleration was defined as the normal acceleration of the chamber wall,

$$\vec{n} \cdot \left(-\frac{1}{\rho_o} \nabla \vec{p} + q \right) = \vec{a}_n$$

$$\vec{a}_n = \vec{u}' \cdot \vec{N}_r + \vec{w}' \cdot \vec{N}_z$$

(31)

Where $\vec{u}$' is the structural radial acceleration, $\vec{w}$' is the structural axial acceleration, and $\vec{N}$ is the normal vector.
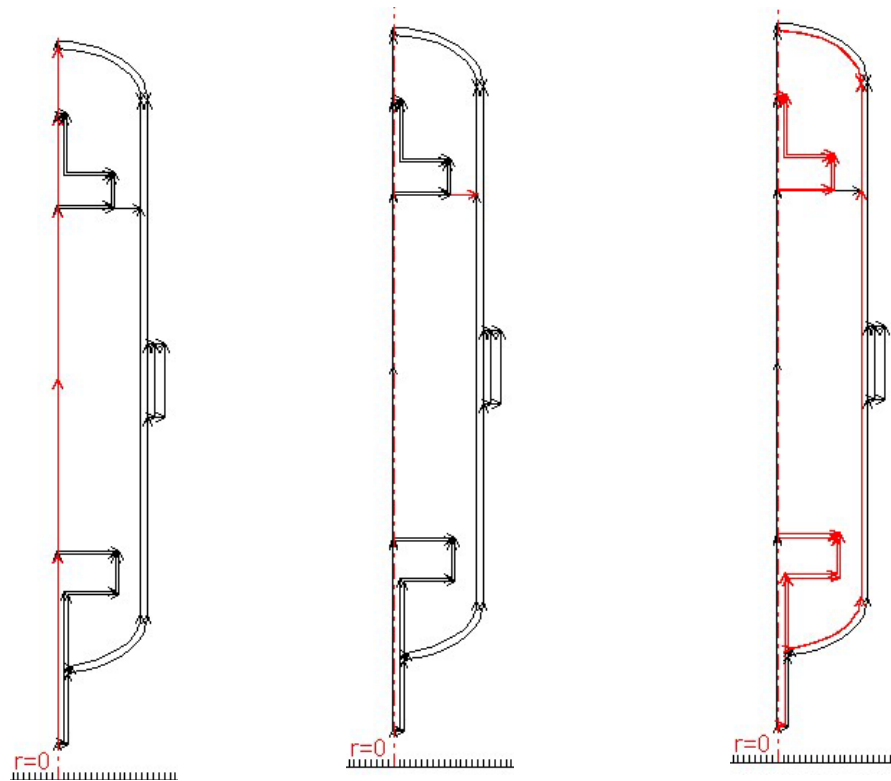
Figure 3.4: From left to right the three types of boundary conditions used for the acoustics modeling (indicated in red); axial symmetry, sound soft, and normal acceleration

The normal acceleration boundary condition also serves to couple the structural response back to the acoustic response.

3.2.2.3 Incompressible Navier-Stokes

The material properties used for the sub domain settings for the Incompressible Navier-Stokes module are defined as,

Table 3.3: Material properties for incompressible Navier-Stokes modeling *(17)*

Component	Dynamic Viscosity [Pa·s]	Fluid Density [kg/m^3]
Acetone (working fluid)	3.26 x 10^{-4}	790
Vapor Pocket	1.7 x 10^{-5}	1.23

There are four types of boundary conditions that were used for the incompressible Navier-Stokes modeling. The first is the same as the first acoustics condition, axial symmetry along the center line. The second condition used was the neutral boundary condition, defined between the liquid and gas sub domains. The third boundary condition that was used along the inside of the chamber walls and outside of the reflector walls is the normal flow/pressure condition, defined in Section 3.1.2.3. For this boundary condition an input pressure value, p_o, is defined such that,

$$\vec{n} \cdot (-p\vec{I} + \eta(\nabla \vec{u} + (\nabla \vec{u})^T))\vec{n} = -p_o \tag{32}$$

Where η is the dynamic viscosity, p is pressure, **u** is the velocity field, and **I** is the identity matrix. The value for p_o was set equal to $-p_{aco}$, which is the acoustic pressure. This essentially allows the acoustics module to calculate the pressure at the boundary, based on the structural acceleration, thus coupling the Navier-Stokes solution to the acoustics solution. The final boundary condition, which was defined on the inside of the reflectors, was the inflow/outflow velocity condition. This condition allows the user to define the velocity field at the specified boundary. For the AICF modeling approach, the radial and axial velocities (u_o, v_o) were set equal to,

$$u_o = u_s$$
$$v_o = w_s \tag{33}$$

where u_s and w_s are the structural radial and axial velocities. This condition dictates to the solver that the velocities experienced at the boundaries in question are directly proportional to the velocities caused by the deforming structure. Furthermore, this boundary condition provides coupling between the structural mechanics and the Navier-Stokes modules.
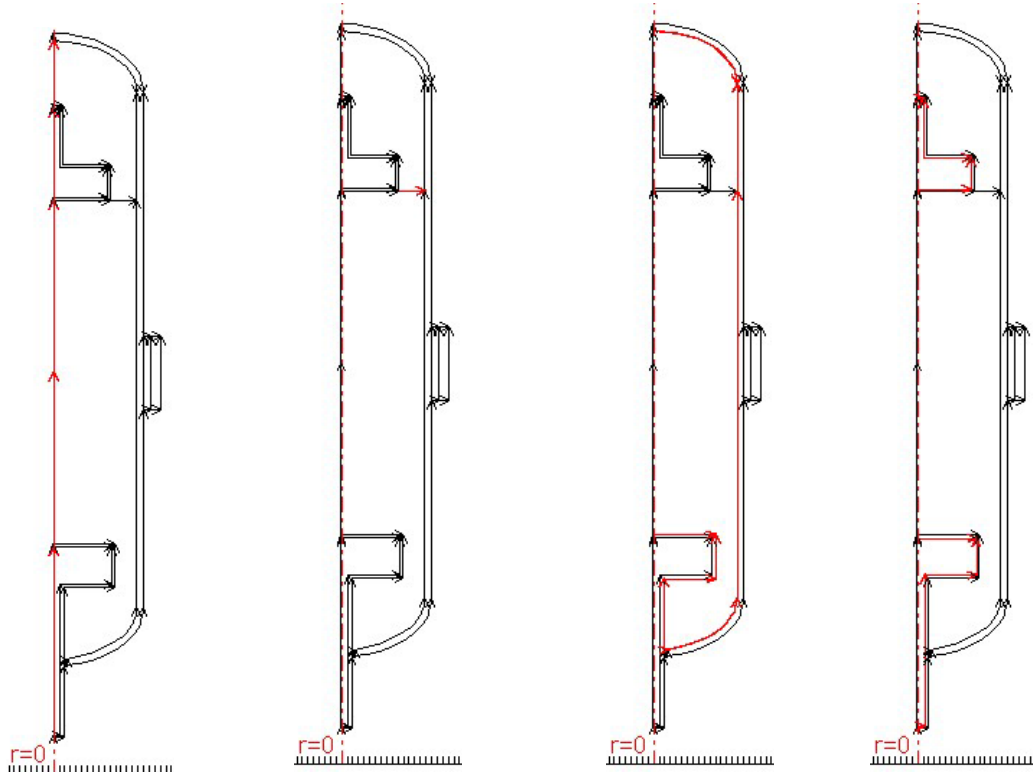
Figure 3.5: From left to right the four types of boundary conditions used for the Navier-Stokes modeling (indicated in red); axial symmetry, neutral, normal flow/pressure, and inflow/outflow velocity

Figure 3.6 below shows a summary of how the three types of physics used to model the AICF chamber are coupled together,
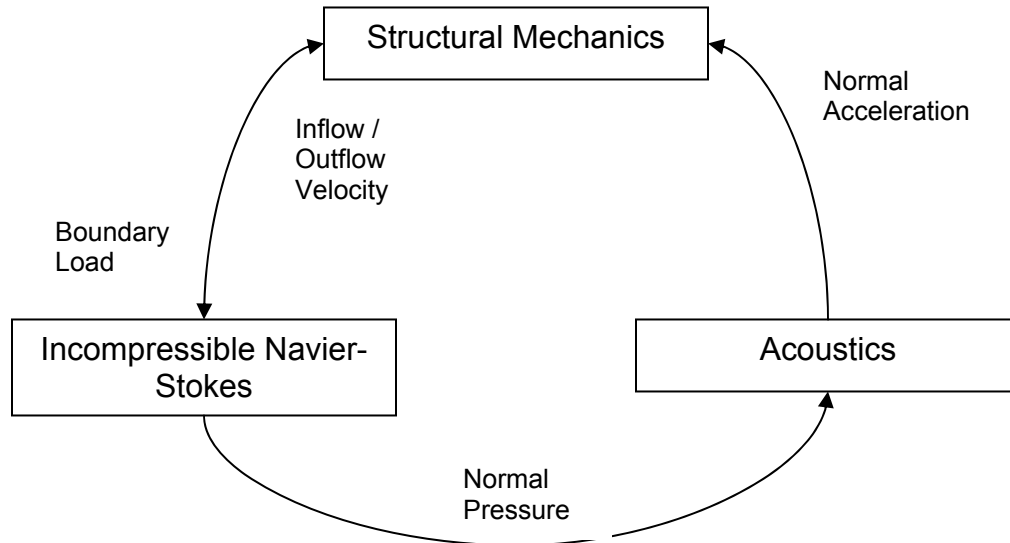
Figure 3.6: Coupling relationship flow chart

3.2.2 Piezoelectric Ring

The piezoelectric ring is a very important component of the AICF system because it provides the mechanical energy input needed to create the strong pressure fluctuations for bubble expansion and implosion. Piezoelectricity is a reversible effect exhibited by certain crystals which generates a voltage in response to a compression, or conversely compresses in the presence of an applied voltage. The acronym PZT is short for Lead (Pb)-Zirconate-Titanate, which are the materials that make up the piezoelectric ring being used for the AICF experiments (Navy Type-5800). It was decided that the PZT would be modeled as a vibrating solid, despite the capability of modeling the PZT ring with an available electromagnetics module. This greatly simplified the modeling process. The PZT ring, with the material properties given in Table 3.1, was defined as having a body force of magnitude F_x, in the radial direction. Since the solid was created in the frequency response domain, F_x varied with frequency, thus establishing the necessary harmonic driving force for the fluid-structure interactions.

3.3 Experimental Setup

In order to validate the results of the finite element analysis it was determined that a series of experiments would be necessary to benchmark the results against. The end solution of interest from the finite element analysis was the acoustic pressure response in the liquid therefore, a series of experiments were devised to map the pressure profile in the liquid based on given power input to the PZT ring.

Since it was decided not to model the electromagnetics of the PZT ring a series of experiments were also performed to measure the power input to the PZT ring as a function of frequency. The reason for these tests is, by leaving out the electromagnetics, the electrical resonances of the system would also be left out of the model. The total resonance of the real system is in fact a combination of the mechanical and electrical resonances.

3.3.1 Pressure Mapping Experimental Setup

A series of pressure mapping experiments were performed to benchmark the numerical results from FEMLAB™ with experimental data and to characterize the system resonances. The experiments were carried out by taking pressure measurements incrementally along the vertical central axis of the AICF chamber.

The equipment included a PCB S113A26 pressure transducer, a PCB 482A21 ICP Sensor Signal Conditioner, a Bogen Gold Seal Series 250 Amplifier, an Agilent 33120A Waveform Generator, and an Agilent 54624A Oscilloscope. In order to facilitate accurate incremental changes in height, the chamber, which was resting on a stand, was mounted to the work table of a drill press (with the drill removed). The work table was raised and lowered with a hand crank. For accuracy a laser tape measure was mounted to the chamber stand and a ruler was attached to a ring stand that was used to fix the pressure transducer in place. Therefore, as the crank was turned the pressure transducer and ruler remained fixed and the chamber moved up and down relative to them, facilitating incremental height measurements.

The experimental AICF chambers were cylindrical with approximately hemispherical tops and bottoms. The bottom hemispherical portion and the cylindrical portion of the chamber are all one piece, with the top being attached with silicone. In order to facilitate the use of the pressure transducer, the top of the chamber was removed for the pressure mapping tests. Additionally, the top reflector, which is attached to the top part of the chamber with fishing line, was also removed. This created two conditions which varied from the typical experimental setup, the ability to to decrease the pressure of the air above the liquid to vacuum pressures and the lack of the boundary created by the top reflector. Experimentally, the vacuum is created to de-gas the liquid prior to experimentation, removing as much of the entrained gases as possible. The more entrained gases there are the more difficult it is to create the extremely intense bubble implosions necessary for AICF *(1)*. In addition, the more de-gassed a liquid is, the more it can be tensioned. Therefore, because the liquid being used for the pressure mapping tests can not be de-gassed, the liquid can not be tensioned very far and only low drive voltages can be used for the PZT ring. Drive voltages higher than approximately 5 or 6 volts resulted in spurious cavitations at the resonant frequency. When cavitations occurred the pressure transducer data would vary considerably and thus not be useful. This may be an

important factor because the fluid-structure interaction may experience some non-linear effects at higher drive voltages. At the low drive voltages necessary to avoid cavitations, the response is essentially linear.

The other factor that differs between the pressure mapping tests and the normal experiments is the lack of the top reflector which means that the boundary conditions (where the reflector normally rests) between both tests will be different. In order to try to eliminate this as a variable, two different top reflectors were made that had holes in the middle to allow the pressure transducer to pass through. The difference between the two reflectors is the diameter of the hole the middle. Since the normal top reflector does not have a hole, an idea was formulated to plot the pressure response for the same input conditions for a case with no reflector (i.e. hole diameter equal to infinity),a reflector with a small hole, and a reflector with a larger hole. This would give three points on a plot for which a trend line could be plotted and the result for a hole size equal to zero (i.e. the normal reflector) could be extrapolated.
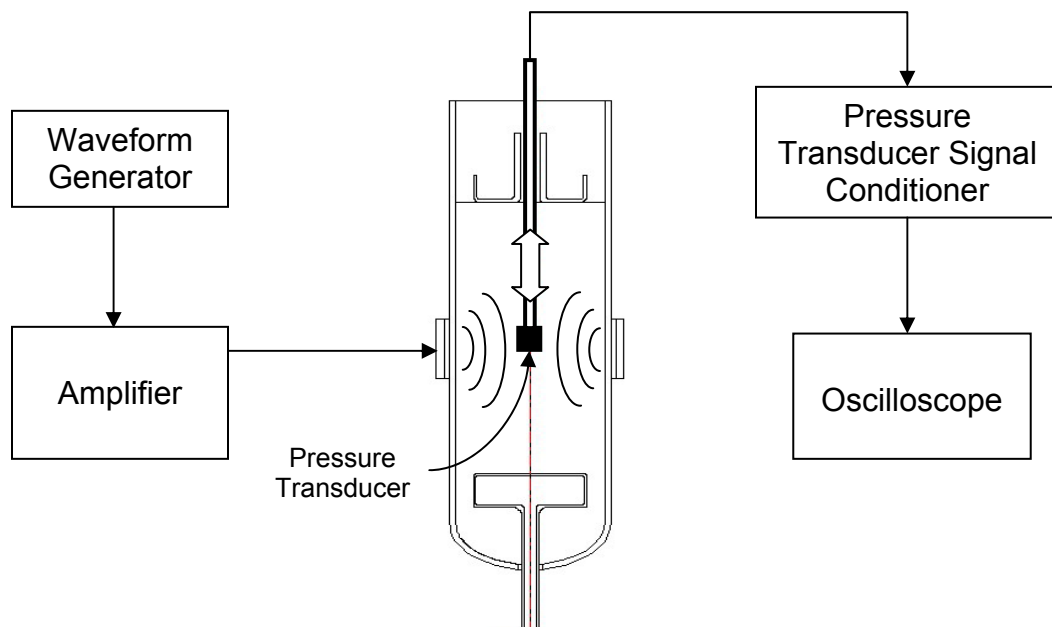
Figure 3.8: Block diagram of pressure mapping experimental setup

Initially this experiment was controlled by moving the pressure transducer to the desired depth, setting the voltage and frequency to the PZT ring on the waveform generator, and then recording the resultant pressure response on the oscilloscope. This however was a tedious process as a typical test might have consisted of twenty height steps, and around 40 frequency measurements at each step.

A computer program was therefore devised to automate the process with the hard work of Jeffery Webster and Peter Shaw, using the program Labview™.
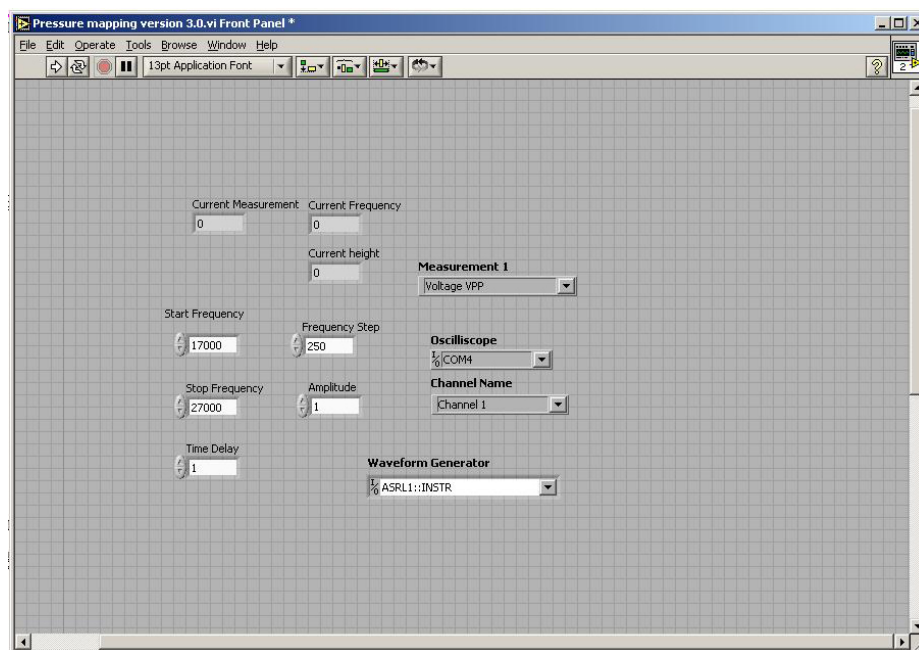
Figure 3.8: Screen shot of Labview™ program developed to automate pressure mapping tests

The program allowed the user to input the starting and stopping frequencies, in addition to the frequency step size and time delay between each step, and the drive voltage. This program interfaced with the waveform generator to control the experiment and subsequently record the pressure data to an Excel spreadsheet for easy analysis.

3.3.2 Power Measuring Experimental Setup

The power measurement experiments were performed to characterize the electrical resonance of the circuit. The end result of these tests was the power delivered to the PZT ring as a function of frequency. In order to get accurate power measurements a Valhalla Scientific Inc. 2101 Digital Power Analyzer was used. The Valhalla 2101 was wired into the circuit as shown below,
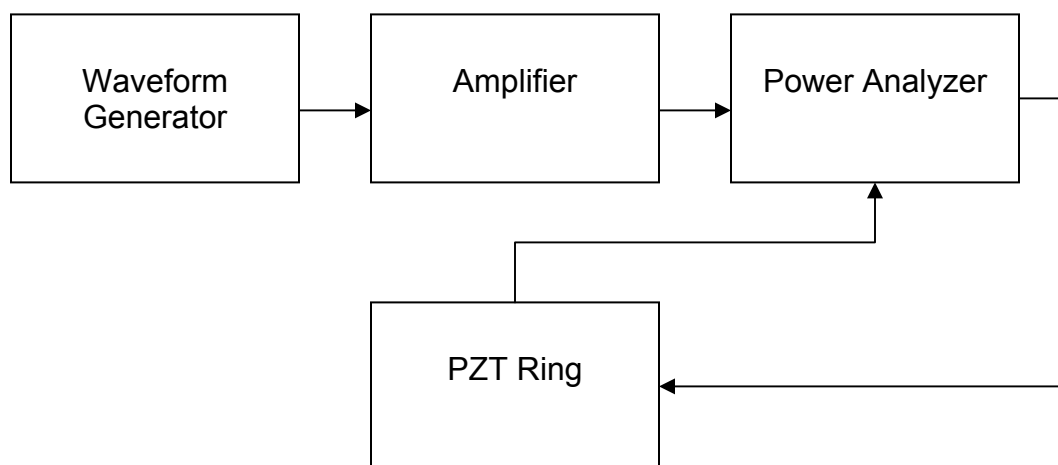
Figure 3.9: Block diagram for power measurement experiments

Since it was not necessary to use the pressure transducer for these tests, the top portion of the chamber was attached to the bottom part of the chamber and a vacuum was pulled so that the liquid would de-gas. This allowed for drive voltages as high as those used during AICF tests (~200 V, 40 W) without the disturbance caused by cavitations.

3.3.3 AICF Experiments

In addition to the above work, a series of AICF tests were performed to provide supportive data for the phenomena. The results are detailed in the two attached publications in Appendix B, and are not discussed further in this document.

CHAPTER 4: RESULTS AND DISCUSSION

4.1 AICF Multiphysics Chamber Modeling

Using the finite element platform of FEMLAB™, a series of models were created to simulate the acoustic pressure response from fluid-structure interactions, generated from the harmonic forces. The nominal experimental AICF chamber had the PZT ring oriented towards the bottom of the chamber. The main reason for this configuration was so the center of the chamber, where the majority of the bubble implosions occurred, was clearly visible. Additionally, this configuration allows for more direct placement of the photo multiplier tube (PMT) which was used to record the sonoluminescent flashes generated in the collapsing bubbles; however, since the placement of the PZT ring is not symmetric with respect to the top and bottom reflectors, the resulting pressure field is also not symmetric. It was therefore decided to both model and create an AICF chamber in which the PZT ring was placed directly in between the top and bottom reflectors, to allow for symmetry of the pressure field and simplification of the analysis.
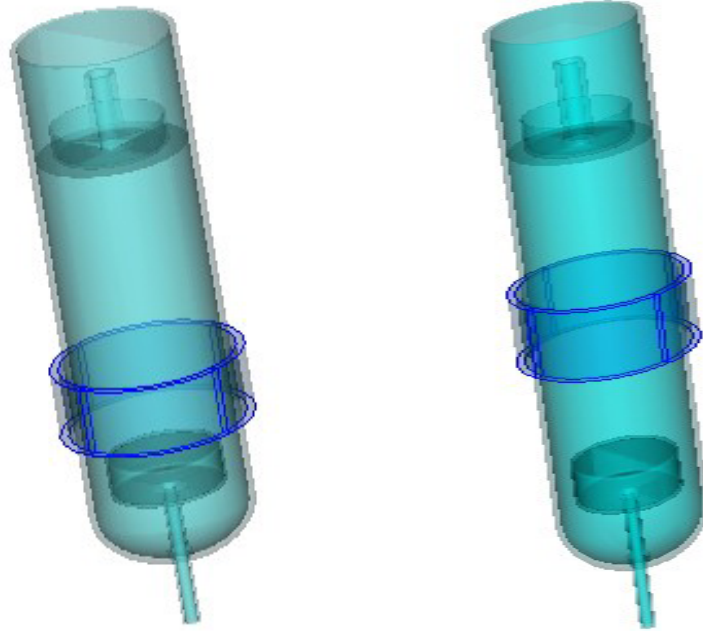
Figure 4.1: Nominal and pressure mapping chamber designs

The goal of this analysis was to create a chamber model capable of reproducing experimentally documented pressure fields. Due to the symmetrical nature of the chosen design, it was intuitively known that the largest pressure fluctuations would be at the center of the chamber (the highest point of pressure fluctuation is called the anti-node). The largest pressure fluctuation would also occur at the first system resonant frequency. It is at this frequency that the deformation of the structure is the greatest, resulting in the maximum amount of mechanical energy being converted to acoustic energy, and thus the highest pressures. The symmetrical nature also simplified the pressure mapping tests. Knowing that the highest pressure would occur at the center of the chamber, the pressure transducer could be placed there and the frequency could be rapidly swept to find the highest value, and thus the resonant frequency.

4.1.1 Chamber Modeling Progression

Initially it was anticipated that the entire fluid-structure interaction could be modeled by using FEMLAB's™ Structural Mechanics and Acoustics modules. The preliminary model, Chamber1, was created using the material properties in Tables 3.1 and 3.2 and the geometry from Figure 3.2. It was however unsure what value to use for the driving force of the PZT ring. Since a linear solver was being used, the value of the driving force would have no effect on the frequency response and mode shapes of the acoustics. The value of the driving force (measured in Newtons) would only affect the magnitude of the pressure nodes. The following results were achieved for a model with the above conditions and a driving force of 1×10^7 N,
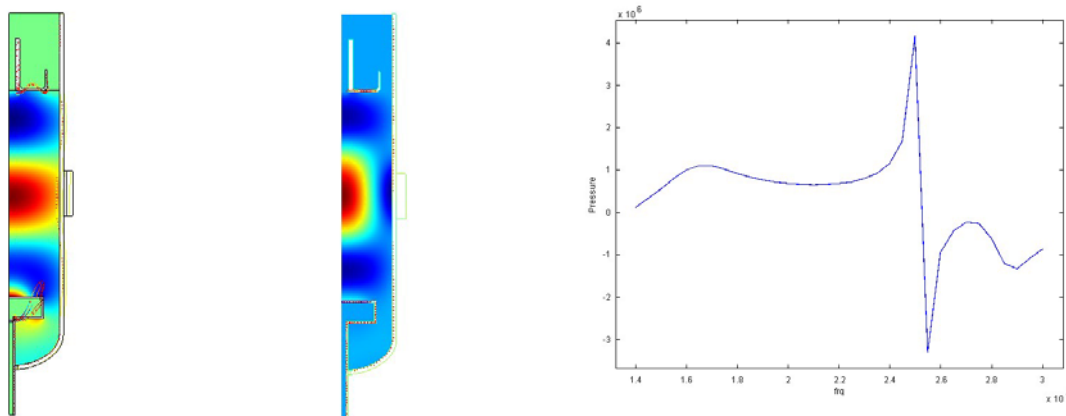
Figure 4.2: Results for Chamber1. The far left picture shows the pressure field at the resonant frequency of 16.7 kHz, the center plot shows the response at the third mode at 25 kHz, and the plot on the right shows the pressure as a function of frequency for a point located at the center of the chamber, on the central axis.

In order to determine whether these results were valid (without having compared them to the pressure mapping data) the theoretical response also needed to be determined. The harmonic compression caused by the PZT ring creates pressure waves in the liquid. These compression waves are reflected by

the top and bottom reflectors and, for a continuous oscillating input, form a standing wave between the reflectors. Due to the cylindrical geometry of the chamber there are two types of modes present, radial and axial. The first mode of a longitudinal wave, also known as the resonant mode, has one anti-node, the second mode has two anti-nodes, and the third mode has three, and so on *(32)*.

Figure 4.3: Various mode shapes for longitudinal waves

For a three dimensional wave, the frequency of a particular mode is defined by,

$$f_{mnp} = \frac{c}{2\pi}\sqrt{\left(\frac{m}{L_x}\right)^2 + \left(\frac{n}{L_y}\right)^2 + \left(\frac{p}{L_z}\right)^2} \tag{34}$$

Where c is the speed of sound, m, n, and p are the mode numbers, and L is a length. Looking at a simplified one-dimensional case, the frequency, f, can be defined as,

$$f = \frac{c}{2\pi}\frac{m}{L} \tag{35}$$

Since the geometry of the current AICF chamber is cylindrical (height to width ratio is around 4), the lower frequency axial mode ends up being the first mode of the system, and thus the resonant mode.

Therefore, the resonant mode of the system should look similar to the first axial mode, and have pressure nodes at the top and bottom reflectors and a single pressure anti-node at the center of the chamber as in Figure 4.4.
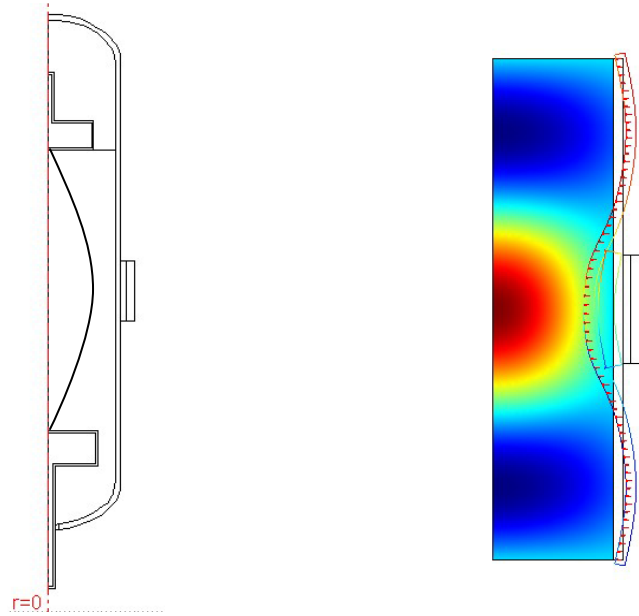
Figure 4.4: Representation of the first radial mode, which should also be the resonant mode, of the system

As mentioned previously, the resonant mode will generate the highest amplitudes with subsequent modes being of a lower value, due to losses such as structural and fluid damping. Looking now at the results from Figure 4.2, the first axial mode occurs at 16.7 kHz, the second axial mode occurs at 22 kHz, and a third mode which is a combination of an axial and a radial mode occurs at 25 kHz; When looking at the pressure versus frequency plot for the center of the chamber, the third mode exhibits the highest pressure fluctuation. This indicates based on the theory above, that the results were not correctly predicting the pressure response; however, the solutions for the various mode shapes did appear to be in line with theory.

Chamber1 lacks the proper definition of three components, one or more of which was most likely causing the discrepancy between the theory and the results. Those three components were the structural damping, fluid damping, and the characterization of the electrical resonance of the system.   The electrical resonance of the system was characterized by performing a number of experiments (see Section 4.2.1).

4.1.1.1 Determination of Structural Damping Parameters

Structural damping, modeled using the Rayleigh damping approach from Section 3.1.1.1.2, was controlled by the mass and stiffness damping coefficients, α_{dM} and β_{dK}. In order to determine a reasonable set of damping parameters a couple of simple parametric tests were performed. To determine the mass damping coefficient, the model Chamber1 was setup to be solved solely for the response at the resonant frequency. The α_{dM} parameter was then made a variable and using the parametric solver, the model was solved for α_{dM} values in the range of 0.0001 to 100, over a number of incremental steps. The solution was however invariant over the specified range, so a value of $\alpha_{dM} = 1$ was used on all subsequent models. To determine the stiffness damping parameter, a series of iterative models were used to generate solutions. The values analyzed for β_{dK} ranged from undamped ($\beta_{dK} = 0$) to 1×10^{-7}. It was found that for values greater than 1×10^{-7} the solution began to be overdamped, as the peaks of the resonant modes began to become very broad.
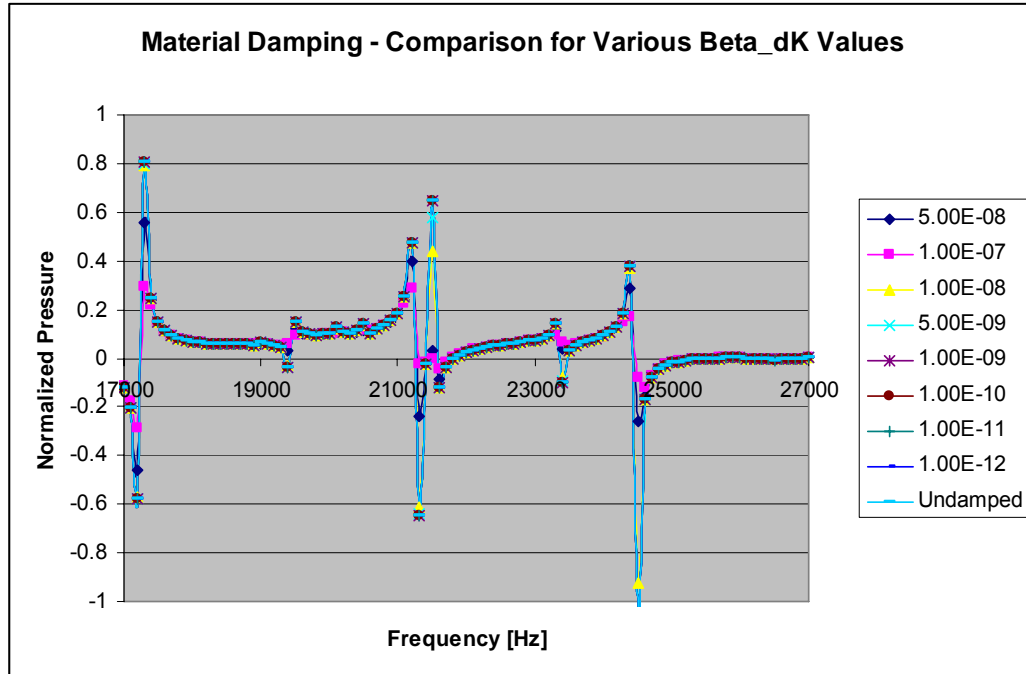
Figure 4.5: Comparison of solutions for various stiffness damping parameter
values

It was determined that the most appropriate value to use for the stiffness damping parameter was β_{dK} = 5 x 10^{-8}. There were two reasons for this selection. The first reason was that for smaller β_{dK} values the peaks began to become large in amplitude. The solutions generated for Figure 4.5 were done in 100 Hz steps. However, when the peaks were resolved at much smaller steps, it became clear that for β_{dK} < ~5 x 10^{-8} the peaks became nearly asymptotic (and thus unrealistic). The second reason was that, based on concurrent pressure mapping tests, the relative ratio of the height of the peaks to the rest of the pressure data was most closely matched for β_{dK} = 5 x 10^{-8} (pressure mapping results in Section 4.1.2). Additionally, the Q value, which is the ratio of the frequency width of a resonant peak, to the full-width half-max value also began to become unbounded (Q > 1000). Depending on how well the peak was resolved also led to higher Q values, further supporting the selection of β_{dK} = 5 x 10^{-8}.

4.1.1.2 Determination of Fluid Damping Parameters

Fluid damping (viscosity) was altogether not included in the Chamber1 model. The reason for this is that the physics controlling the fluid, Acoustics, was modeled via the Helmholtz equation, Eq.(27). This particular equation is an un-damped, frequency domain solution to the wave equation. Because there was no simple way of adding viscosity modeling to the acoustics analysis it was decided to incorporate the Incompressible Navier-Stokes fluid dynamics module. The Navier-Stokes module, as described in Section 3.1.1.3, utilizes the Navier-Stokes equations for fluid flow, in which the losses due to viscosity are included; however, since the Navier-Stokes fluid flow equation is time dependant, it can not be used solely in conjunction with the structural mechanics frequency response analysis. Therefore, the acoustics analysis had to be used in conjunction with the Navier-Stokes analysis to improve the modeling response of the fluid.

In order to determine the best way of incorporating the Navier-Stokes and acoustics analyses, a second model, Chamber2, was created. The first version of this model consisted of a simple closed cylinder completely filled with a liquid (acetone), with a PZT ring attached. This symmetric geometry and forcing would produce results most consistent with those from theory (Figures 4.3 and 4.4) and would therefore be a good starting point to incorporating the new physics. Using the property values from Table 3.1, 3.2, and 3.3, results were produced showing a comparison to using the three types of physics, as opposed to simply using acoustics and structural mechanics alone. As for the boundary conditions the normal acceleration condition was used for the acoustic-structural boundaries, and the normal pressure condition was used for the Navier-Stokes-structural boundaries. All other boundary conditions were as described in the Figure 3.6 flowchart. The force input was set at an arbitrary value and the resulting pressure values were normalized to allow for comparison of pressure response and mode shapes.
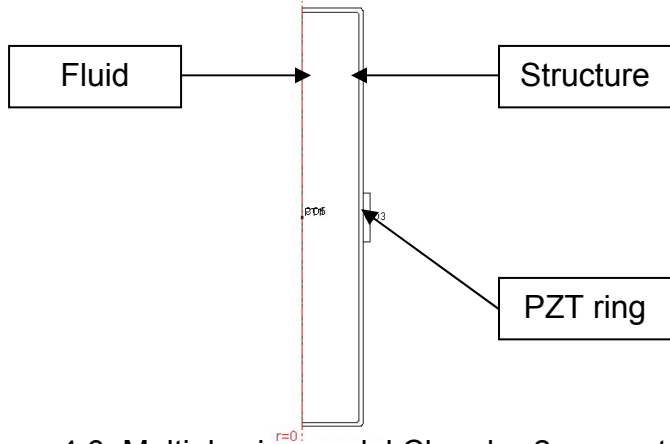
Figure 4.6: Multiphysics model Chamber2 geometry
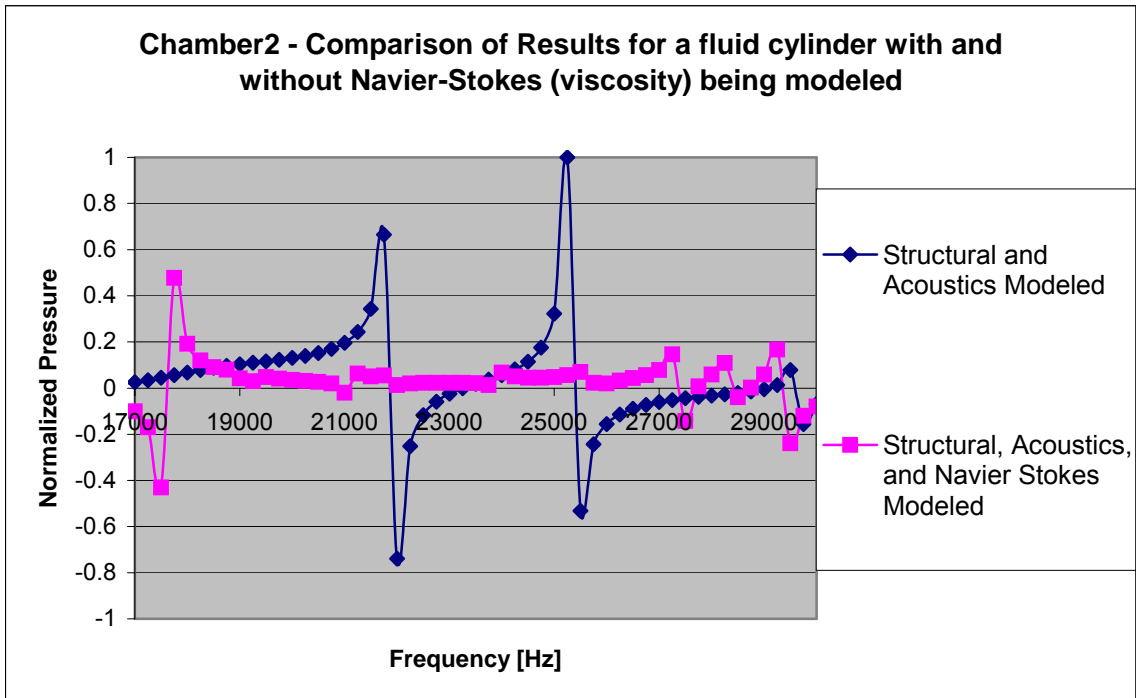
Figure 4.7: Model Chamber2 results comparison for cases with and without fluid damping

Figure 4.7 shows the comparison of results with and without fluid damping. As expected, when viscosity is added to the model, the higher modes (2 and 3) dampen out, leaving the first mode (the resonant mode) with the highest pressure amplitude.
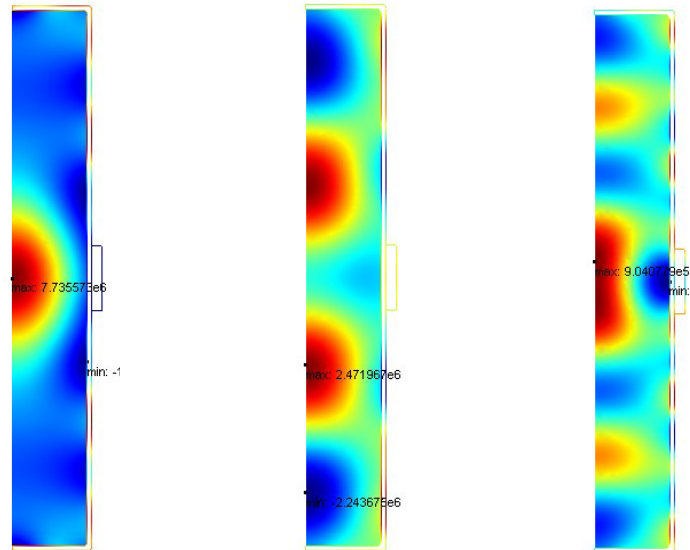
Figure 4.8: Chamber2 mode shape results at 17.7 kHz, 21 kHz, and 26.9 kHz respectively.

The mode shapes, produced from the acoustics solution as shown above in Figure 4.8, also indicate realistic results.

In order to determine the correct setup for a full AICF model, a series of intermediate models were create to determine the correct settings in a step-by-step fashion for the various components of the chamber. The additional components that needed to be added to the model Chamber2 to get to the full chamber model included the vapor gap, the top and bottom reflectors, and the addition of the silicone and epoxy, as well as the corrected chamber geometry.
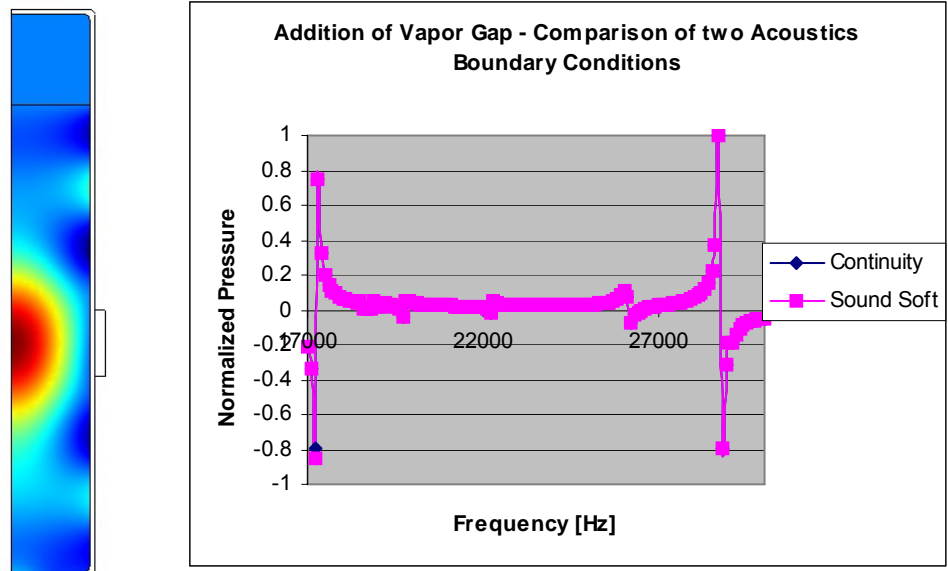
Figure 4.9: Pressure response for the addition of vapor gap and mode shape at resonant frequency (17.3 kHz)

As seen above, two solutions were generated for different acoustic boundary conditions at the liquid/gas interface. There was little difference between the continuity and sound soft boundary conditions. The sound soft condition was however chosen to be used in future models.
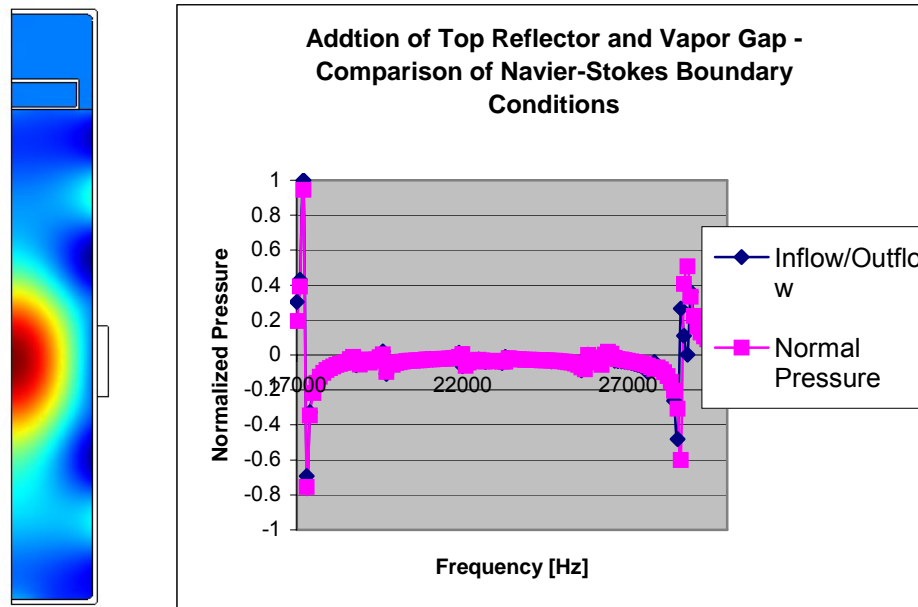
Figure 4.10: Pressure response for the addition of vapor gap and top piston and as mode shape at resonant frequency (17.3 kHz)

The next component added to the model was the top reflector. Utilizing the inflow/outflow velocity boundary condition on the inside of the reflector and the normal pressure condition for the rest of the Navier-Stokes/structural mechanics boundaries produced more consistent results. The difference between the two results is slight, but the inflow/outflow velocity condition resulted in a greater difference between the two peaks which was more consistent with the concurrent experiments. Therefore, the inflow/outflow velocity condition was chosen to govern the dynamics inside the reflectors. All other boundary conditions remained the same.
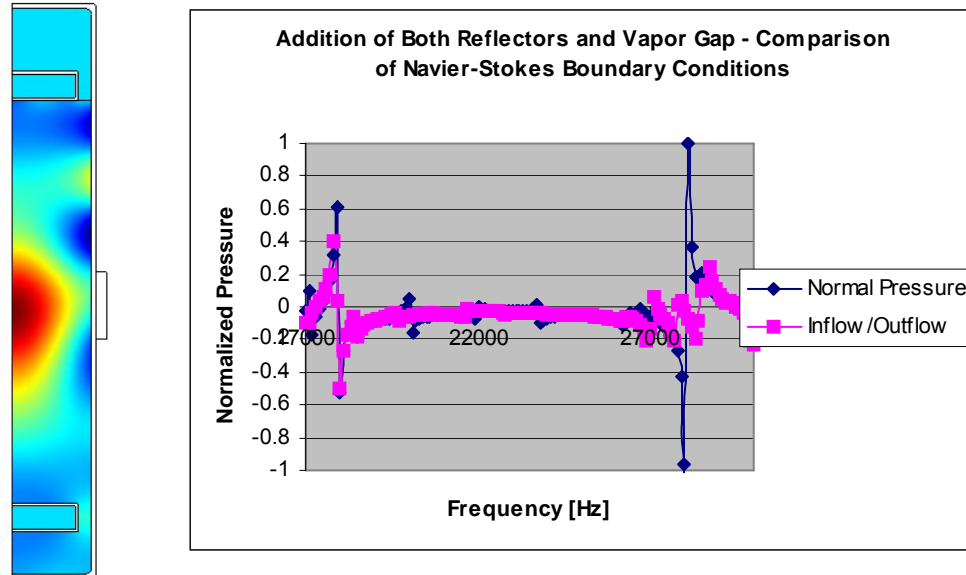
Figure 4.11: Pressure response for the addition of vapor gap and both reflectors and mode shape at resonant frequency (18.0 kHz)

After the addition of the top reflector, the bottom reflector was added. Again, following the same results as though presented in Figure 4.10, the best results were achieved when the boundaries inside of the reflectors utilized the inflow/outflow velocity condition (higher mode is more damped in comparison to the first mode). The differences between the two boundary conditions used was, however, much more distinct in this case, lending further credibility to the selection of the inflow/outflow velocity condition.
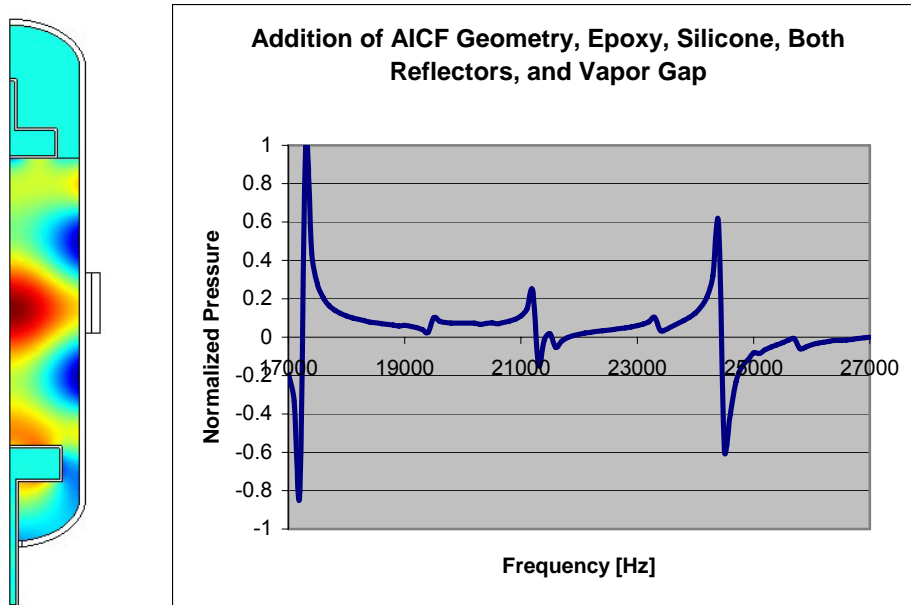
Figure 4.12: Pressure response for the addition of the AICF chamber geometry, epoxy, silicone, both reflectors, and the vapor gap. The mode shape at the resonant frequency (17.3 kHz) is plotted on the left.

The final components were then added to the model, including the AICF chamber geometry, the epoxy attaching the PZT ring to the chamber wall, and the silicone used to attach the bottom reflector and seal the chamber. The pressure response was normalized from to values from zero to one.
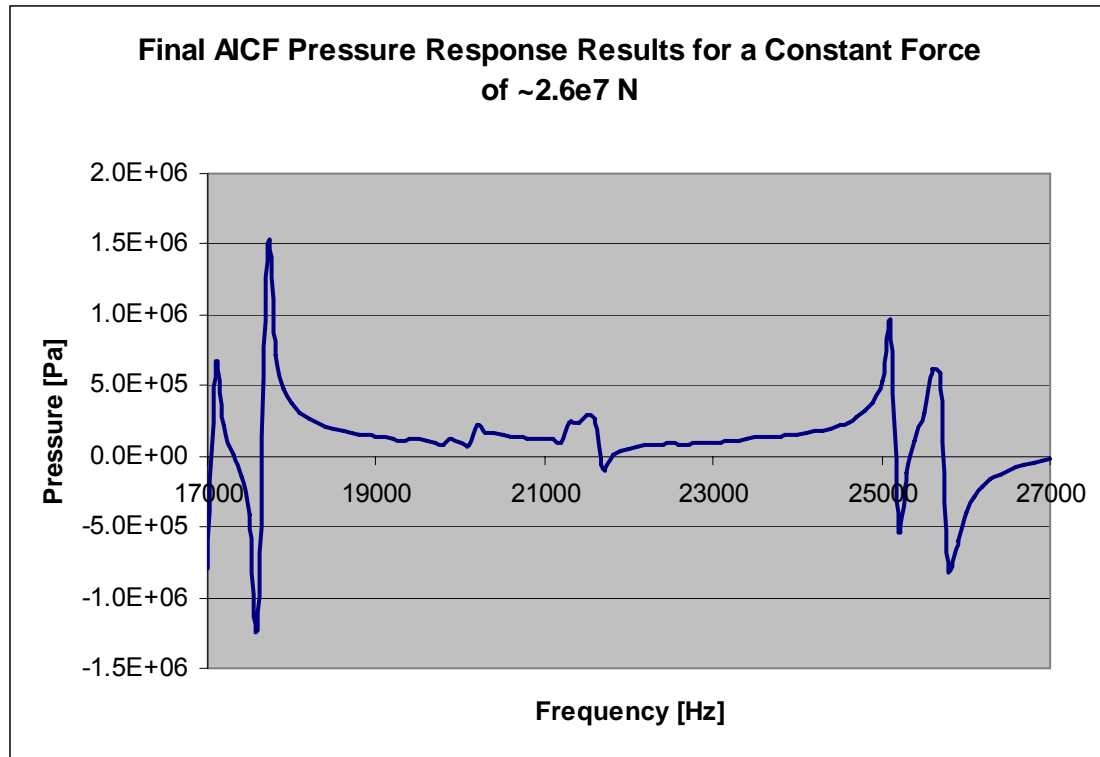
Figure 4.13: Final pressure response results

Finally, the pressure response was adjusted so that the max pressure was equal to the experimentally observed value of 15 bars. In order to achieve this, a constant force of ~2.6 x 10^7 N was used. This value would later be used to determine a coupling factor in order to determine an accurate PZT ring force. Note that two potentially important factors were left out of this modeling, the physics of the piezoelectric ring, and the reflector-vacuum coupling. During the nominal AICF tests, the reflectors are linked together via a silicone tube. The air within the reflectors is also open to the remaining air above the liquid, which is taken to vacuum pressures during tests. Due to the nature of the 2-D axis-symmetric model it was not possible for this to be modeled.

4.2 Experimental Benchmarking Results

4.2.1 Electrical Resonance Characterization

In order to characterize the electrical resonance of the experimental system a number of tests were performed to measure the power delivered to the PZT ring as a function of frequency. This is an important test to perform because every electric circuit has a resonant frequency, analogous to any mechanical system, and the combination of the two dictate the overall system resonance. For an AC circuit, the voltage V and current I can be describe as,

$$V = V_m \sin(\omega t)$$
$$I = I_m \sin(\omega t - \varphi)$$

(34)

Where V_m and I_m are the max voltage and current values, ω, is the angular frequency, and φ is the phase angle between the current and the voltage *(29)*. The average power of an AC circuit for the instantaneous values of the voltage and current is,

$$P_{avg} = VI \cos\varphi$$

(35)

Therefore, for a phase angle of 0° the power is at a maximum and for a phase angle of 90° the power is a minimum.

In order to get accurate measurements of the power being delivered to the PZT ring, a Valhalla Scientific 2101 Digital Power Analyzer was used, per Section 3.3.2.
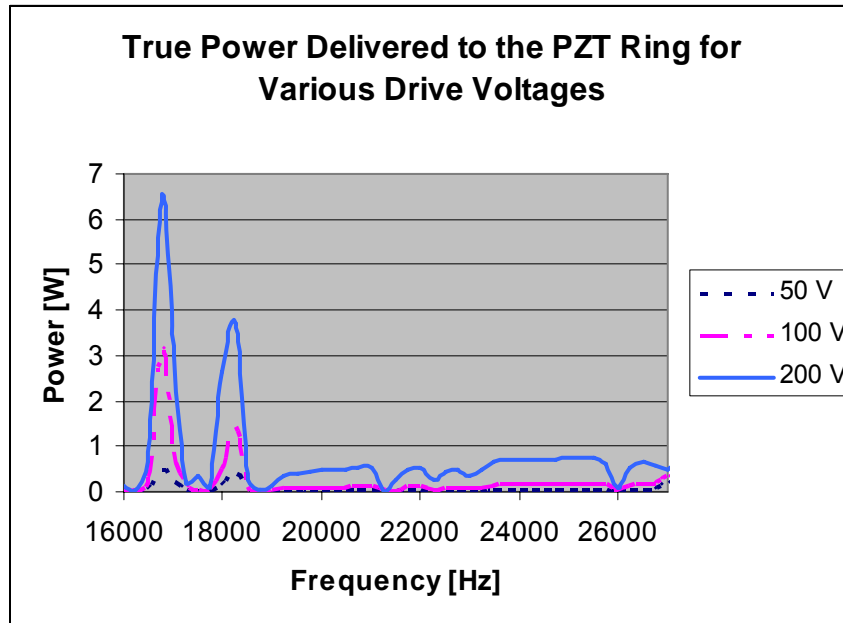
Figure 4.14: Experimental power data, characterizing the electrical resonance of the system

As seen in Figure 4.14 there are two strong electric resonances where the phase angles between the voltage and current are small (at around 16.8 kHz and 18.2 kHz). It should be noted that the manufacturer specifies that the 2101 is accurate to within ±1% up to 20 kHz, but looses accuracy at a rate of ±1% per 10 kHz thereafter.

In order to incorporate the electrical resonance characterization of the system into the multiphysics analysis, it was necessary to convert power as a function of frequency into force as a function of frequency. This is necessary because FEMLAB™ requires a force function input for the PZT ring. Force is equivalent to power divided by velocity, where the velocity in question is that of the PZT ring.

4.2.1.1 Coupling Factor k

To account for the lack of coupled fluid-structural interaction together with electromagnetics feedback, a coupling factor, k, was introduced. By using this coupling factor it was possible to arrive at the experimentally observed peak pressure fluctuations at the system resonance. This was determined for a known electrical power input. The value for the coupling factor determined to generate the experimentally observed values was $k \sim 1 \times 10^7$. Therefore, and input value of 1×10^7 N in the multiphysics model would yield a pressure of about 15 bars, at the resonant frequency of the nominal AICF chamber design.

4.2.2 Pressure Mapping Experiments

The first set of pressure mapping benchmark tests consisted of using an acoustic chamber with the PZT ring centered in between the two reflectors, as in Figure 4.1. The top reflector used was specifically designed to have a hole just large enough for the pressure transducer to pass through (about 7mm). The tests were set up per Section 3.3.1 and pressure measurements were recorded at 5mm increments from the top bottom reflector to the bottom of the top reflector. At each height increment pressure values were taken at 100 Hz steps, in a range from 16 kHz to 28 kHz, for a total of 3025 measurements. The PZT ring was driven at 4 V, which was the maximum drive voltage possible without the fluid cavitating. Even though the AICF tests were run at around 200 V, the mode shapes and frequency response of the pressure mapping tests remained similar (the amplitudes being different). The figures below show the results for the pressure response taken at the center of the chamber over the entire frequency range. The entire pressure map, plotted in three dimensions, is also shown below. Additionally, analogous plots from the multiphysics simulation are presented for comparison.
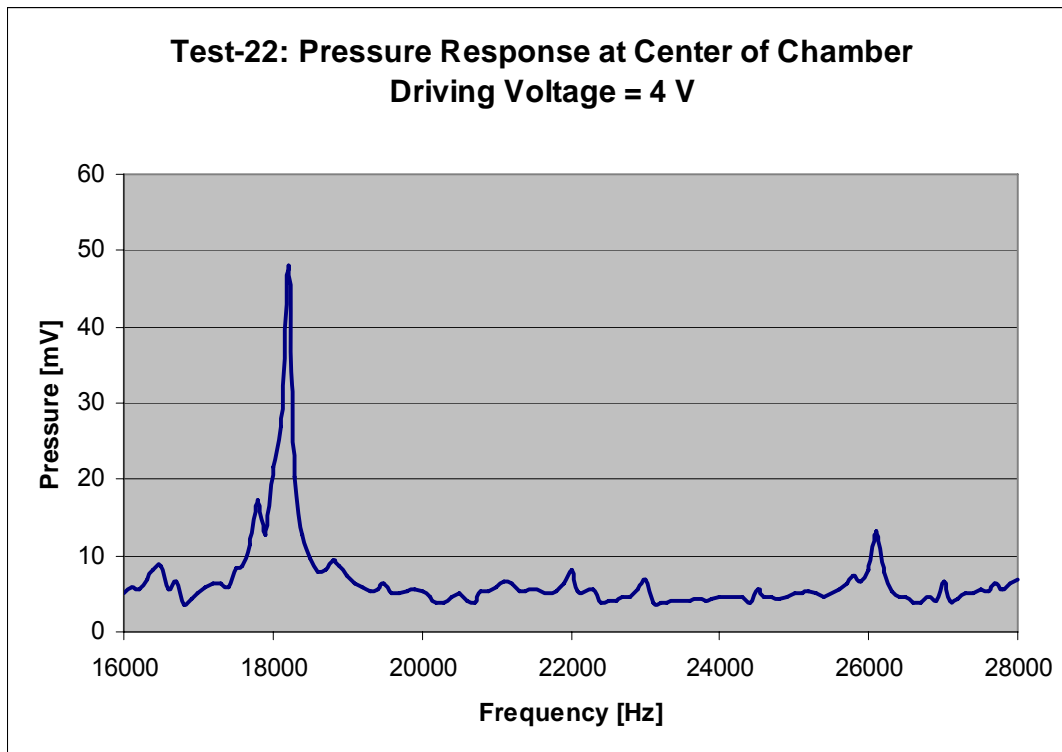
Figure 4.17: Pressure response at the center of the chamber for a 4 V input
(transducer calibration is 10 mV/psi)
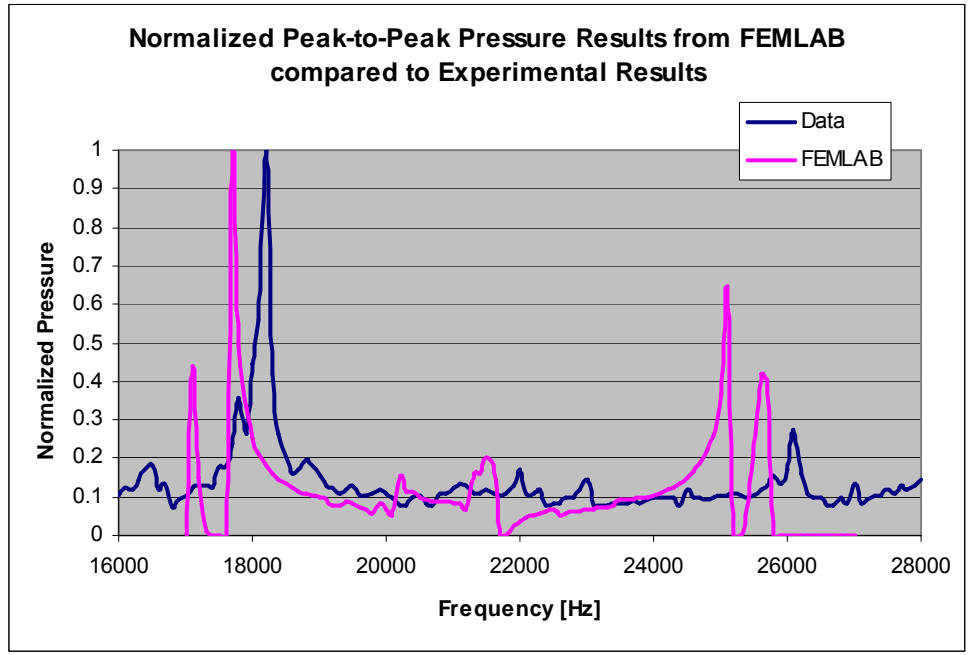
Figure 4.18: Comparison of normalized peak-to-peak pressure with experimental
data
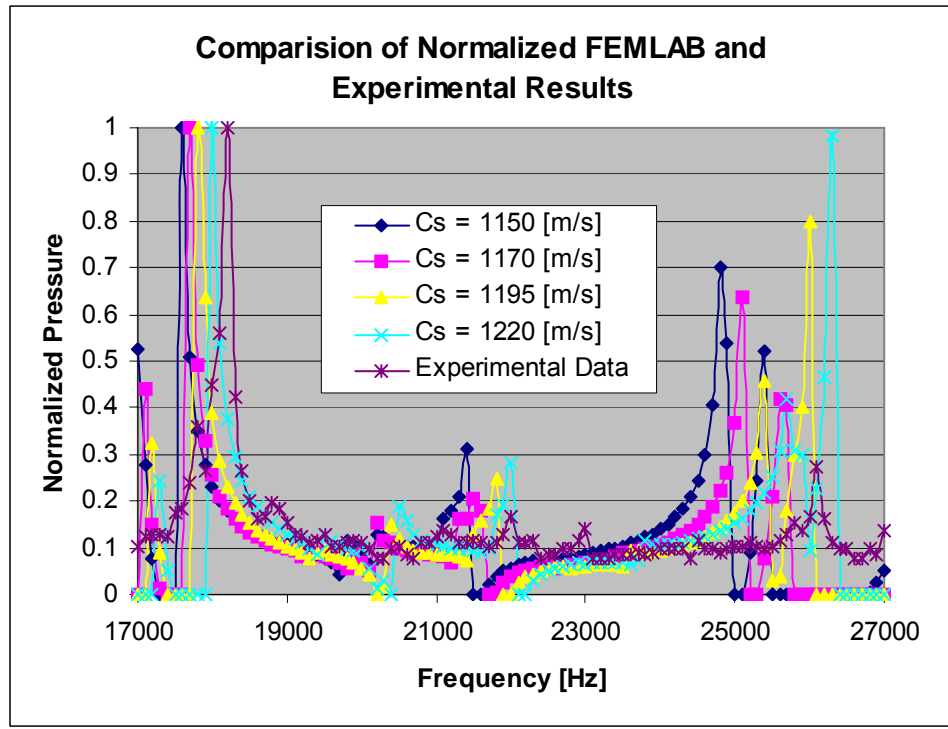
Figure 4.19: Comparison of computed pressure response for various speeds of
sound for Acetone versus the experimental data
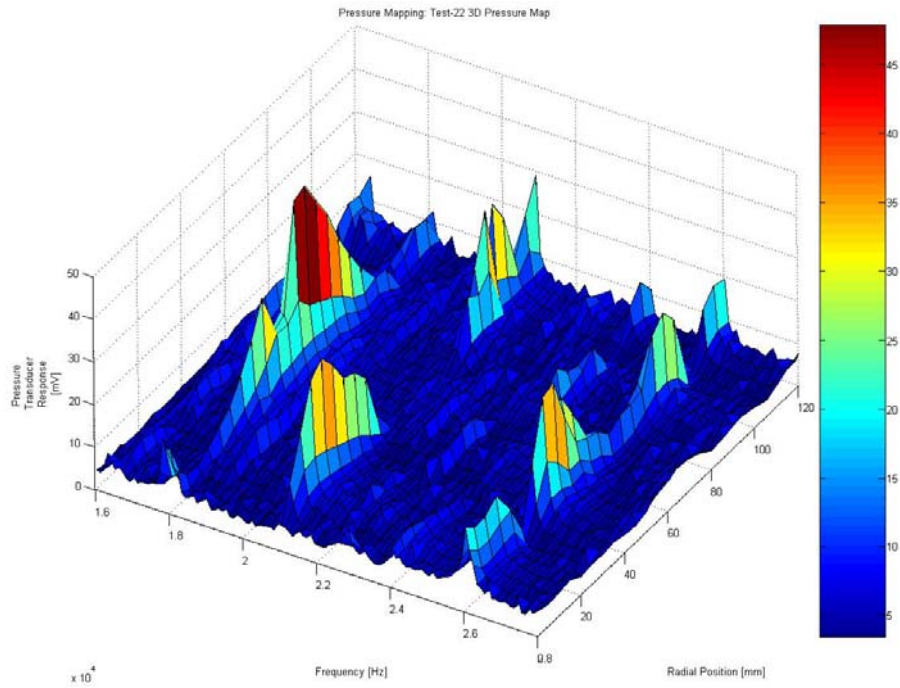
Figure 4.20: Experimental 3-D pressure map for a 4 V input
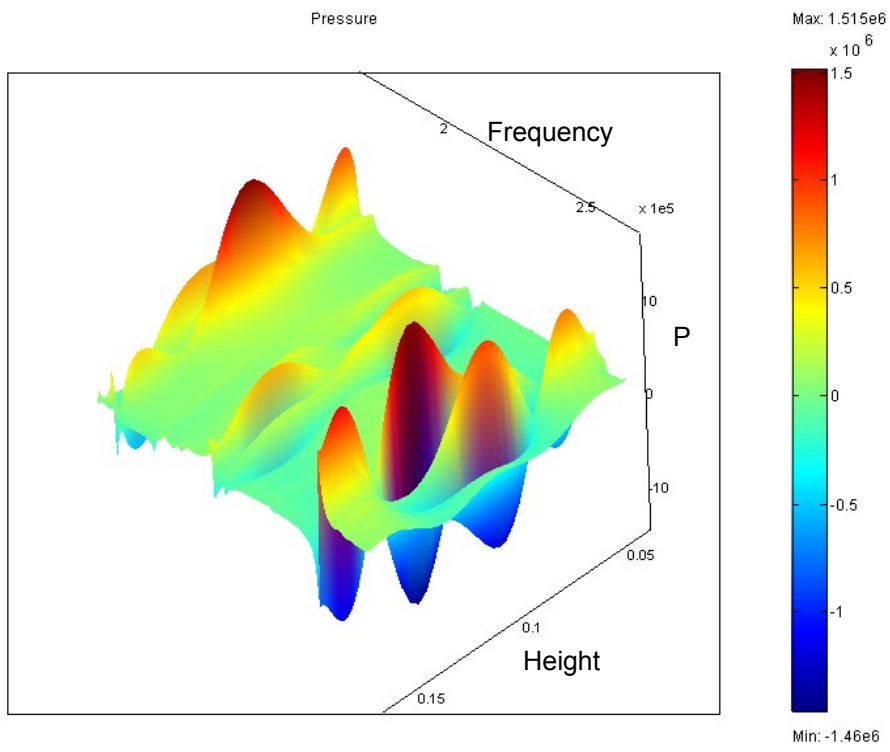
Figure 4.21: Numerical results of pressure map

Clear similarities exist between Figures 4.20 and 4.21. The resonant mode, with the large pressure peak in the center, is present in both figures at around 17-18 kHz. The second mode, with two distinct peaks, is present in both figures at around 21-22 kHz. Also the third mode, exhibiting four peaks (the two middle peaks from the numerical results are lumped together), is present in the 25-26 kHz range for both.

4.2.3 Benchmarking Against Rensselaer Polytechnic Institute AICF Chamber Study

In order to further validate the multiphysics modeling approach used an additional comparative benchmark analysis was performed. A group from the Rensselaer Polytechnic Institute (RPI) (consisting of S. Cancelos, F. J. Moraga, R. T. Lahey, Jr., and P. Bouchilloux from the Magsoft Corporation) conducted similar research which was published in a paper entitled "The Design of Acoustic Chambers for Bubble Dynamics Research" *(8)*. Their research followed the same basic path as that of this research in which a finite element method (FEM) program was used to create a chamber model suitable for AICF research. Cancelos et al. additionally performed a benchmark analysis using an acoustic chamber that was built based on their numerical results. The FEM code that they used was ATILA™, which solved for fluid/structure interaction, acoustics, and the physics of the piezoelectric materials. A comparison for this study would allow for FEM to FEM comparisons, as well as another FEMLAB™ to experimental benchmark

A new model was created within FEMLAB™ using the multiphysics modeling approach developed for this research. The material properties and dimensions were obtained from the Cancelos et al paper.
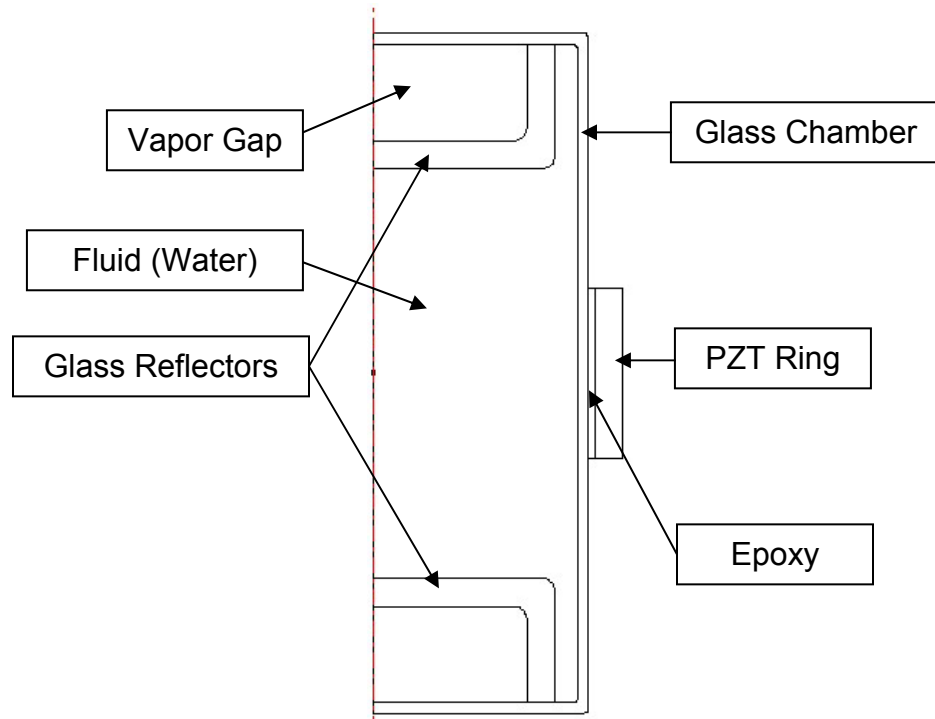
Figure 4.22: Chamber geometry for the FEMLAB™ RPI chamber model

The main difference between the two modeling approaches used was that the RPI group modeled the physics of the piezoelectric ring, whereas for this research the PZT ring was modeled as a solid oscillating with a given force. Using an input force of 1×10^7 N (coupling factor k), and the same structural damping parameters as is the previous analysis, the following results were produced for a point at the center of the chamber,
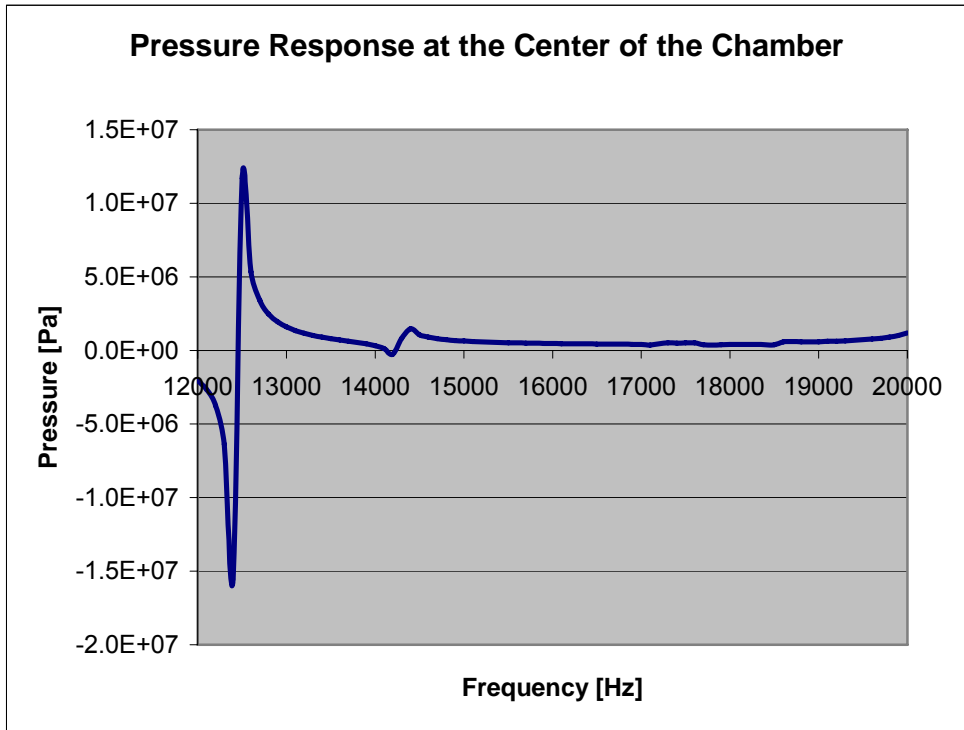
Figure 4.23: Pressure response for a FEMLAB™ version of the RPI acoustics chamber
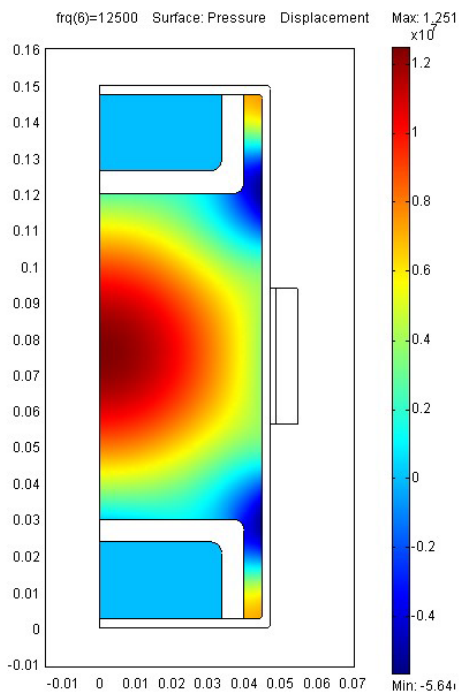
Figure 4.24: FEMLAB™ RPI chamber at resonant frequency of 12.5 kHz

Figure 4.25 shows the mode shape results for the resonant frequency, found at 12.5 kHz, and Figure 4.24 shows the pressure response over the desired frequency range. Aside from the frequency of the resonant mode, the Q-value of the FEMLAB™ results was calculated and compared to the RPI results. The Q-value is a factor which describes how 'resonant' a chamber is; the greater the value the sharper the peak and higher the amplitude. It is defined as the frequency at the peak divided by the frequency shift at the amplitude that is half of that at the peak. The FEMLAB™ results were calculated based on the data from Figure 4.23.

The table below summarizes the comparison between the ATILA™ and FEMLAB™ models, and the RPI experimental data.

Table 4.1: Results summary for FEMLAB™ and ATILLA™ RPI chamber models

Method	Resonant Frequency [kHz]	Q-value
FEMLAB™	12.52	113
ATILA™	12.678	140
RPI Experiments	12.814	127

The conclusion was that the multiphysics approach for AICF chamber modeling that was developed, appears to match with reasonable accuracy to that of an external research group. In fact this comparison was even slightly more accurate than that of the AICF comparison from the previous sections. Some of the possible reasons for this increased accuracy were that the RPI design was, in a few respects, a more simple design than the AICF chamber. The boundary conditions were more simple (no liquid/gas boundary), the reflectors were closed cavities that did not interact with one another like in the AICF chamber, and the top reflector is fixed for the RPI design (floating on liquid surface in AICF design and able to move side to side). Additionally the FEMLAB™ model could be slightly over-damped, which might account for the discrepancy in Q-values.

CHAPTER 5: PRECONCEPTUAL AICF REACTOR DESIGN

Upon completion of a benchmarked, multiphysics AICF chamber analysis, a preconceptual reactor design was performed. The goal was to get a first look at what a 1 kW, 150 kW, 500 kW, and 1 MW AICF reactor might look like, and discuss some of the issues related to real reactors of those power levels. Designs were completed at various power levels for three reactions, D-D, D-T, and D-^{3}He.

5.1 Design Approach

The approach followed for the reactor design was as follows:

1) Determine the energy released per fusion reaction, based on the reactants chosen
2) Estimate the radius, R_c, of an imploded bubble core at maximum compression
3) Estimate the confinement, or reaction, time Δt
4) Based on an estimated fusion-reactant density ρ and a given, velocity weighted reaction cross section, $<\sigma v>$, determine the number of neutrons (for D-D and D-T) or protons (D-^{3}He) produced per bubble implosion
5) Determine the energy release per bubble implosion
6) Estimate the number of bubbles produced per second, compressed intensely enough for neutron (for D-D and D-T) or proton (D-^{3}He) production

7) Calculate the amount of fusion neutron (or proton) energy produced per second

8) Determine the 'sensitive volume', within which the acoustic pressure fluctuations will be sufficient for bubble implosion

9) Determine a value for a constant neutron density which can be used as a scaling parameter

10) Size the sensitive volume necessary for 1 kW, 150 kW, 500 kW, and 1 MW power production

11) Based on the previously benchmarked AICF chamber design, determine the necessary scaled sized of the chamber at each of the power levels

Estimates for needed values were summarized in the 2004 Proceedings of the Japan/US Seminar on Two-phase Flow Dynamics, Volume 2, paper entitled, "Bubble Nuclear Fusion Technology – Status and Challenges", by Rusi P. Taleyarkhan, Richard T. Lahey Jr., and Robert I. Nigmatulin *(9)*. These values are summarized below in Table 5.1,

Table 5.1: Values used for AICF reactor design *(9)*

Variable	Value
Fusion Reactant Density	10^4 kg/m^3
Concentration of D-ions	0.5×10^{30} D/m^3
Weighted Cross-section	4.5×10^{-25} m^3/s
Bubble core temperature	10^8 K
Compressed Bubble Core Radius	50 nm
Confinement Time	0.5 ps

The energy released per reaction is given in Equations (1), (2), and (3) and are reprinted below,

$$D + T \rightarrow {}^4He(3.5MeV) + n(14.1MeV)$$

$$D + D \xrightarrow{50\%} T(1.01MeV) + p(3.02MeV)$$

$$D + D \xrightarrow{50\%} {}^3He(0.82MeV) + n(2.45MeV)$$

$$D + {}^3He \rightarrow {}^4He(3.6MeV) + p(14.7MeV)$$
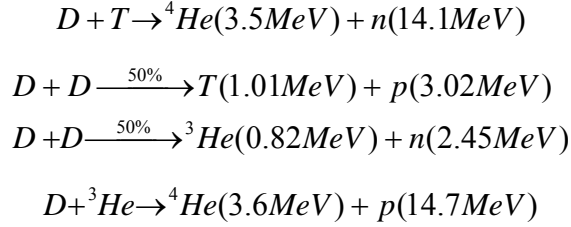
The compressed bubble core radius R_c is estimated to have an average value of 50 nm, giving a compressed core volume of about $V_c = 5 \times 10^{-22}$ m^3. The estimated confinement time based on the sources cited above is $\Delta t \sim 0.5$ ps. Following the analysis of Taleyarkhan et al. and using a well known neutron kinetics equation *(3)*, the neutron production rate for a particular reaction is estimated by,

$$\frac{dn'''_j}{dt} = \frac{1}{2}\left(n'''_j\right)^2 \langle \sigma v \rangle \tag{36}$$

Where n'''_j is the concentration of entity-j (where j = D, ion/m^3; j = n, neutrons/m^3, for D-D fusion), and $\langle \sigma v \rangle$ is the weighted cross section. The production of neutrons (or protons) per implosion is determined by,

$$n_n = \int_{t\_implosion} \int_{V\_bubble} \frac{dn'''_n}{dt} dV dt \tag{37}$$

The solution to this integral can be estimated by using the Mean Value Theorem resulting in,

$$n_n \sim \left(n'''_D\right)^2 \langle \sigma v \rangle R_c^2 \Delta t \tag{38}$$

The neutron energy released per implosion is then,

$$E_i = \text{Neutron Energy (for given reaction, X-X)} * n_n$$
$$= (E_n)_{X-X} * n_n \tag{39}$$

In order to determine the number of neutrons produced per second, it first must be known how many bubbles, capable of generating neutrons, are produced per second, n_b,

$$n_b = \text{[\# of Bubble Clusters/s]} * \text{[\# of Bubbles/Cluster]} * \text{[Cycles]} \tag{40}$$

It was found from the experiments of Taleyarkhan et al. *(33),* that it is not bubbles that are formed in the AICF chambers, but in fact tightly-packed clusters of bubbles. It was estimated that each cluster was comprised of about 1000 bubbles and that within each cluster there coalesced about 20 bubbles that were large enough to implode with the intensity necessary for fusion. Additionally it was estimated that each cluster underwent about 60 cycles before being dissolved back into the fluid, and from experimental work, about 50 clusters were formed per second. Inserting the above values into Eq.(40) yields n_b = 24,000 neutron producing bubbles per second. The number of fusion neutrons produced per second is,

$$n_f = n_n \cdot n_b \tag{41}$$

From this value the amount of neutron fusion energy produced per second if given as,

$$E_f = \left(E_n\right)_{X-X} \cdot n_f \tag{42}$$

5.1.1 Determination of Sensitive Volume

In order to develop a scaling factor to design AICF power reactors based on the benchmarked multiphysics FEM analysis, a percentage of the total liquid volume was defined as the 'sensitive volume'. This was defined as the approximate volume of the fluid, in which there was an acoustic pressure fluctuation of at least 7 bars. This pressure value is around the nucleation threshold for acetone, thus at pressures greater than or equal to 7 bars neutron producing bubbles will form.
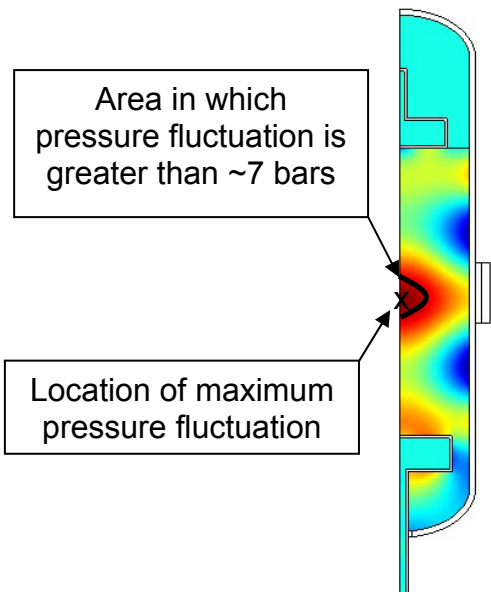
Figure 5.1: Definition of sensitive region, in which bubble cluster formation is most likely to occur
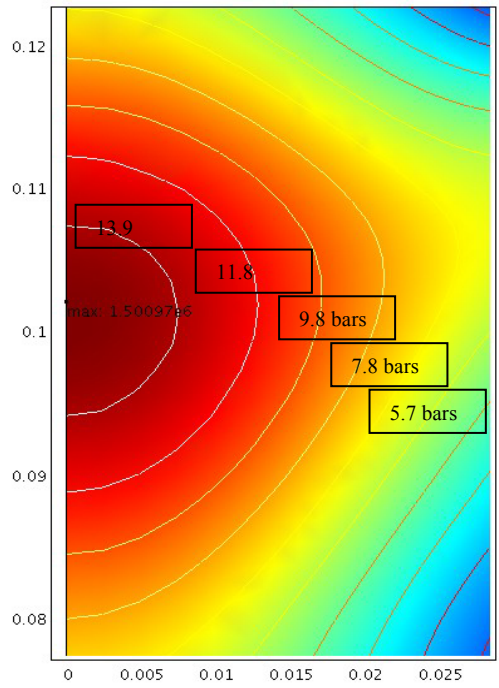
Figure 5.2: Sensitive, neutron producing region, within the fluid with indicated isobar lines

Assuming the isobars are spherical, the area indicated in Figure 5.2 of greater than or equal to 7 bars was calculated to be around 13% of the total volume (where V = (4/3)*pi*r^3, and r is determined from Figure 5.2). In order to determine a scaling parameter, the desired power level is divided by this volume to determine a series of power densities (summarized in Table 5.3 below) Designing the reactors consisted of using the same geometry as the benchmarked AICF design, determining the desired power output, and using a power density value to determine the scaled chamber size.

5.1.2 Trends and Assumptions

Using the approach described above, a series of reactor designs were created. Predicting how a newly developed concept can turn into a reality can be a very difficult proposition. Despite this, a trend was discovered during AICF testing that suggested at the possibility of being able to scale the design. What was discovered was that by increasing the amplitude of the acoustic pressure fluctuations driving the expansion and collapse of the bubbles, a significant increase in fusion neutron production was recorded *(1, 2)*. The cavitation threshold for deuterated acetone is around 7 bars. At this threshold the neutron production rate, filtered from the background, was around 10^2 n/s. By increasing the drive amplitude such that the maximum obtained pressure fluctuation was doubled to15 bars, the neutron production rate climbed by nearly 4 orders of magnitude to $10^5 - 10^6$ n/s. The reason that is believed to have caused such a significant increase is that the reaction cross-section for D-D fusion increases by nearly 4 orders of magnitude from 10^7 to 10^8 K

This experimentally observed trend was then used as the basis for further scaling and preconceptual reactor design. The assumption was that for every doubling in maximum acoustic pressure, the number of fusion neutrons produced would increase by 3 orders of magnitude. The trend line is illustrated in Figure 5.3.
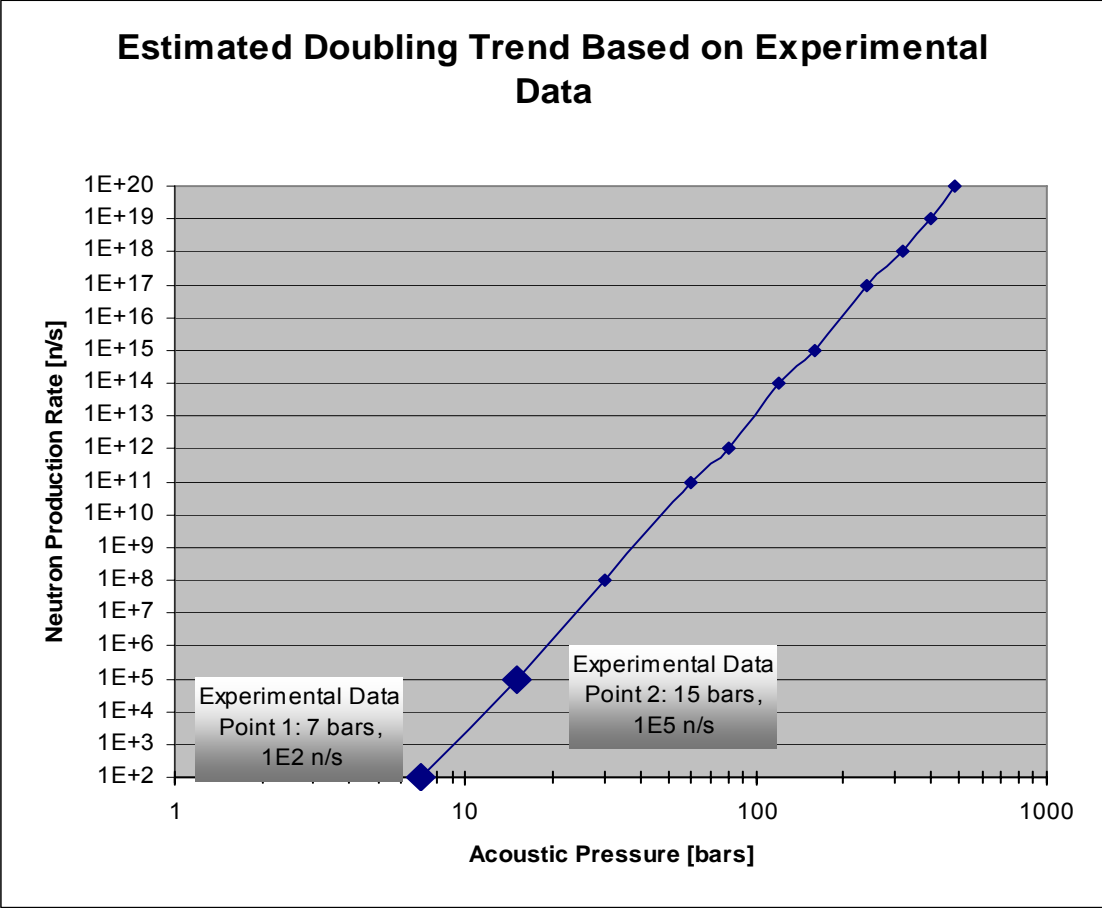
Figure 5.3: Experimentally determined neutron production trend used for preconceptual reactor design

Two different types of reactors were designed, both at various power levels, one being a 'breakeven' design and the other being a 'Q = 100' design. The value Q, known as the energy gain, is simple ratio of the fusion power produced by the reactor, divided by the power input to the reactor,

$$Q = \frac{Power_{out}}{Power_{in}} \tag{43}$$

A breakeven design is one in which the power out equals the power in. This is a very useful design for many scientific studies (including plasma physics, cosmology, and material research, etc.), as well as being the first step to a commercial reactor. The second design is what is sometimes called engineering

breakeven. The Q = 100 design generates 100 times more energy than is used to generate that energy. Even still, it is believed that it will take around a Q value of 100 to compensate for all of the other supporting hardware inefficiencies necessary to run such reactors.

Another assumption was made based on the trend in Figure 5.4. The second trend, shown in Figure 5.5, was that the bubble core temperature (in keV) also doubles in value for every doubling of maximum acoustic pressure. This assumption was important so that realistic cross-sections could be determined based on the acoustic pressure. These cross-section values were then used to calculate the neutron production rate per bubble, n_n. The resulting trend is shown below,
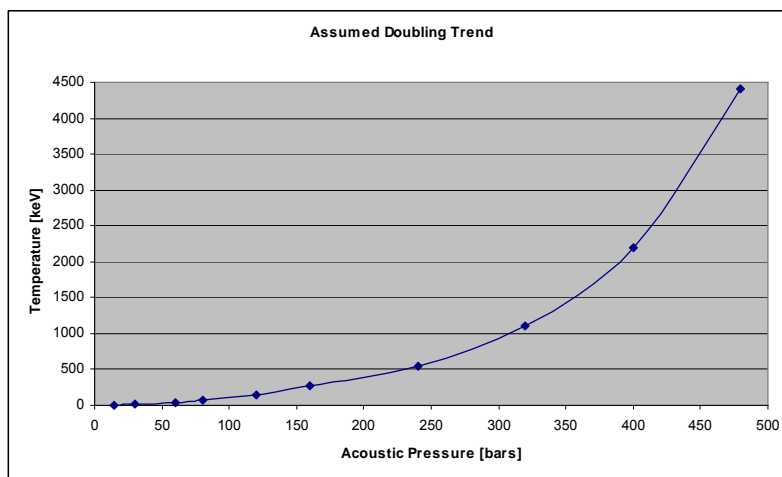
Figure 5.4: Assumed doubling trend for bubble core temperature

The third assumption that was made was that the bubble density ρ_b remained the same, regardless of the power level. The bubble density was defined as $\rho_b = n_b/V_s$, where n_b was the number of neutron producing bubbles formed per second and, V_s, was the sensitive volume. This value was calculated to be 2.17×10^{10} bubble/m³*s from the values in Table 5.1.

Table 5.2: Summary of Assumptions used

Assumption	Value
Neutron production to P_{aco} doubling trend	Figure 5.3
Bubble core temperature to P_{aco} doubling trend	Same trend as Figure 5.3

5.2 Reactor Sizing for D-D Reactions

Using the design approach and the assumptions developed in Section 5.1, the requirements for breakeven and Q = 100 reactors were developed,
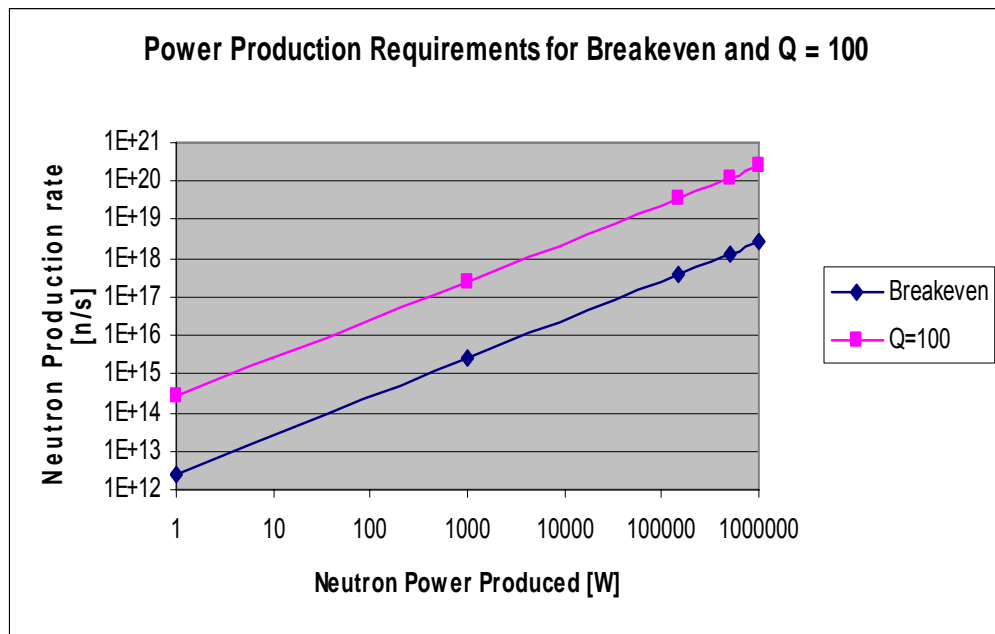
Figure 5.5: Neutron production rates necessary for breakeven and Q = 100 reactors at various power levels (for D-D reaction)

From these values a series of power density levels, based on the assumption of constant neutron producing bubble density, were generated and are listed below,

73

Table 5.3: Power Density based on Reaction Output

Reaction Output		Power Density [W/m^3]	
		Identifier	Value
Breakeven	1 W	P_{sv1}	1.94×10^4
	1 kW	P_{sv2}	1.94×10^7
	150 kW	P_{sv3}	2.87×10^9
	500 kW	P_{sv4}	9.56×10^9
	1 MW	P_{sv5}	1.94×10^{10}
Q = 100	1 W	P_{sv6}	1.94×10^6
	1 kW	P_{sv7}	1.94×10^9
	150 kW	P_{sv8}	2.87×10^{11}
	500 kW	P_{sv9}	9.56×10^{11}
	1 MW	P_{sv10}	1.94×10^{12}

As this analysis was done for a preconceptual design, it was decided that only to use the two most conservative power density values, summarized below,

Table 5.4: Conservative values of Power Density used for Design

Reaction	Power Density [W/m^3]
Breakeven – 1 W	1.94×10^4
Breakeven – 1 kW	1.94×10^7
Q =100 – 1 W	1.94×10^6
Q = 100 – 1 kW	1.94×10^9

The values in Table 5.4 were considered the most conservative of the values from Table 5.3, as they required the lowest values for maximum acoustic pressure. This approach would be useful for future conceptual reactor designs studies as the values needed for maximum acoustic pressure would be most feasible in the near term.

5.2.1 Reactor Design for a 1 W Breakeven Power Density Level

The first reactor design utilized the most conservative value for power density, P_{sv1}, that of a 1 W breakeven reaction. Since the neutron producing bubble density is based on the AICF chamber from Chapter 4, for the same sensitive volume as the Chamber2 model, the total power generated from this design would be 1 W. This is also how the power density values were generated, as detailed above (Table 5.3). Therefore for this power density level, the necessary values for the sensitive and total volumes were calculated and shown below,
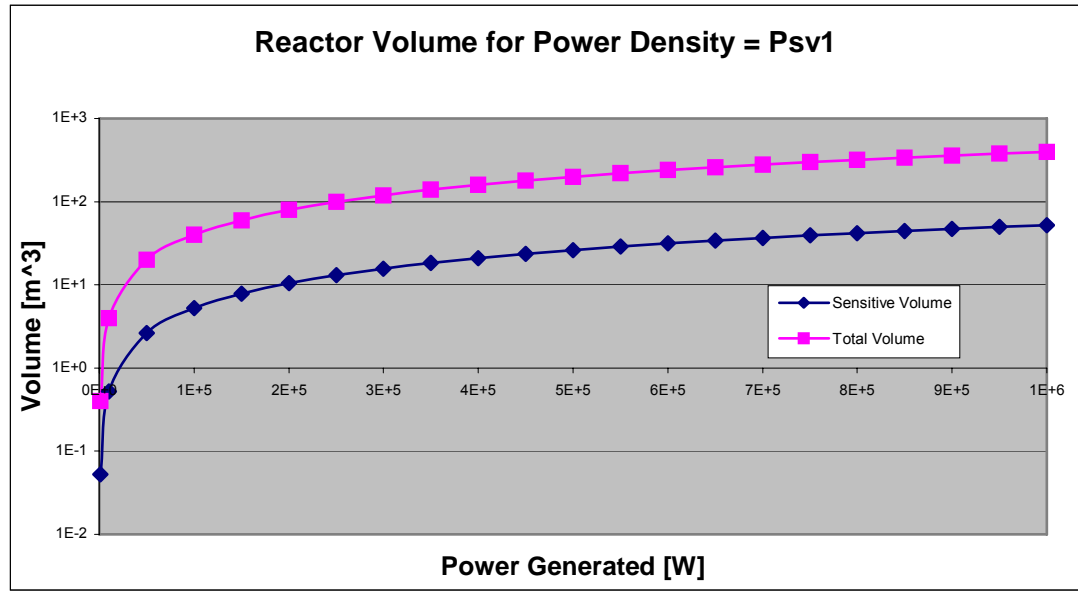
Figure 5.6: Reactor volume requirements for a 1 W breakeven power density level

The calculated parameters for this power density level are listed below in Table 5.5,

Table 5.5: Results for 1 W Breakeven Power Density Level, D-D AICF Reactor,
ChamberDesign1

Variable	Value
Maximum Acoustic Pressure needed	~ 80 bars
Weighted Cross-section	1.6×10^{-23} m^3/s
Nn, Number of neutrons produced per implosion	251 n/bubble
Nb, Number of neutron producing bubbles per second	1.0×10^{10} bubbles/s
Nf, Number of neutrons produced per second	2.55×10^{12} n/s
Power Density	1.91×10^4 W/m^3
Chamber Radius	0.295 m
Wall Thickness	2.5 cm
Chamber Height	1.46 m
Chamber Material	Glass
Maximum Wall Stress	1.7×10^6 Pa
Input Force Required	6.2×10^6 N

A 1 kW reactor was then designed following the benchmarked multiphysics approach from Chapter 4. The requirements for this power level were $V_s = 5.23 \times 10^{-2}$ m^3, and a total volume of $V = 0.398$ m^3.
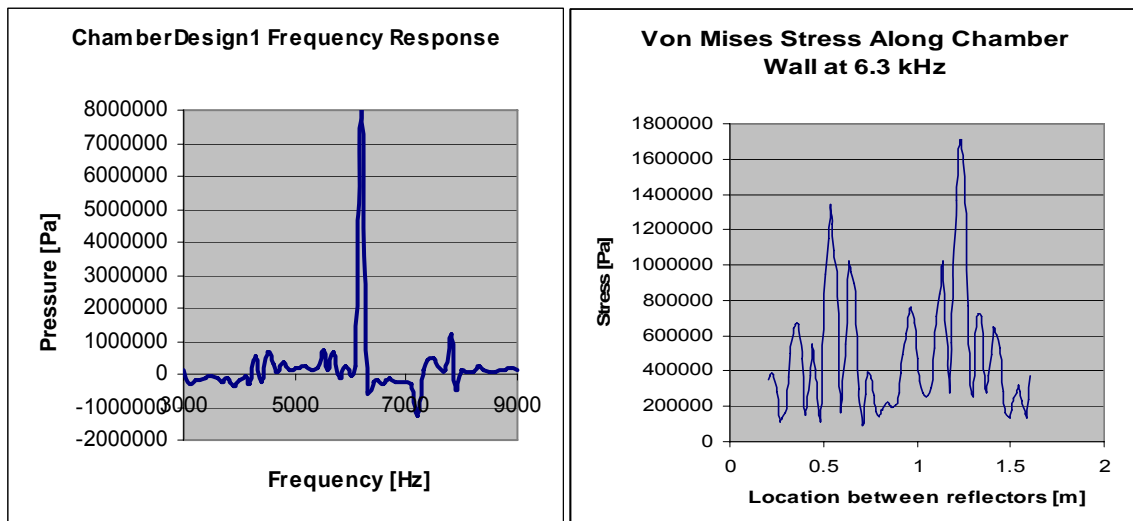
Figure 5.7: Results for frequency response and wall stress for ChamberDesign1.

Glass has a fracture stress of about 170 MPa, so for a maximum stress produced of ~1.7 x 10^6 Pa, there would be no need to change the material.

5.2.2 Reactor Design for a 1 kW Breakeven Power Density Level

The second design utilized the specific power level P_{sv2}, based on 1 kW breakeven reaction occurring in the same volume as that of the Chamber2 model. The values for sensitive and total volume necessary for various power levels are given below,
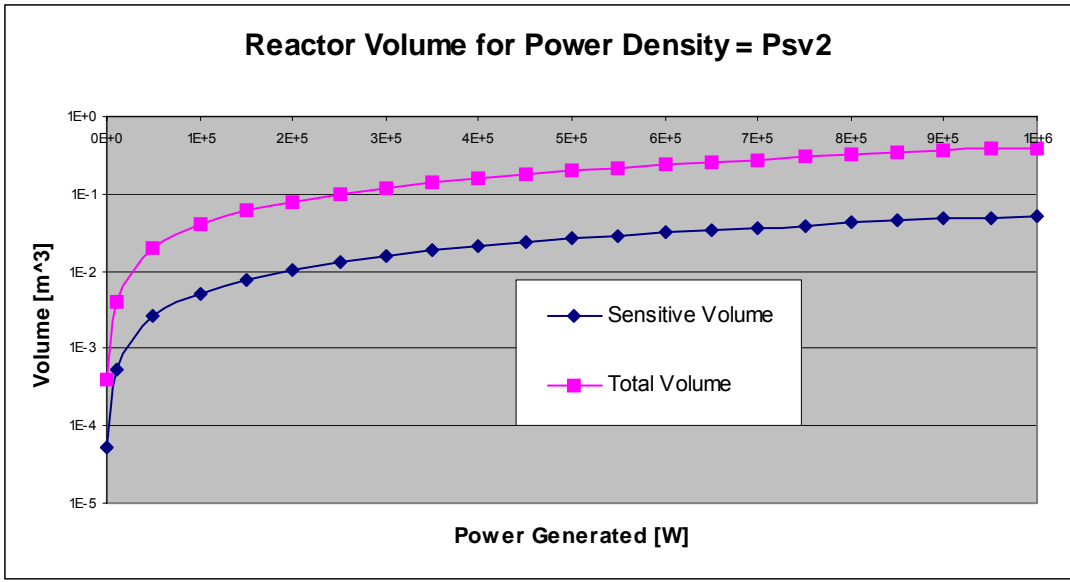
Figure 5.8: Reactor volume requirements for a 1 kW breakeven power density level

The calculated parameters for this power density level are listed below in Table 5.6,

Table 5.6: Results for 1 kW Breakeven Power Density Level, D-D AICF Reactor, ChamberDesign2

Variable	Value
Maximum Acoustic Pressure needed	~ 160 bars
Weighted Cross-section	5.7×10^{-23} m^3/s
Nn, Number of neutrons produced per implosion	884 n/bubble
Nb, Number of neutron producing bubbles per second	2.9×10^{12} bubbles/s
Nf, Number of neutrons produced per second	2.55×10^{15} n/s
Power Density	1.91×10^{7} W/m^3
Chamber Radius	0.0295 m
Wall Thickness	2.5 mm
Chamber Material	Glass
Maximum Wall Stress	2.5×10^{8} Pa
Input Force Required	2.6×10^{8} N

A 1 kW reactor was then designed following the benchmarked multiphysics approach from Chapter 4. The requirements for this power level were $V_s = 5.23 \times 10^{-5}$ m^3, and a total volume of $V = 3.94 \times 10^{-4}$ m^3.
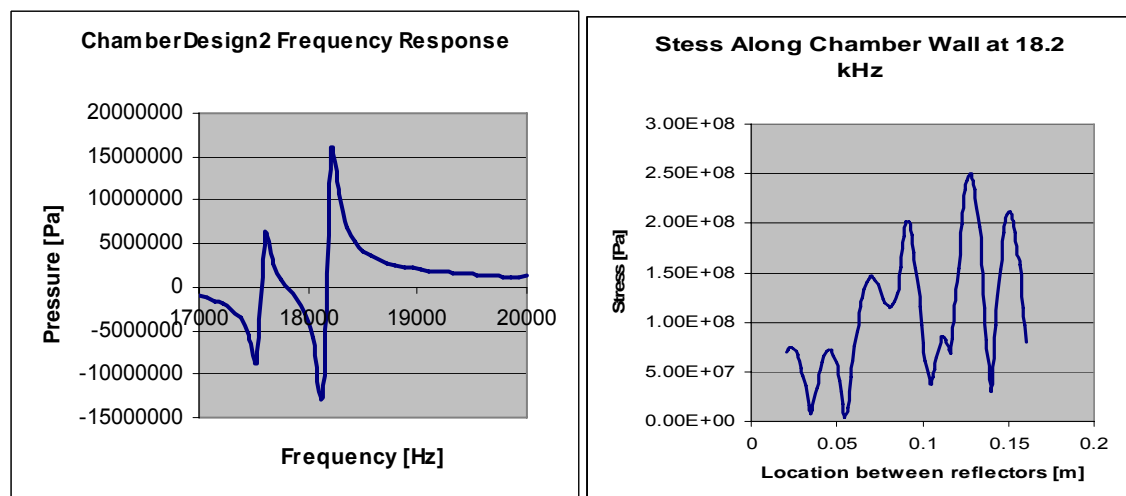
Figure 5.9: Results for frequency response and wall stress for ChamberDesign2.

5.2.3 Reactor Design for a 1 W Q =100 Power Density Level

The third design utilized the power denisty level P_{sv6}, based on 1 W Q =100 reaction occurring in the same volume as that of the Chamber2 model. The values for sensitive and total volume are given below,
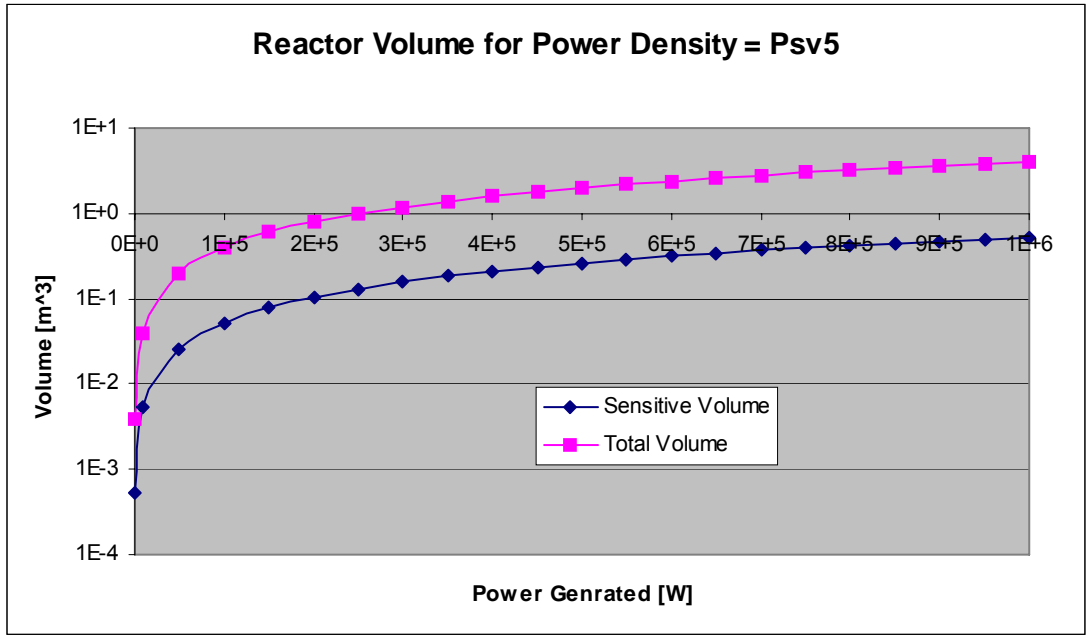
Figure 5.10: Reactor volume requirements for a 1 W Q = 100 power density level

The calculated parameters for this power density level are listed below in Table 5.7,

Table 5.7: Results for 1 W Q = 100 Power Density Level, D-D AICF Reactor, ChamberDesign3

Variable	Value
Maximum Acoustic Pressure needed	~ 120 bars
Weighted Cross-section	3.1×10^{-23} m^3/s
Nn, Number of neutrons produced per implosion	488 n/bubble
Nb, Number of neutron producing bubbles per second	5.2×10^{11} bubbles/s
Nf, Number of neutrons produced per second	2.55×10^{14} n/s
Power Density	1.91×10^6 W/m^3
Chamber Radius	0.064 m
Wall Thickness	5.25 mm
Chamber Material	Glass
Maximum Wall Stress	2×10^8 Pa
Input Force Required	4.45×10^7 N

A 1 kW reactor was then designed following the benchmarked multiphysics approach from Chapter 4. The requirements for this power level were $V_s = 5.23 \times 10^{-4}$ m^3, and a total volume of $V = 3.98 \times 10^{-3}$ m^3.
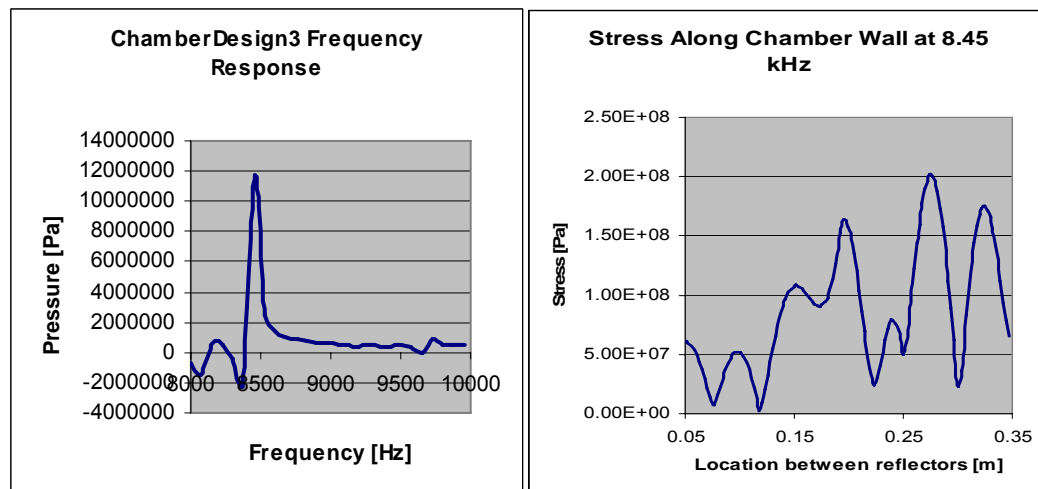
Figure 5.11: Results for frequency response and wall stress for ChamberDesign3.

5.2.4 Reactor Design for a 1 kW Q =100 Specific Power Level

The fourth and final design utilized the power density level P_{sv7}, based on 1 kW Q =100 reaction occurring in the same volume as that of the Chamber2 model. The values for sensitive and total volume are given below,
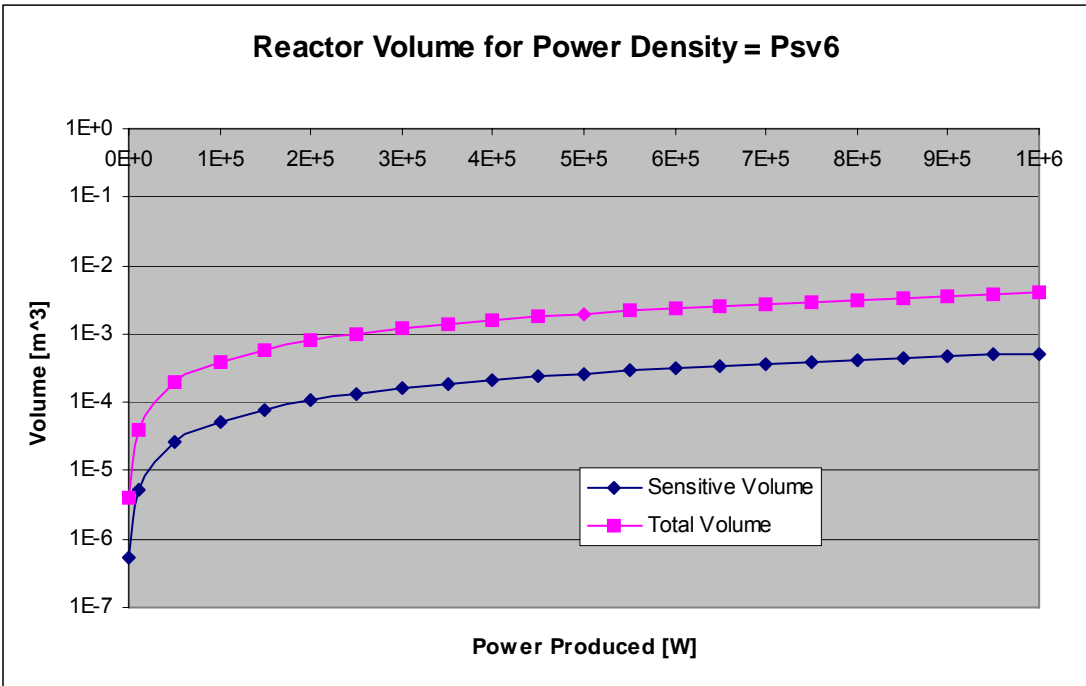
Figure 5.12: Reactor volume requirements for a 1 kW Q = 100 power density level

The calculated parameters for this specific power level are listed below in Table 5.8,

Table 5.8: Results for 1 kW Q = 100 Power Density Level, D-D AICF Reactor, ChamberDesign4

Variable	Value
Maximum Acoustic Pressure needed	~ 240 bars
Weighted Cross-section	1.1×10^{-22} m^3/s
Nn, Number of neutrons produced per implosion	1669 n/bubble
Nb, Number of neutron producing bubbles per second	1.53×10^{14} bubbles/s
Nf, Number of neutron produced per second	2.55×10^{17} n/s
Power Density	3.62×10^{10} W/m^3
Chamber Radius	0.0064 m
Wall Thickness	0.525 mm
Chamber Material	Steel
Maximum Wall Stress	4×10^8 Pa
Input Force Required	7.58×10^9 N

A 1 kW reactor was then designed following the benchmarked multiphysics approach from Chapter 4. The requirements for this power level were $V_s = 5.23 \times 10^{-7}$ m^3, and a total volume of $V = 3.98 \times 10^{-6}$ m^3.
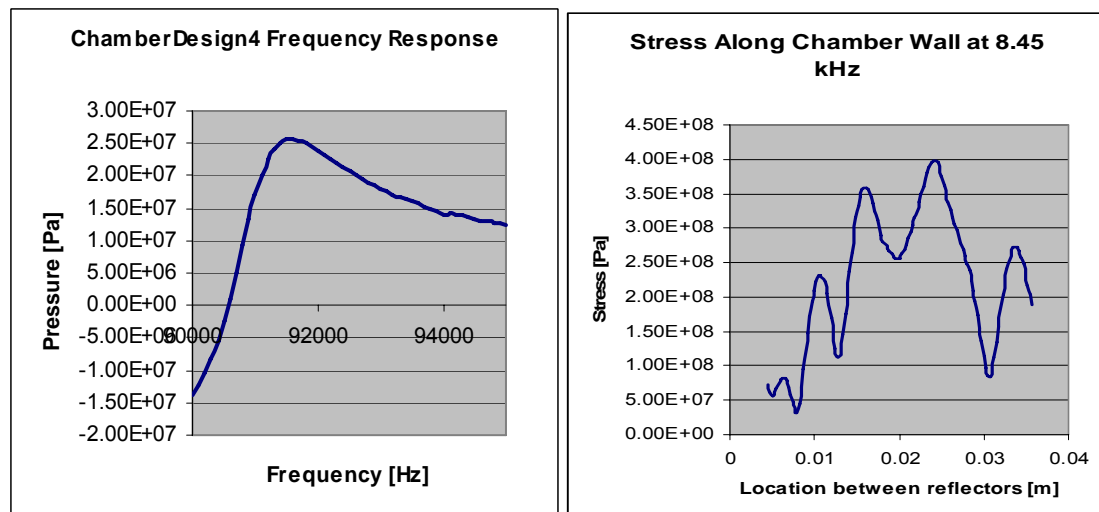
Figure 5.13: Results for frequency response and wall stress for ChamberDesign4.

It was decided that the chamber wall would be too difficult to make and be too fragile at a 0.5 mm thickness therefore, ChamberDesign4 was modeled using steel as the structural material (yield stress ~1 x 10^{11} Pa).

5.3 Reactor Sizing for D-T and D-^{3}He Reactions

There are other thermonuclear fusion reactions which are of interest for power production. Deuteron-Deuteron fusion is however most likely the best choice for the initial proof of concept-type designs. The reason is that deuterium is extremely abundant, and not radioactive, thus being just about perfect for laboratory experiments. However for commercial fusion reactors, the D-T, and D-^{3}He reactions are of great interest as they both are more energy dense reactions. The D-T reaction also benefits from a lower ignition temperature than the D-D reaction. Also, the D-^{3}He reaction benefits from nearly all of the products being charged particles. Following the same approach as detailed in Section 5.1, one reactor was designed for both the D-T and D-^{3}He. Both were designed at the 1 W breakeven power density levels so as to provide a conservative starting point for future research.

5.3.1 Reactor Sizing for a D-T Reaction

The first alternate reaction considered was the D-T reaction. This reaction produces a 3.5 MeV alpha particle (^{4}He$^+$) and a 14.1 MeV neutron. Design of the D-T reactor can be considered the same as the D-D reactor, with the difference being the energy of the neutron (14.1 MeV compared to 2.45 MeV). The production requirements for breakeven and Q = 100 reactions are summarized below,
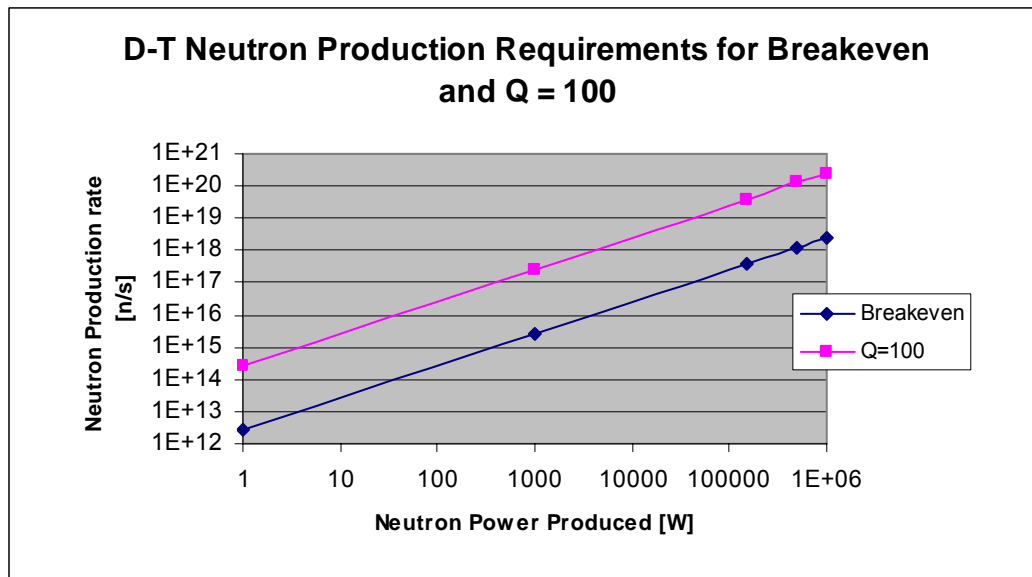
Figure 5.14: Neutron production rates necessary for breakeven and Q = 100 reactors at various power levels (for D-T reaction)

The calculated parameters for this specific power level are listed below in Table 5.9,

Table 5.9: Results for 1 W Q = 100 Power Density Level, D-T AICF Reactor, ChamberDesign5

Variable	Value
Maximum Acoustic Pressure needed	~ 100 bars
Weighted Cross-section	8.75×10^{-22} m^3/s
Nn, Number of neutrons produced per implosion	13250 n/bubble
Nb, Number of neutron producing bubbles per second	3.34×10^9 bubbles/s
Nf, Number of neutrons produced per second	4.43×10^{13} n/s
Power Density	1.89×10^6 W/m^3
Chamber Radius	0.64 m
Wall Thickness	5 cm
Chamber Material	Steel
Maximum Wall Stress	1×10^7 Pa
Input Force Required	3.83×10^7 N

A 1 MW reactor was then designed following the benchmarked multiphysics approach from Chapter 4. The requirements for this power level were $V_s = 5.28 \times 10^{-1}$ m^3, and a total volume of V = 3.94 m^3.
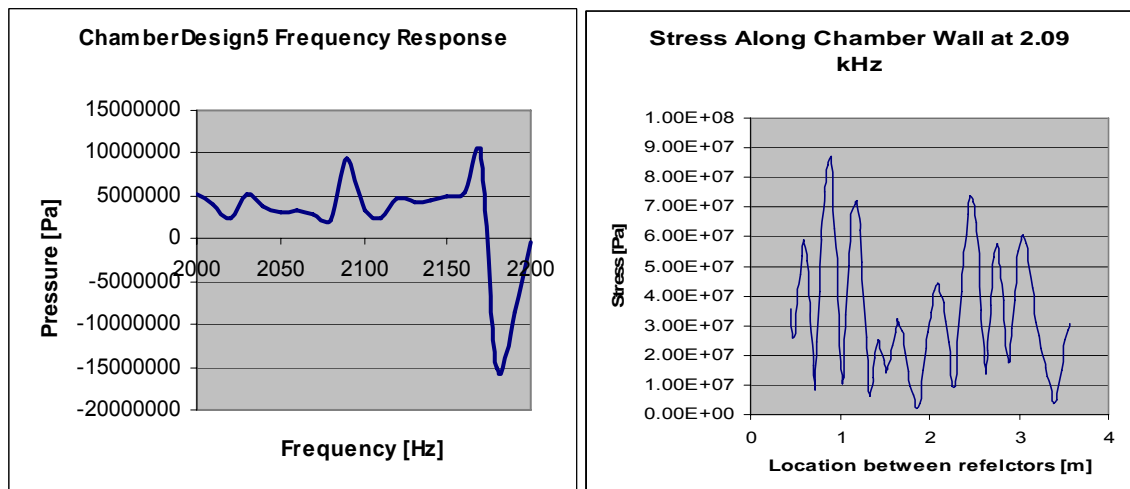
Figure 5.15: Results for frequency response and wall stress for ChamberDesign5.

5.3.2 Reactor Sizing for a D-^{3}He Reaction

The final reaction considered was the D-^{3}He reaction. The reaction produces a 3.6 MeV alpha particle (^{4}He$^+$) and a 14.7 MeV proton. As the alpha particle is very massive and positively charged, it would not travel very far in the fluid before losing its energy. However at the energy levels of the proton, it is assumed to act like a neutron, and escapes the fluid. There will be charged particle interactions with the rest of the fluid, but they were assumed to be negligible for this analysis. The production requirements for breakeven and Q = 100 reactions are summarized below,
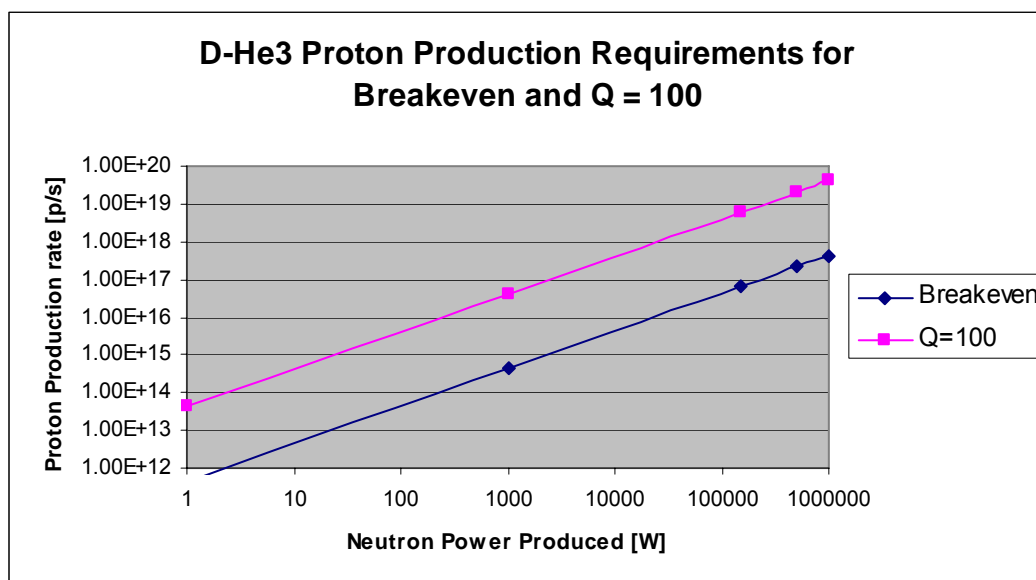
Figure 5.16: Proton production rates necessary for breakeven and Q = 100
reactors at various power levels (for D-^{3}He reaction)

The same assumptions and trends were used for this analysis as those used for the D-D reaction. The power densities will remain the same between all reactions as they are simply and energy balance (i.e. 1 kW of breakeven energy via a D-D reaction is the same as 1 kW of breakeven energy from a D-^{3}He). The difference is that the different reactions produce particles at different levels, thus

each reaction requires a different numbers of particles to produce that energy. With respect to AICF this translates to higher or lower values for acoustic pressure, as per Figure 5.3 (i.e. more particles means a higher maximum acoustic pressure). A comparison of D-D and D-^{3}He particle production needed for breakeven power production is shown below,
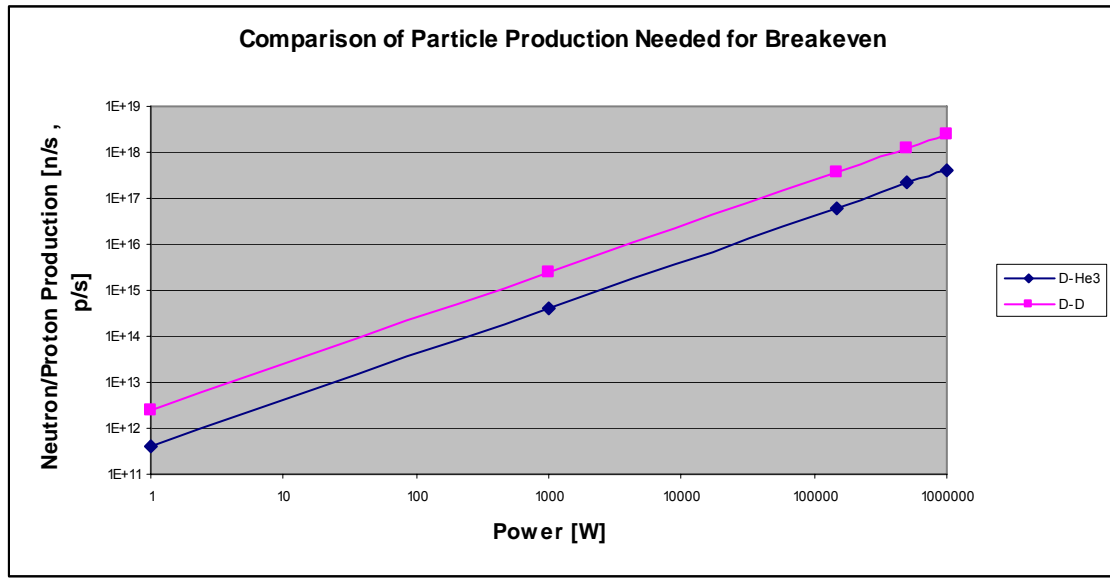
Figure 5.17: Comparison of particle production needed

The calculated parameters for this specific power level are listed below in Table 5.10,

Table 5.10: Results for 1 W Q = 100 Power Density Level, D-^{3}He AICF Reactor, ChamberDesign6

Variable	Value
Maximum Acoustic Pressure needed	~ 100 bars
Weighted Cross-section	4.3×10^{-23} m^3/s
Nn, Number of neutrons produced per implosion	281 n/bubble
Nb, Number of neutron producing bubbles per second	1.5×10^{11} bubbles/s
Nf, Number of neutrons produced per second	4.25×10^{13} n/s
Power Density	3.62×10^7 W/m^3
Chamber Radius	0.64 m
Wall Thickness	5 cm
Chamber Material	Steel
Maximum Wall Stress	1×10^7 Pa
Input Force Required	3.83×10^7 N

A 1 MW reactor was then designed following the benchmarked multiphysics approach from Chapter 4. The requirements for this power level were $V_s = 2.76 \times 10^{-2}$ m^3, and a total volume of V = 3.94 m^3. As the power density was the same as that of ChamberDesign5, the results for frequency response and stress levels would also be the same as those in Figure 5.14. The difference between these two results was the number of particles required to produce this energy, analogous to Figure 5.16 (slightly less for D-^{3}He).

5.3 AICF Reactor Shielding Analysis

A shielding analysis was performed for a 1 kW Q = 100 D-T reaction. The neutrons that are generated from the reaction are emitted from the center of the reactor out, in all directions. Just outside of the chamber wall is what is called the heat exchange or thermal conversion system, whose purpose is to capture the energy of the fusion neutrons and transfer that energy to a coolant. Following the concept outline by Miley *(10)* the basic steps for thermal conversion are; for the neutrons and radiation to be absorbed in a blanket or shield, for the heat in the blanket to be extracted, the heat is used to generate electricity in a conversion system, and finally the waste heat must be rejected. As well as absorbing a large fraction of the neutron and radiation energy, the blanket can also serve as a breeding medium from tritium. Because tritium is so rare in nature, in must be manufactured in-situ to assure a constant fuel supply. The typical reaction considered for tritium breeding is the two neutron reactions with lithium *(10)*,

$$^{1}n + {}^{6}Li \rightarrow {}^{4}He + {}^{3}T + (4.785)MeV$$
$$^{1}n + {}^{7}Li \rightarrow {}^{4}He + {}^{3}T + {}^{1}n' + (-2.5)MeV$$

(44)
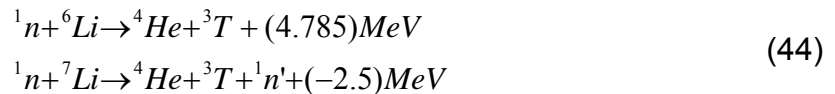
The heat is then extracted from the blanket via a circulating coolant (water). The coolant then passes through a steam generation system to produce electricity. In order to determine the basic parameters for AICF reactor design above, a basic sizing analysis was performed.

The first-wall power loading is defined as,

$$\Lambda \equiv \frac{P_f}{A_w}$$

(45)

Where P_f is the fusion power produced, and A_w is the area of the chamber. Power loading as a function of power produced is shown in Figure 5.9.
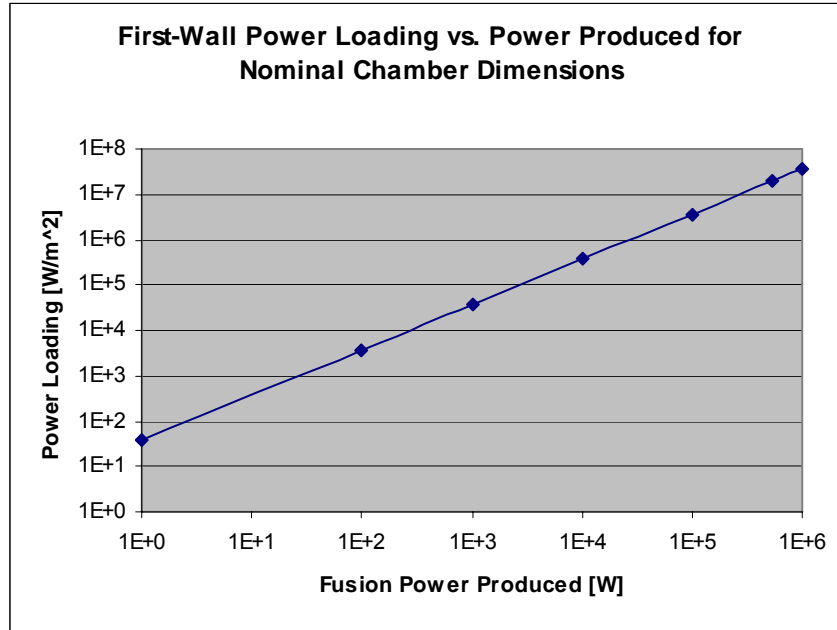
Figure 5.18: Chamber wall power loading as a function of fusion power produced

For a single phase coolant the total volumetric flow rate is related to the wall power loading by an overall energy balance *(10)*,

$$Q = \frac{\Lambda \cdot A_w \cdot f_b}{\rho \cdot C_p \cdot \langle \Delta T \rangle} \tag{46}$$

Where ρ is the coolant density, C_p is the specific heat of the coolant, $\langle \Delta T \rangle$ is the average coolant temperature rise, and f_b is a correction factor for additional energy generated in the blanket. The $\langle \Delta T \rangle$ value is limited by thermal-stress considerations, and a value of $100^{\circ}C$ is considered to be typical. The f_b factor accounts for the exothermic reactions in the blanket, and if no fissionable materials are used within the blanket, is typically on the order of 1.3.
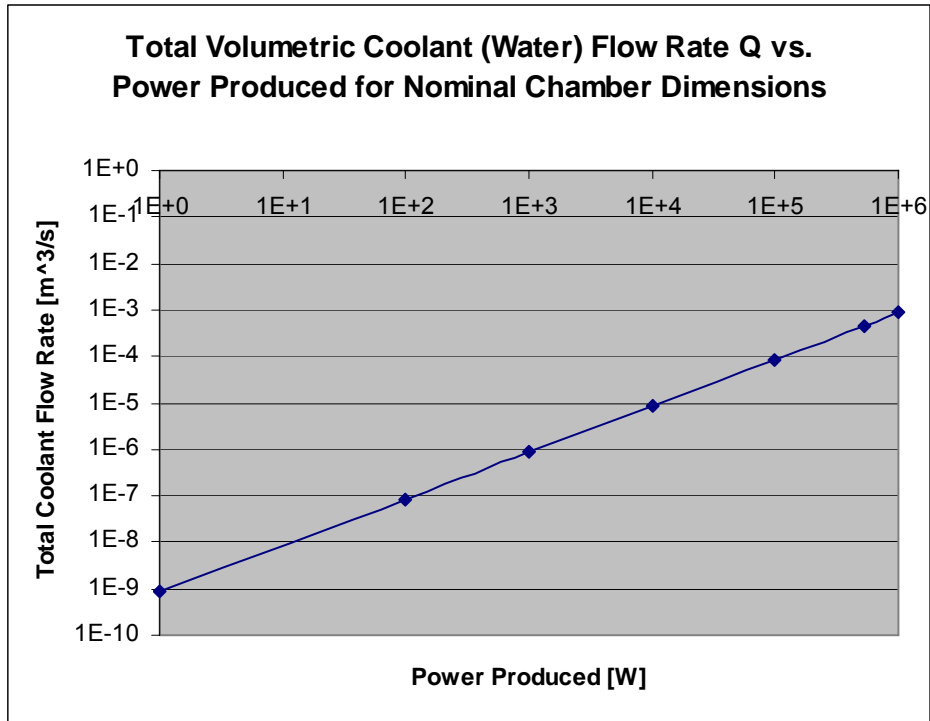
Figure 5.19: Volumetric coolant flow rate as a function of power produced

The average coolant velocity, u_c, can be determined by the following,

$$u_c = \frac{Q}{A_c} = \frac{\Lambda}{\rho \cdot C_p \cdot \langle \Delta T \rangle} \left(\frac{A_w}{A_c} \right) \tag{47}$$

Where A_c is the coolant flow area necessary for the given volumetric flow rate.
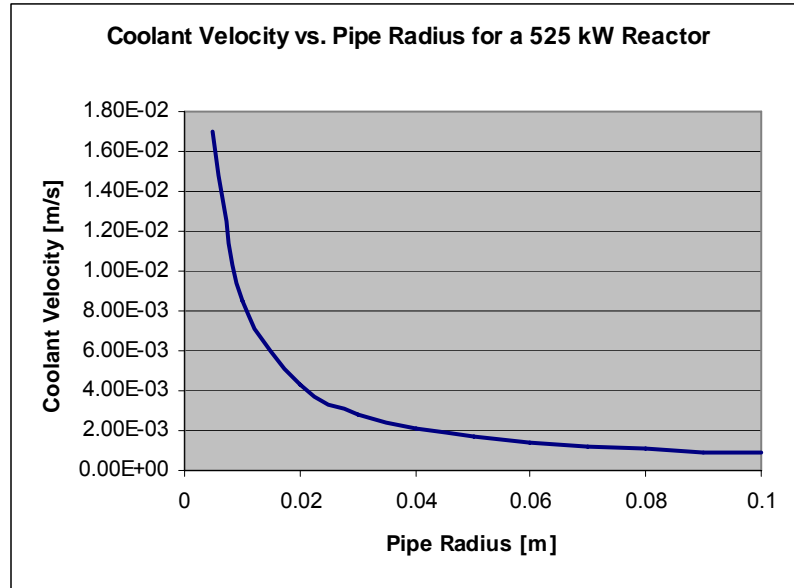
Figure 5.20: Coolant velocity necessary for an average coolant temperature rise of 100 $^{\circ}$C as a function of pipe radius

The pumping power, P_L, necessary for the desired coolant and flow rate is,

$$P_L = Q \cdot \Delta p \tag{48}$$

where Δp is the coolant pressure drop through the coolant lines. The pressure drop over a pipe section of length, L, can be calculated from the conventional relation,

$$\Delta p = \frac{\rho \cdot L \cdot u_c^2}{2d_c} C_f \tag{49}$$

Where d_c is the inner diameter of the coolant pipe, and C_f is the friction factor of the pipe. Finally the heat flux, q_w, can be through the blanket can be calculated by,

$$q_w = h \cdot (T_i - T_o) \tag{50}$$

Where h is the heat-transfer coefficient, T_i is the inner wall temperature, and T_0 is the outer wall temperature.

A basic schematic of a reactor vessel for an AICF D-T system is shown below in Figure 4.9,
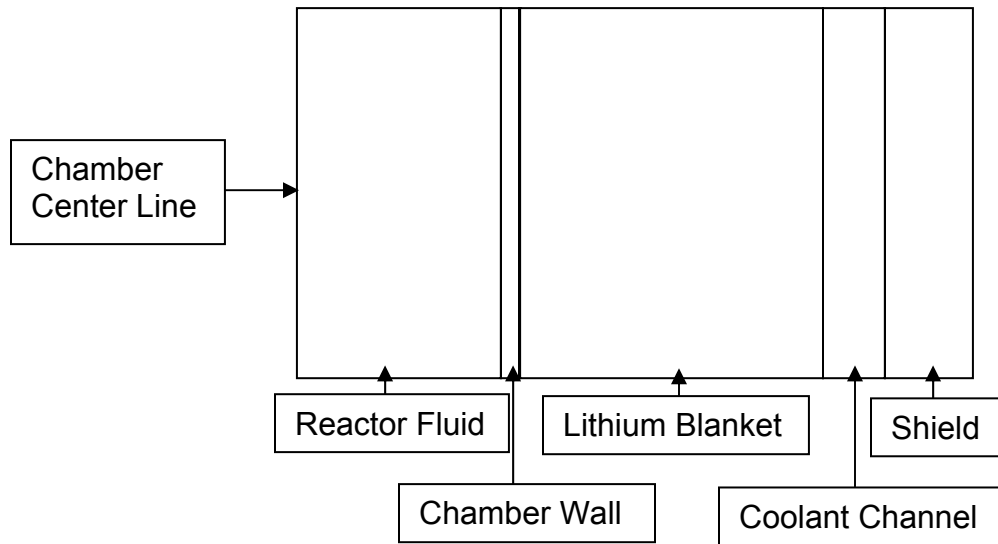
Figure 5.21: Basic schematic of reactor vessel wall cross section

In order to determine the thickness of the blanket, coolant channel, and shield the mean free path, λ, of the neutrons must be determined, which is a measure of the average distance a particle travels through a specific medium before a collision.

$$\lambda = \frac{1}{\Sigma_t} = \frac{1}{N \cdot \sigma_t} \tag{51}$$

Where Σ_t is the total macroscopic cross-section, N is the atom or molecular density, and σ_t is the total microscopic cross-section. A range of values for the materials of interest are listed below in Table 4.5 (for neutron interactions).

Table 5.11: Energy Conversion Material Properties *(18)*

Material	σ_t [barns]		N [atoms/cm^2] x 10^{24}	Lambda [cm]	
	@ 2.45 MeV	@ 14.1 MeV		@ 2.45 MeV	@ 14.1 MeV
H	2.57	0.66	0.0418	9.3	36.2
C	1.585	1.379	0.0802	7.9	9.0
O	0.896	1.7	0.043	26.0	13.7
Li-6	1.6	1.4	0.046	13.6	15.5
Si	2.479	1.8	0.0499	8.1	11.1
Na	3.235	1.735	0.0254	12.2	22.7
Al	2.086	1.748	0.0602	8.0	9.5
Pb	4.929	5.578	0.0330	6.2	5.4
B	2.174	1.455	0.1281	3.6	5.4
Acetone	21.071	9.797	0.0622	0.8	1.6
Glass	25.533	26.975	0.0593	0.7	0.1
Water	1.082	1.585	0.0334	27.7	18.9

The average fractional energy loss per collision is given by *(6)*,

$$\frac{\overline{\Delta E}}{E} = \frac{1}{2}(1-\alpha) \tag{52}$$

Where $\overline{\Delta E}$ is the average energy loss per collision, E is is starting energy, and α is the collision parameter given by,

$$\alpha = \left(\frac{A-1}{A+1}\right)^2 \tag{53}$$

Where A is the atomic number of the material the particle is colliding into.

For the given chamber dimensions and material properties, a 14.1 MeV neutron created at the center of the AICF chamber will undergo three collisions within the reactor fluid resulting in a exit energy of 6.1 MeV (for a fractional energy loss of 24.3% per collision). Assuming that 2 mean free paths are necessary to insure that a sufficient number of the desired tritium-breeding lithium reactions takes place (Eq.(44)), the blanket thickness is determined to be 30 cm and the exit energy is 2.4 MeV.

In order to determine the thickness of the shield, a satisfactory dose rate level must be determined. An accepted value for yearly biological dose is 5 Rem/yr. The lower the neutron energy, the less energy each particle will deposit into whatever it comes into contact with. Therefore, it is beneficial for the shielding to reduce the neutron energy to sufficiently low levels (~0.1 eV). Therefore for this design the shield must reduce the incoming neutron energy from 2.4 MeV to 0.1 eV. A good material for thermalizing neutrons is paraffin, $C_{22}H_{46}$. The reason paraffin is a good shield is because of the high concentration of hydrogen atoms. Hydrogen, with an atomic number of 1, provides the highest values for the collision parameter, α. A high collision parameter value means that the subsequent fractional energy loss per collision is very high, thus rapidly reducing the energy of the neutrons. Additionally for space purposes, paraffin has a low density ($\rho = 930$ kg/m^3), which results in increased specific power for the propulsion system. The thickness of the shield can then be determined by multiplying the number of collisions necessary to adequately reduce the neutron energy by the mean free path length. This can be determined by multiplying the collision parameter by the initial energy,

$$\alpha \cdot E = \left(\frac{A-1}{A+1}\right)^2 \cdot E \tag{54}$$

To determine the number of collisions, x, necessary to reduce the energy from E to E', the following relationship can be solved for x,

$$E' = \alpha^x E \tag{55}$$

For E = 2.4 MeV and E' = 0.1 eV, the number of collisions necessary is calculated to be ~10.5 and for a mean free path of 2.7 cm, the shield thickness is calculated to be ~28.5 cm.

In order to determine any additional shielding necessary to reduce the neutron flux such that the yearly dose rate is less than or equal to 5 Rem/yr, the neutron flux, Φ_n, at each stage must be determined.

Table 5.12: Neutron Flux at Various Positions

Position	Φ_n [n/s*cm^2]
Center of AICF Reaction Chamber	2.55×10^{17}
Chamber Wall	9.46×10^{14}
Outer Blanket Wall	1.05×10^{14}
Outer Coolant Wall	5.10×10^{12}
Outer Wall of Thermalization Shield	1.49×10^{8}

From Lamarsh and Baratta *(8)*, for thermal neutron energies, Φ_n = 260 n/s*cm^2 gives 1 mrem/hour. Therefore the yearly dose rate from the biological shield can be determined by dividing an exit flux by the 260 n/s*cm^2 value above.

Radiation Dose Rate as a Function of Shield Thicknes for a 1kW Q=100 D-D Reaction
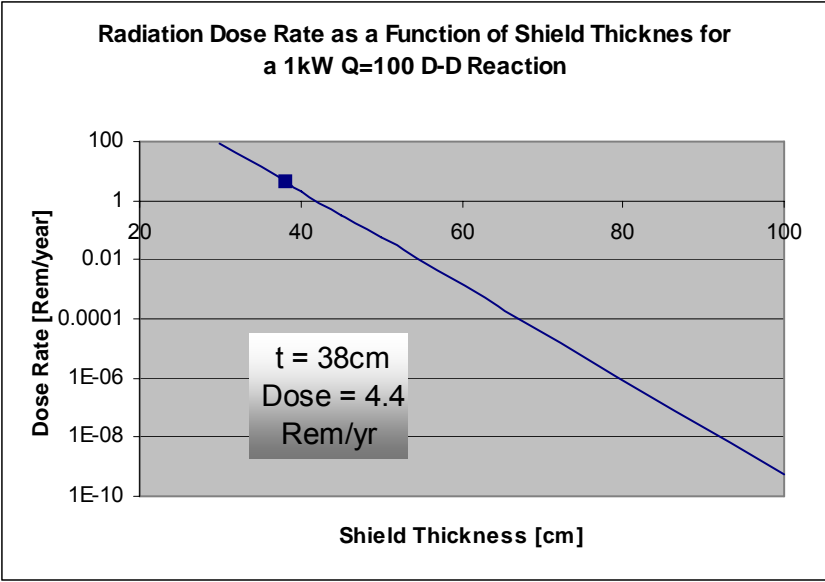
Figure 5.22: Radiation dose as a function of shield thickness

It can be seen from Figure 4.10 that for a biological shield thickness of 38 cm, the year dose rate can be controlled to an acceptable value of 4.4 Rem/year. The total shield thickness is then the combination of the thermalization and biological shields, ~66 cm of paraffin.

CHAPTER 6: CONCLUSION

An analysis was completed to characterize the experimental AICF reaction chamber and provide the basis for basic preconceptual reactor design. The chamber characterization was accomplished by experimentally benchmarking a multiphysics finite element method model created with the program FEMLAB™ (recently changed to Comsol Multiphysics™). Pressure mapping tests produced benchmarked results against the multiphysics model which resulted in an accurate representation of the important acoustic modes. The magnitude of the pressure oscillations was found to agree well with the introduction of an experimentally determined coupling factor, k. Finally, the frequencies of the important acoustic modes produced in the multiphysics analysis were found to lag the experimental results by close to 1 kHz. It was hypothesized that the lack of electrical resonance modeling (piezoelectric physics), and the lack of multidimensional coupling of the acoustic wave reflectors accounted for this frequency lag.

Confirmatory AICF experiments were conducted with neutron-seeded deuterated acetone, where data indicated that statistically significant 2.45 MeV neutrons and tritium were produced. Control experiments did not result in such emissions. From these experiments insights were derived on scalability and the importance of maintaining spherical implosions.

Additional benchmarking of the multiphysics modeling approach was done against a similar design study conducted at the Rensselaer Polytechnic Institute. Comparison results for this analysis produced even more accurate resonant mode predictions than that of the AICF chamber. The proposed reason for better coupling to this model was that the overall geometry was much simpler. For

instance there was no liquid/gas interface, the pistons were fixed, there was no multidimensional reflector coupling, etc. This reduction of complexities was most like the reason for the more accurate results.

Using the benchmarked multiphysics modeling approach and a couple of experimentally determined trends, a series of preconceptual AICF reactor designs were created for three different fusion reactions. These designs were created with the intention of providing a roadmap to future scaling work. Although current AICF energy production is at least six orders of magnitude below that of breakeven, it was found that with as little as approximately a five times increase in maximum acoustic pressure, D-D breakeven may be possible. Other preconceptual designs provide a starting point for building and analyzing scaled up AICF reactors.

6.1 Recommendations for Future Work

There is a large amount of progress to be made in the relatively new field of acoustic inertial confinement fusion. Specifically, there is much potential for increasing fusion rates, via the use of a benchmarked multiphysics modeling approach. There remains however many improvements that can be made to the multiphysics model. The main omissions from this research to that of the experimental systems are: characterization and modeling of the piezoelectric electrical resonances, and multidimensional coupling of the acoustic reflectors. Additional refinements should be made to the structural and fluid damping. Future work in multiphysics modeling should also include: 3-dimensional effects on the acoustic pressure field caused by voids (bubbles), and modeling of 'streamers', which are type of bubble source found to adversely affect the production of fusion energy.

Additional work needs to be conducted in the area of shock implosion-dynamics. A better understanding of this area should lead to improved

predictions of bubble core temperatures, and thus fusion reaction rates, to more accurately predict the acoustic pressure fluctuations needed to create these conditions.

Finally there is a great deal of work to be done in the scaling of AICF experiments to ascertain the realistic possibility of using this approach to someday create breakeven and beyond fusion reactors.

LIST OF REFERENCES

LIST OF REFERENCES

1. Taleyarkhan, R.P., West, C.D, Cho, J.S., Lahey, R.T. Jr., Nigmatulin, R.I., and Block, R.C., "Evidence of Nuclear Emissions During Acoustic Cavitation," *Science*, Vol.295, 1868-1873, 8 March, 2002.

2. Taleyarkhan, R.P., West, C.D, Cho, J.S., Lahey, R.T. Jr., Nigmatulin, R.I., and Block, R.C., "Additional Evidence of Nuclear Emissions During Acoustic Cavitation," *Phys.Rev.E*, Vol.69, 036109, March, 2004.

3. Gross, R.A., Fusion Energy, John Wiley and Sons, New York, 1984.

4. Kammash, T., "Principles of Fusion Energy Utilization in Space Propulsion", *Fusion Energy in Space Propulsion (Progress in Astronautics and Aeronautics)*, Vol.167, 1-46, 1995.

5. Watanabe, Y., Carrera, R., "Fusion-Fission Hybrid Nuclear Rocket Engine", *Fusion Energy in Space Propulsion (Progress in Astronautics and Aeronautics)*, Vol.167, 1-46, 1995.

6. Lamarsh, J. R., Baratta, J., Introduction to Nuclear Engineering, Prentice Hall, New Jersey, 2001.

7. AIAA SP-108-2004, "Recommended Design Practices for Conceptual Nuclear Fusion Space Propulsion Systems", American Institute of Aeronautics and Astronautics, 2004.

8. Cancelos, S., Moraga, F. J., Lahey Jr., R. T., Bouchilloux, P, "The Design of Acoustic Chambers for Bubble Dynamics Research", *Japan-US Seminar on Two-Phase Flow Dynamics*, Vol.2, December, 2004.

9. Taleyarkhan, R. P., Lahey Jr., R. T., Nigmatulin, R. I. "Bubble Nuclear Fusion Technology - Status and Challenges", *Japan-US Seminar on Two-Phase Flow Dynamics*, Vol.2, December, 2004.

10. Miley, G. H., Fusion Energy Conversion, American Nuclear Society, 1976.

11. Cox, L.T., "Thermonuclear cross section and reaction-rate-parameter data compilation", Report No. AL-TR-90-053, Air Force Astronautics Lab (Edwards AFB), July, 1991.

12. FEMLab Version 3.1, COMSOL Inc., Burlington, Massachusetts, 2005.

13. Uranium Information Centre, "Nuclear Reactors for Space", Briefing Paper #82, January 2004. http://www.uic.com.au/nip82.htm

14. Xu, Y., Butt, A., "Confirmatory Experiments for Nuclear Emissions During Acoustic Cavitation", Nuclear Engineering and Design 235 (2005), 1317-1324.

15. Channel Industries Inc. http://www.channelindustries.com/

16. Wilmad Labglass Inc., Borosilicate Glass Properties, www.wilmad-labglass.com/pdf/ Borosilicate%20Glass%20Properties.pdf

17. CRC Handbook of Heat Transfer, 79th Edition, CRC Press, 1998-1999.

18. Table of Nuclides. Korea Atomic Energy Research Institute, Nuclear Data Evaluation Lab. http://atom.kaeri.re.kr/

19. Xu, Y., Butt, A., "Bubble Dynamics and Tritium Emission During Bubble Fusion Experiments", The 11th International Topical Meeting on Nuclear Reactor Thermal-Hydraulics (NURETH-11), Popes' Palace Conference Center, Avignon, France, October 2-6, 2005.

APPENDICES

Appendix A

Additional Benchmark Comparison

The experimental pressure map of a 125 mL conical flask was recorded and the results were compared to a FEMLAB™ modeling results using the developed modeling approach.
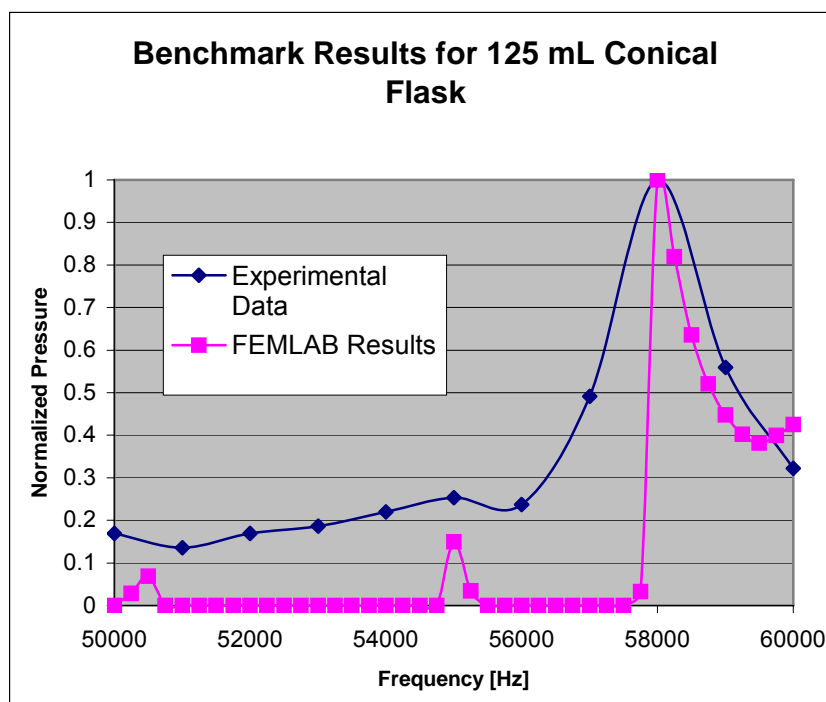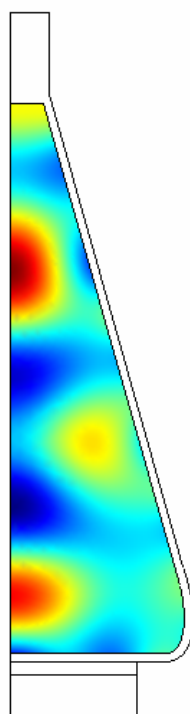
Appendix B

Determination of Scaling Parameters used for Reactor Design

A series of spreadsheets were created to calculate all the necessary parameters for reactor design.

D-D AICF Reactor Sizing

Assumptions and Constants (for D-D Fusion):

rho =	1.00E+04 [kg/m^3]	% Compressed fluid density
Ni =	5E+29 [Ions/m^3]	% Ion Concentration
<SigmaV>d =	4.50E-25 [m^3/s]	% Weighted Cross-Section for D-D at T
T =	1.00E+08 [K]	% Compressed Temperature
deltaT =	5.00E-13 [s]	% Reaction Time
R =	5.00E-08 [m]	% Compressed Bubble Radius
En =	2.45 [MeV]	% D-D neutron energy
Nbc =	1000.00 [bubbles/cluster]	% Number of bubbles in each cluster
Nbi =	20.00 [bubbles/cluster]	% # of bubbles per cluster that implode violently
Ncycles =	60.00 [cycles]	% Ave. # of cycles bubbles expand and collapse
Ncn =	50.00 [clusters/s]	% Number of clusters nucleated per second
Vs =	2.76E-06 [m^3]	% Sensitive volume for nominal setup
Vt =	3.98E-04 [m^3]	% Total volume for nominal setup
Vs/V =	0.007	% Ratio of Sensitive to Total fluid volume
Rc/h =	0.2027	% Ratio of chamber radius to chamber height
1 W =	6.24E+12 [MeV/s]	% Conversion

Calculations for current AICF design (D-D Fusion):

Nn =	7.03 [n/bubble]	% # of neutrons produced per bubble implosion
Ei =	1.72E+01 [MeV/bubble]	% Neutron Energy Released per Implosion
Nb =	60000 [bubbles/s]	% Number of neutron producing bubbles per second
Vb =	1.66E-01 [m^3*bubbles/s]	% # of n producing bubbles within the Vs produced /s
Rho_b =	2.17E+10 [bubbles/m^3*s]	% Neutron producing bubble density per second
Nf =	421875 [n/s]	% Number of D-D neutrons produced per second
Efn =	1033593.8 [Mev/s]	% Amount of D-D neutron energy produced per second
Esv =	3.74E+11 [MeV/s*m^3]	% Specific Energy produced from sensitive volume
Psv =	6.00E-02 [W/m^3]	% Specific Power for sensitive volume

Calculations for Breakeven (for D-D Fusion):

Neutron production necessary for breakeven at various power levels,

Power Level [W]	1	1.00E+03	1.50E+05	5.00E+05	1.00E+06
Nf [n/s]	2.55E+12	2.55E+15	3.82E+17	1.27E+18	2.55E+18
		1	2	3	4

Assume the following relationship between Nf and the Acoustic Pressure:

Nf [n/s]	1.00E+05	1.00E+08	1.00E+11	1.00E+12	1.00E+14
P [atm]	15	30	60	80	120
T [keV]	8.6	17.2	34.4	68.8	137.6
<sigma*v> [m^3/s]	4.50E-25	2.18E-24	6.86E-24	1.604E-23	3.12E-23

Continued... Nf [n/s]	1.00E+15	1.00E+17	1.00E+18	1.00E+19	1.00E+20
P [atm]	160	240	320	400	480
T [keV]	275.2	550.4	1100.8	2201.6	4403.2
<sigma*v> [m^3/s]	5.658E-23	1.07E-22	2.353E-22	6.765E-22	2.84E-21

Efn1 =	6.24E+12 [Mev/s]	% D-D neutron energy produced per second for 1 kW
Efn2 =	6.24E+15 [Mev/s]	% D-D neutron energy produced per second for 1 kW
Efn3 =	9.36E+17 [Mev/s]	% D-D neutron energy produced per second for 150 kW
Efn4 =	3.12E+18 [Mev/s]	% D-D neutron energy produced per second for 500 kW
Efn5 =	6.24E+18 [Mev/s]	% D-D neutron energy produced per second for 1 MW
Esv1 =	2.26E+18 [MeV/s*m^3]	% Energy density produced from sensitive volume for 1W
Esv2 =	2.26E+21 [MeV/s*m^3]	% Energy rho produced from sensitive volume for 1kW
Esv3 =	3.39E+23 [MeV/s*m^3]	% Energy density produced from Vs for 150 kW
Esv4 =	1.13E+24 [MeV/s*m^3]	% Energy density produced from Vs for 500 kW
Esv5 =	2.26E+24 [MeV/s*m^3]	% Energy rho produced from sensitive volume for 1MW
Psv1 =	3.62E+05 [W/m^3]	% Power density for sensitive volume for 1 W
Psv2 =	3.62E+08 [W/m^3]	% Power density for sensitive volume for 1 kW
Psv3 =	5.43E+10 [W/m^3]	% Power density for sensitive volume for 150 kW
Psv4 =	1.81E+11 [W/m^3]	% Power density for sensitive volume for 500 kW
Psv5 =	3.62E+11 [W/m^3]	% Power density for sensitive volume for 1 MW

1 kW		1 W	
Nf =	2.55E+15	Nf =	2.55E+12
Nn =	884.13	Nn =	250.59
Nb =	2.88E+12	Nb =	1.02E+10
Rho_b =	2.17E+10		

Calculations for Q=100 (for D-D Fusion):

Neutron production necessary for Q = 100 at various power levels,

Power Level [W]	1	1.00E+03	1.50E+05	5.00E+05	1.00E+06
Nf [n/s]	2.55E+14	2.55E+17	3.82E+19	1.27E+20	2.55E+20
		1	2	3	4

Efn6 =	6.24E+14 [Mev/s]	% D-D neutron energy produced per second for 1 kW
Efn7 =	6.24E+17 [Mev/s]	% D-D neutron energy produced per second for 1 kW
Efn8 =	9.36E+19 [Mev/s]	% D-D neutron energy produced per second for 150 kW
Efn9 =	3.12E+20 [Mev/s]	% D-D neutron energy produced per second for 500 kW
Efn10 =	6.24E+20 [Mev/s]	% D-D neutron energy produced per second for 1 MW
Esv6 =	2.26E+20 [MeV/s*m^3]	% Energy density produced from sensitive volume for 1W

Esv7 =	2.26E+23 [MeV/s*m^3]	% Energy rho produced from sensitive volume for 1kW
Esv8 =	3.39E+25 [MeV/s*m^3]	% Energy density produced from Vs for 150 kW
Esv9 =	1.13E+26 [MeV/s*m^3]	% Energy density produced from Vs for 500 kW
Esv10 =	2.26E+26 [MeV/s*m^3]	% Energy rho produced from sensitive volume for 1MW

Psv6 =	3.62E+07 [W/m^3]	% Power density for sensitive volume for 1 W
Psv7 =	3.62E+10 [W/m^3]	% Power density for sensitive volume for 1 kW
Psv8 =	5.43E+12 [W/m^3]	% Power density for sensitive volume for 150 kW
Psv9 =	1.81E+13 [W/m^3]	% Power density for sensitive volume for 500 kW
Psv10 =	3.62E+13 [W/m^3]	% Power density for sensitive volume for 1 MW

1 kW		1 W	
Nf =	2.55E+17	Nf =	2.55E+14
Nn =	1669.06	Nn =	487.72
Nb =	1.53E+14	Nb =	5.22E+11

Reactor Sizing

	Reactor P [W]	Nf [n/s]	Vs [m^3]	Vtotal [m^3]
Currently	1000	1.70E+05	1.67E+04	2.40E+06
	150000	1.70E+05	2.50E+06	3.61E+08
	500000	1.70E+05	8.33E+06	1.20E+09
	1000000	1.70E+05	1.67E+07	2.40E+09
Breakeven	1000	2.55E+15	2.76E-06	3.98E-04
	150000	3.82E+17	2.76E-06	3.98E-04
	500000	1.27E+18	2.76E-06	3.98E-04
	1000000	2.55E+18	2.76E-06	3.98E-04
Q = 100	1000	2.55E+17	2.76E-08	3.98E-06
	150000	3.82E+19	2.76E-08	3.98E-06
	500000	1.27E+20	2.76E-08	3.98E-06
	1000000	2.55E+20	2.76E-08	3.98E-06

P_aco	Nf
15	1.00E+05
30	1.00E+08
60	1.00E+11
80	1.00E+12
120	1.00E+14
160	1.00E+15
240	1.00E+17
320	1.00E+18
400	1.00E+19
480	1.00E+20

P_aco	T [keV]
15	8.6
30	17.2
60	34.4
80	68.8
120	137.6
160	275.2
240	550.4
320	1100.8
400	2201.6
480	4403.2

Power Lvl [W]	Breakeven	Q = 100
1	2.55E+12	2.55E+14
1.00E+03	2.55E+15	2.55E+17
1.50E+05	3.82E+17	3.82E+19
5.00E+05	1.27E+18	1.27E+20
1.00E+06	2.55E+18	2.55E+20

For Psv6 =   3.62E+10 [W/m^3]   Q=100

Power [W]	Vs [m^3]	Vtotal [m^3]
1000	2.76E-08	3.98E-06
10000	2.76E-07	3.98E-05
50000	1.38E-06	1.99E-04
100000	2.76E-06	3.98E-04
150000	4.14E-06	5.97E-04
200000	5.52E-06	7.96E-04
250000	6.90E-06	9.95E-04
300000	8.28E-06	1.19E-03
350000	9.66E-06	1.39E-03
400000	1.10E-05	1.59E-03
450000	1.24E-05	1.79E-03
500000	1.38E-05	1.99E-03
550000	1.52E-05	2.19E-03

600000	1.66E-05	2.39E-03
650000	1.79E-05	2.59E-03
700000	1.93E-05	2.79E-03
750000	2.07E-05	2.99E-03
800000	2.21E-05	3.18E-03
850000	2.35E-05	3.38E-03
900000	2.48E-05	3.58E-03
950000	2.62E-05	3.78E-03
1000000	2.76E-05	3.98E-03

For Psv5 =   3.62E+07 [W/m^3]   Q=100

Power [W]	Vs [m^3]	Vtotal [m^3]
1000	2.76E-05	3.98E-03
10000	2.76E-04	3.98E-02
50000	1.38E-03	1.99E-01
100000	2.76E-03	3.98E-01
150000	4.14E-03	5.97E-01
200000	5.52E-03	7.96E-01
250000	6.90E-03	9.95E-01
300000	8.28E-03	1.19E+00
350000	9.66E-03	1.39E+00
400000	1.10E-02	1.59E+00
450000	1.24E-02	1.79E+00
500000	1.38E-02	1.99E+00
550000	1.52E-02	2.19E+00
600000	1.66E-02	2.39E+00
650000	1.79E-02	2.59E+00
700000	1.93E-02	2.79E+00
750000	2.07E-02	2.99E+00
800000	2.21E-02	3.18E+00
850000	2.35E-02	3.38E+00
900000	2.48E-02	3.58E+00
950000	2.62E-02	3.78E+00
1000000	2.76E-02	3.98E+00

For Psv1 =   3.62E+05 [W/m^3]   Breakeven

Power [W]	Vs [m^3]	Vtotal [m^3]
1000	2.76E-03	3.98E-01
10000	2.76E-02	3.98E+00
50000	1.38E-01	1.99E+01
100000	2.76E-01	3.98E+01
150000	4.14E-01	5.97E+01

200000	5.52E-01	7.96E+01
250000	6.90E-01	9.95E+01
300000	8.28E-01	1.19E+02
350000	9.66E-01	1.39E+02
400000	1.10E+00	1.59E+02
450000	1.24E+00	1.79E+02
500000	1.38E+00	1.99E+02
550000	1.52E+00	2.19E+02
600000	1.66E+00	2.39E+02
650000	1.79E+00	2.59E+02
700000	1.93E+00	2.79E+02
750000	2.07E+00	2.99E+02
800000	2.21E+00	3.18E+02
850000	2.35E+00	3.38E+02
900000	2.48E+00	3.58E+02
950000	2.62E+00	3.78E+02
1000000	2.76E+00	3.98E+02

For Psv2 = 3.62E+08 [W/m^3] Breakeven

Power [W]	Vs [m^3]	Vtotal [m^3]
1000	2.76E-06	3.98E-04
10000	2.76E-05	3.98E-03
50000	1.38E-04	1.99E-02
100000	2.76E-04	3.98E-02
150000	4.14E-04	5.97E-02
200000	5.52E-04	7.96E-02
250000	6.90E-04	9.95E-02
300000	8.28E-04	1.19E-01
350000	9.66E-04	1.39E-01
400000	1.10E-03	1.59E-01
450000	1.24E-03	1.79E-01
500000	1.38E-03	1.99E-01
550000	1.52E-03	2.19E-01
600000	1.66E-03	2.39E-01
650000	1.79E-03	2.59E-01
700000	1.93E-03	2.79E-01
750000	2.07E-03	2.99E-01
800000	2.21E-03	3.18E-01
850000	2.35E-03	3.38E-01
900000	2.48E-03	3.58E-01
950000	2.62E-03	3.78E-01
1000000	2.76E-03	3.98E-01

Chamber Design 1
Chamber Sizing for a 1 kW Reactor at 1 W Breakeven Power Density Level (Psv1)

Vnew1 =	1.00E+03	% Volume ratio of current to nominal designs
Rnew1 =	0.295077 [m]	% New chamber radius
Hnew1 =	1.455734 [m]	% New Chamber Height
Anew =	0.429554 [m^2]	% 2-D Chamber Geom Area
Vnew1_check =	0.398 [m^3]	% Check to make sure correct volume is used
Paco =	80 [bars]	% Acoustic pressure required for Psv1
Scale1 =	10.00262	% Scaling factor applied to FEMLAB model

Glass
Wall t =	2.5 cm
Max Stress	1.7e6 Pa

Chamber Design 2
Chamber Sizing for a 1 kW Reactor at 1 kW Breakeven Power Density Level (Psv2)

Vnew1 =	1.00E+00	% Volume ratio of current to nominal designs
Rnew1 =	0.029508 [m]	% New chamber radius
Hnew1 =	0.145573 [m]	% New Chamber Height
Anew =	0.004296 [m^2]	% 2-D Chamber Geom Area
Vnew1_check =	0.000398 [m^3]	% Check to make sure correct volume is used
Paco =	160 [bars]	% Acoustic pressure required for Psv1
Scale1 =	1.000262	% Scaling factor applied to FEMLAB model

Glass
Wall t =	2.5 mm
Max Stress	2.5e8 Pa
F =	2.6e8 N

Chamber Design 3
Chamber Sizing for a 1 kW Reactor at 1 W Q=100 Power Density Level (Psv6)

Vnew1 =	1.00E+01	% Volume ratio of current to nominal designs
Rnew1 =	0.063572 [m]	% New chamber radius
Hnew1 =	0.313628 [m]	% New Chamber Height
Anew =	0.019938 [m^2]	% 2-D Chamber Geom Area

Vnew1_check
=   0.00398 [m^3]   % Check to make sure correct volume is used

Paco =   120 [bars]   % Acoustic pressure required for Psv1
                                             % Scaling factor applied to FEMLAB
Scale1 =   2.154999   model

Glass
Wall t =   5.25 mm
Max Stress   3e8 Pa
F =   4.45e7 N

Chamber Design 4
Chamber Sizing for a 1 kW Reactor at 1 kW Q=100 Power Density Level (Psv7)

Vnew1 =   1.00E-02   % Volume ratio of current to nominal designs
Rnew1 =   0.006357 [m]   % New chamber radius
Hnew1 =   0.031363 [m]   % New Chamber Height
Anew =   0.000199 [m^2]   % 2-D Chamber Geom Area
Vnew1_check
=   3.98E-06 [m^3]   % Check to make sure correct volume is used

Paco =   240 [bars]   % Acoustic pressure required for Psv1
                                             % Scaling factor applied to FEMLAB
Scale1 =   0.2155   model

Steel
Wall t =   0.525 mm
Max Stress   3e8 Pa
F =   7.58e9 N

Chamber Design 7: Space Reactor (3 x 175 kW)
Chamber Sizing for a 175 kW Reactor at 1 kW Q=100 Power Density Level (Psv7)

Vnew1 =   1.75E+02   % Volume ratio of current to nominal designs
Rnew1 =   0.16505 [m]   % New chamber radius

Hnew1 =   0.814257 [m]   % New Chamber Height
Anew =   0.134393 [m^2]   % 2-D Chamber Geom Area
Vnew1_check
=   0.06965 [m^3]   % Check to make sure correct volume is used

Paco =   240 [bars]   % Acoustic pressure required for Psv1
                                             % Scaling factor applied to FEMLAB
Scale1 =   5.594909   model

Steel
Wall t =   14mm
Max Stress   5e8 Pa
F =   2.575e7 N

For Psv7 =   3.62E+10 [W/m^3]   Q = 100

Power [W]	Vs [m^3]	Vtotal [m^3]
1000	2.76E-06	3.98E-04
10000	2.76E-05	3.98E-03
50000	1.38E-04	1.99E-02
100000	2.76E-04	3.98E-02
150000	4.14E-04	5.97E-02
175000	4.83E-04	6.97E-02
200000	5.52E-04	7.96E-02
250000	6.90E-04	9.95E-02
300000	8.28E-04	1.19E-01
350000	9.66E-04	1.39E-01
400000	1.10E-03	1.59E-01
450000	1.24E-03	1.79E-01
500000	1.38E-03	1.99E-01
550000	1.52E-03	2.19E-01
600000	1.66E-03	2.39E-01
650000	1.79E-03	2.59E-01
750000	2.07E-03	2.99E-01
800000	2.21E-03	3.18E-01
850000	2.35E-03	3.38E-01
900000	2.48E-03	3.58E-01
950000	2.62E-03	3.78E-01
1000000	2.76E-03	3.98E-01

D-T AICF Reactor Sizing

Assumptions and Constants (for D-T Fusion):

rho =	1.00E+04 [kg/m^3]	% Compressed fluid density
Ni =	5E+29 [Ions/m^3]	% Ion Concentration
<SigmaV>d =	4.50E-25 [m^3/s]	% Weighted Cross-Section for D-T at T
T =	1.00E+08 [K]	% Compressed Temperature
deltaT =	5.00E-13 [s]	% Reaction Time
R =	5.00E-08 [m]	% Compressed Bubble Radius
En =	14.10 [MeV]	% D-D neutron energy
Nbc =	1000.00 [bubbles/cluster]	% Number of bubbles in each cluster
Nbi =	20.00 [bubbles/cluster]	% Number of bubbles per cluster that implode violently
Ncycles =	60.00 [cycles]	% Ave. Number of cycles bubbles expand and collapse
Ncn =	50.00 [clusters/s]	% Number of clusters nucleated per second
Vs =	2.76E-06 [m^3]	% Sensitive volume for nominal setup
Vt =	3.98E-04 [m^3]	% Total volume for nominal setup
Vs/V =	0.007	% Ratio of Sensitive to Total fluid volume
Rc/h =	0.2027	% Ratio of chamber radius to chamber height
1 W =	6.24E+12 [MeV/s]	% Conversion

Calculations for current AICF design (D-T Fusion):

Nn =	7.03 [n/bubble]	% Number of neutrons produced per bubble implosion
Ei =	9.91E+01 [MeV/bubble]	% Neutron Energy Released per Implosion
Nb =	60000 [bubbles/s]	% Number of neutron producing bubbles per second
Vb =	1.66E-01 [m^3*bubbles/s]	% # of n producing bubbles within the Vs produced /s
Rho_b =	2.17E+10 [bubbles/m^3*s]	% Neutron producing bubble density per second
Nf =	421875 [n/s]	% Number of D-D neutrons produced per second
Efn =	5948437.5 [Mev/s]	% Amount of D-D neutron energy produced per second
Esv =	2.16E+12 [MeV/s*m^3]	% Specific Energy produced from sensitive volume
Psv =	3.45E-01 [W/m^3]	% Specific Power for sensitive volume

Calculations for Breakeven (for D-T Fusion):

Neutron production necessary for breakeven at various power levels,

Power Level [W]	1	1.00E+03	1.50E+05	5.00E+05	1.00E+06
Nf [n/s]	4.43E+11	4.43E+14	6.64E+16	2.21E+17	4.43E+17
	1	2	3	4

Assume the following relationship between Nf and the Acoustic Pressure:

Nf [n/s]		1.00E+05	1.00E+08	1.00E+11	1.00E+12	1.00E+14
P [atm]		15	30	60	80	120
T [keV]		8.6	17.2	34.4	68.8	137.6
<sigma*v> [m^3/s]		7.14E-23	2.91E-22	6.55E-22	9.05E-22	8.48E-22
Continued... Nf [n/s]		1.00E+15	1.00E+17	1.00E+18	1.00E+19	1.00E+20
P [atm]		160	240	320	400	480
T [keV]		275.2	550.4	1100.8	2201.6	4403.2
<sigma*v> [m^3/s]		5.98E-22	3.51E-22	1.90E-22	1.05E-22	6.52E-23

Efn1 =	6.24E+12 [Mev/s]	% D-T neutron energy produced per second for 1 kW
Efn2 =	6.24E+15 [Mev/s]	% D-T neutron energy produced per second for 1 kW
Efn3 =	9.36E+17 [Mev/s]	% D-T neutron energy produced per second for 150 kW
Efn4 =	3.12E+18 [Mev/s]	% D-T neutron energy produced per second for 500 kW
Efn5 =	6.24E+18 [Mev/s]	% D-T neutron energy produced /s for 1 MW
Esv1 =	2.26E+18 [MeV/s*m^3]	% Energy density produced from Vs for 1W
Esv2 =	2.26E+21 [MeV/s*m^3]	% Energy density produced from Vs for 1kW
Esv3 =	3.39E+23 [MeV/s*m^3]	% Energy density produced from sVs for 150 kW
Esv4 =	1.13E+24 [MeV/s*m^3]	% Energy density produced from Vs for 500 kW
Esv5 =	2.26E+24 [MeV/s*m^3]	% Energy density produced from Vs for 1MW
Psv1 =	3.62E+05 [W/m^3]	% Power density for sensitive volume for 1 W
Psv2 =	3.62E+08 [W/m^3]	% Power density for sensitive volume for 1 kW
Psv3 =	5.43E+10 [W/m^3]	% Power density for sensitive volume for 150 kW
Psv4 =	1.81E+11 [W/m^3]	% Power density for sensitive volume for 500 kW
Psv5 =	3.62E+11 [W/m^3]	% Power density for sensitive volume for 1 MW

1 W			1 kW		
Nf =	4.43E+11		Nf =	4.43E+14	
Nn =	14140.63		Nn =	9343.75	
Nb =	3.13E+07		Nb =	4.74E+10	

Calculations for Q=100 (for D-T Fusion):

Neutron production necessary for Q = 100 at various power levels,

Power Level [W]		1	1.00E+03	1.50E+05	5.00E+05	1.00E+06
Nf [n/s]		4.43E+13	4.43E+16	6.64E+18	2.21E+19	4.43E+19

Efn6 =	6.24E+14 [Mev/s]	% D-T neutron energy produced per second for 1 kW
Efn7 =	6.24E+17 [Mev/s]	% D-T neutron energy produced per second for 1 kW
Efn8 =	9.36E+19 [Mev/s]	% D-T neutron energy produced per second for 150 kW
Efn9 =	3.12E+20 [Mev/s]	% D-T neutron energy produced per second for 500 kW
Efn10 =	6.24E+20 [Mev/s]	% D-T neutron energy produced /s for 1 MW
Esv6 =	2.26E+20 [MeV/s*m^3]	% Energy density produced from Vs for 1W
Esv7 =	2.26E+23 [MeV/s*m^3]	% Energy density produced from Vs for 1kW
Esv8 =	3.39E+25 [MeV/s*m^3]	% Energy density produced from sVs for 150 kW

Esv9 =	1.13E+26 [MeV/s*m^3]	% Energy density produced from Vs for 500 kW	
Esv10 =	2.26E+26 [MeV/s*m^3]	% Energy density produced from Vs for 1MW	
Psv6 =	3.62E+07 [W/m^3]	% Power density for sensitive volume for 1 W	
Psv7 =	3.62E+10 [W/m^3]	% Power density for sensitive volume for 1 kW	
Psv8 =	5.43E+12 [W/m^3]	% Power density for sensitive volume for 150 kW	
Psv9 =	1.81E+13 [W/m^3]	% Power density for sensitive volume for 500 kW	
Psv10 =	3.62E+13 [W/m^3]	% Power density for sensitive volume for 1 MW	

1 W		1 kW	
Nf =	4.43E+13	Nf =	4.43E+16
Nn =	13250.00	Nn =	5484.38
Nb =	3.34E+09	Nb =	8.07E+12

Reactor Sizing

	Reactor P [W]	Nf [n/s]	Vs [m^3]	Vtotal [m^3]
Currently	1000	1.70E+05	2.90E+03	4.14E+05
	150000	1.70E+05	4.34E+05	6.21E+07
	500000	1.70E+05	1.45E+06	2.07E+08
	1000000	1.70E+05	2.90E+06	4.14E+08
Breakeven	1000	4.43E+14	2.76E-06	3.94E-04
	150000	6.64E+16	2.76E-06	3.94E-04
	500000	2.21E+17	2.76E-06	3.94E-04
	1000000	4.43E+17	2.76E-06	3.94E-04
Q = 100	1000	4.43E+16	2.76E-08	3.94E-06
	150000	6.64E+18	2.76E-08	3.94E-06
	500000	2.21E+19	2.76E-08	3.94E-06
	1000000	4.43E+19	2.76E-08	3.94E-06

P_aco	Nf
15	1.00E+05
30	1.00E+08
60	1.00E+11
80	1.00E+12
120	1.00E+14
160	1.00E+15
240	1.00E+17
320	1.00E+18
400	1.00E+19
480	1.00E+20

P_aco	T [keV]
15	8.6
30	17.2
60	34.4
80	68.8
120	137.6
160	275.2
240	550.4
320	1100.8
400	2201.6
480	4403.2

Power Lvl [W]	Breakeven	Q = 100
1	2.54776E+12	2.5478E+14
1000	2.54776E+15	2.5478E+17
10000	3.82163E+17	3.8216E+19
100000	1.27388E+18	1.2739E+20
1000000	2.54776E+18	2.5478E+20

For Psv6 =   3.62E+10 [W/m^3]   Q=100

Power [W]	Vs [m^3]	Vtotal [m^3]
1000	2.76E-08	3.94E-06
10000	2.76E-07	3.94E-05
50000	1.38E-06	1.97E-04
100000	2.76E-06	3.94E-04
150000	4.14E-06	5.91E-04
200000	5.52E-06	7.89E-04
250000	6.90E-06	9.86E-04
300000	8.28E-06	1.18E-03
350000	9.66E-06	1.38E-03
400000	1.10E-05	1.58E-03
450000	1.24E-05	1.77E-03
500000	1.38E-05	1.97E-03
550000	1.52E-05	2.17E-03
600000	1.66E-05	2.37E-03
650000	1.79E-05	2.56E-03
700000	1.93E-05	2.76E-03
750000	2.07E-05	2.96E-03
800000	2.21E-05	3.15E-03
850000	2.35E-05	3.35E-03
900000	2.48E-05	3.55E-03
950000	2.62E-05	3.75E-03
1000000	2.76E-05	3.94E-03

For Psv5 = 3.62E+07 [W/m^3]   Q=100

Power [W]	Vs [m^3]	Vtotal [m^3]
1000	2.76E-05	3.94E-03
10000	2.76E-04	3.94E-02
50000	1.38E-03	1.97E-01
100000	2.76E-03	3.94E-01
150000	4.14E-03	5.91E-01
200000	5.52E-03	7.89E-01
250000	6.90E-03	9.86E-01
300000	8.28E-03	1.18E+00
350000	9.66E-03	1.38E+00
400000	1.10E-02	1.58E+00
450000	1.24E-02	1.77E+00
500000	1.38E-02	1.97E+00
550000	1.52E-02	2.17E+00
600000	1.66E-02	2.37E+00
650000	1.79E-02	2.56E+00
700000	1.93E-02	2.76E+00
750000	2.07E-02	2.96E+00
800000	2.21E-02	3.15E+00

850000	2.35E-02	3.35E+00
900000	2.48E-02	3.55E+00
950000	2.62E-02	3.75E+00
1000000	2.76E-02	3.94E+00

For Psv1 = 3.62E+05 [W/m^3] Breakeven

Power [W]	Vs [m^3]	Vtotal [m^3]
1000	2.76E-03	3.94E-01
10000	2.76E-02	3.94E+00
50000	1.38E-01	1.97E+01
100000	2.76E-01	3.94E+01
150000	4.14E-01	5.91E+01
200000	5.52E-01	7.89E+01
250000	6.90E-01	9.86E+01
300000	8.28E-01	1.18E+02
350000	9.66E-01	1.38E+02
400000	1.10E+00	1.58E+02
450000	1.24E+00	1.77E+02
500000	1.38E+00	1.97E+02
550000	1.52E+00	2.17E+02
600000	1.66E+00	2.37E+02
650000	1.79E+00	2.56E+02
700000	1.93E+00	2.76E+02
750000	2.07E+00	2.96E+02
800000	2.21E+00	3.15E+02
850000	2.35E+00	3.35E+02
900000	2.48E+00	3.55E+02
950000	2.62E+00	3.75E+02
1000000	2.76E+00	3.94E+02

For Psv2 = 3.62E+08 [W/m^3] Breakeven

Power [W]	Vs [m^3]	Vtotal [m^3]
1000	2.76E-06	3.94E-04
10000	2.76E-05	3.94E-03
50000	1.38E-04	1.97E-02
100000	2.76E-04	3.94E-02
150000	4.14E-04	5.91E-02
200000	5.52E-04	7.89E-02
250000	6.90E-04	9.86E-02
300000	8.28E-04	1.18E-01
350000	9.66E-04	1.38E-01
400000	1.10E-03	1.58E-01

450000	1.24E-03	1.77E-01
500000	1.38E-03	1.97E-01
550000	1.52E-03	2.17E-01
600000	1.66E-03	2.37E-01
650000	1.79E-03	2.56E-01
700000	1.93E-03	2.76E-01
750000	2.07E-03	2.96E-01
800000	2.21E-03	3.15E-01
850000	2.35E-03	3.35E-01
900000	2.48E-03	3.55E-01
950000	2.62E-03	3.75E-01
1000000	2.76E-03	3.94E-01

Power Level [W]	D -He3 Nf [n/s]	D-D	D-T
1	4.24626E+11	2.5478E+12	4.427E+11
1000	4.24626E+14	2.5478E+15	4.427E+14
150000	6.36939E+16	3.8216E+17	6.64E+16
500000	2.12313E+17	1.2739E+18	2.213E+17
1000000	4.24626E+17	2.5478E+18	4.427E+17

Chamber Design 5
Chamber Sizing for a 1 MW Reactor at 1 W Q = 100 Power Density Level (Psv7)

Vnew1 =	9.91E+03	% Volume ratio of current to nominal designs
Rnew1 =	0.633740868 [m]	% New chamber radius
Hnew1 =	3.126496635 [m]	% New Chamber Height
Anew =	1.98138869 [m^2]	% 2-D Chamber Geom Area
Vnew1_check =	3.942857143 [m^3]	% Check to make sure correct volume is used
Paco =	100 [bars]	% Acoustic pressure required for Psv1
Scale1 =	21.48274128	% Scaling factor applied to FEMLAB model

Steel
Wall t =	5 cm
Max Stress	1e7 Pa
F =	3.83e7 N

D-He3 AICF Reactor Sizing

Assumptions and Constants (for D-He3 Fusion):

rho =	1.00E+04	[kg/m^3]	% Compressed fluid density
Ni =	5E+29	[Ions/m^3]	% Ion Concentration
<SigmaV>d =	1.47E-25	[m^3/s]	% Weighted Cross-Section for D-T at T
T =	1.00E+08	[K]	% Compressed Temperature
deltaT =	5.00E-13	[s]	% Reaction Time
R =	5.00E-08	[m]	% Compressed Bubble Radius
En =	14.70	[MeV]	% D-He3 proton energy
Nbc =	1000.00	[bubbles/cluster]	% Number of bubbles in each cluster
Nbi =	20.00	[bubbles/cluster]	% Number of bubbles per cluster that implode violently
Ncycles =	60.00	[cycles]	% Ave. Number of cycles bubbles expand and collapse
Ncn =	50.00	[clusters/s]	% Number of clusters nucleated per second
Vs =	2.76E-06	[m^3]	% Sensitive volume for nominal setup
Vt =	3.98E-04	[m^3]	% Total volume for nominal setup
Vs/V =	0.007		% Ratio of Sensitive to Total fluid volume
Rc/h =	0.2027		% Ratio of chamber radius to chamber height
1 W =	6.24E+12	[MeV/s]	% Conversion

Calculations for current AICF design (D-He3 Fusion):

Nn =	2.30	[n/bubble]	% Number of protons produced per bubble implosion
Ei =	3.38E+01	[MeV/bubble]	% Proton Energy Released per Implosion
Nb =	60000	[bubbles/s]	% Number of proton producing bubbles per second
Vb =	1.66E-01	[m^3*bubbles/s]	% # of p producing bubbles within the Vs produced per s
Rho_b =	2.17E+10	[bubbles/m^3*s]	% Proton producing bubble density per second
Nf =	137812.5	[n/s]	% Number of D-He3 protons produced per second
Efn =	2025843.8	[Mev/s]	% Amount of D-He3 proton energy produced per second
Esv =	7.34E+11	[MeV/s*m^3]	% Energy Density produced from sensitive volume
Psv =	1.18E-01	[W/m^3]	% Power density for sensitive volume

Calculations for Breakeven (for D-He3 Fusion):

Proton production necessary for breakeven at various power levels,

Power Level [W]	1	1.00E+03	1.50E+05	5.00E+05	1.00E+06
Nf [n/s]	4.25E+11	4.25E+14	6.37E+16	2.12E+17	4.25E+17
		1	2	3	4

Assume the following relationship between Nf and the Acoustic Pressure:

	Nf [n/s]	1.00E+05	1.00E+08	1.00E+11	1.00E+12	1.00E+14
	P [atm]	15	30	60	80	120
	T [keV]	8.6	17.2	34.4	68.8	137.6
	<sigma*v> [m^3/s]	1.47E-25	2.66E-24	2.09E-23	8.14E-23	1.80E-23
Continued…	Nf [n/s]	1.00E+15	1.00E+17	1.00E+18	1.00E+19	1.00E+20
	P [atm]	160	240	320	400	480
	T [keV]	275.2	550.4	1100.8	2201.6	4403.2
	<sigma*v> [m^3/s]	2.57E-22	2.71E-22	2.42E-22	2.09E-22	1.99E-22

Efn1 =	6.24E+12 [Mev/s]	% D-He3 proton energy produced per second for 1 kW
Efn2 =	6.24E+15 [Mev/s]	% D-He3 proton energy produced per second for 1 kW
Efn3 =	9.36E+17 [Mev/s]	% D-He3 proton energy produced per second for 150 kW
Efn4 =	3.12E+18 [Mev/s]	% D-He3 proton energy produced per second for 500 kW
Efn5 =	6.24E+18 [Mev/s]	% D-He3 proton energy produced per second for 1 MW
Esv1 =	2.26E+18 [MeV/s*m^3]	% Energy density produced from sensitive volume for 1W
Esv2 =	2.26E+21 [MeV/s*m^3]	% Energy density produced from sensitive volume for 1kW
Esv3 =	3.39E+23 [MeV/s*m^3]	% Energy density produced from Vs for 150 kW
Esv4 =	1.13E+24 [MeV/s*m^3]	% Energy density produced from Vs for 500 kW
Esv5 =	2.26E+24 [MeV/s*m^3]	% Energy density produced from sensitive volume for 1MW
Psv1 =	3.62E+05 [W/m^3]	% Power density for sensitive volume for 1 W
Psv2 =	3.62E+08 [W/m^3]	% Power density for sensitive volume for 1 kW
Psv3 =	5.43E+10 [W/m^3]	% Power density for sensitive volume for 150 kW
Psv4 =	1.81E+11 [W/m^3]	% Power density for sensitive volume for 500 kW
Psv5 =	3.62E+11 [W/m^3]	% Power density for sensitive volume for 1 MW

1 W			1 kW	
Nf =	4.25E+11		Nf =	4.25E+14
Nn =	326.56		Nn =	281.25
Nb =	1.30E+09		Nb =	1.51E+12

Calculations for Q=100 (for D-He3 Fusion):

Proton production necessary for Q = 100 at various power levels,

Power Level [W]	1	1.00E+03	1.50E+05	5.00E+05	1.00E+06
Nf [n/s]	4.25E+13	4.25E+16	6.37E+18	2.12E+19	4.25E+19

Efn6 =	6.24E+14 [Mev/s]	% D-He3 proton energy produced per second for 1 kW
Efn7 =	6.24E+17 [Mev/s]	% D-He3 proton energy produced per second for 1 kW
Efn8 =	9.36E+19 [Mev/s]	% D-He3 proton energy produced per second for 150 kW
Efn9 =	3.12E+20 [Mev/s]	% D-He3 proton energy produced per second for 500 kW
Efn10 =	6.24E+20 [Mev/s]	% D-He3 proton energy produced per second for 1 MW
Esv6 =	2.26E+20 [MeV/s*m^3]	% Energy density produced from sensitive volume for 1W

Esv7 =	2.26E+23 [MeV/s*m^3]	% Energy density produced from sensitive volume for 1kW
Esv8 =	3.39E+25 [MeV/s*m^3]	% Energy density produced from Vs for 150 kW
Esv9 =	1.13E+26 [MeV/s*m^3]	% Energy density produced from Vs for 500 kW
Esv10 =	2.26E+26 [MeV/s*m^3]	% Energy density produced from sensitive volume for 1MW

Psv6 =	3.62E+07 [W/m^3]	% Power density for sensitive volume for 1 W
Psv7 =	3.62E+10 [W/m^3]	% Power density for sensitive volume for 1 kW
Psv8 =	5.43E+12 [W/m^3]	% Power density for sensitive volume for 150 kW
Psv9 =	1.81E+13 [W/m^3]	% Power density for sensitive volume for 500 kW
Psv10 =	3.62E+13 [W/m^3]	% Power density for sensitive volume for 1 MW

1 W			1 kW	
Nf =	4.25E+13		Nf =	4.25E+16
Nn =	281.25		Nn =	4234.38
Nb =	1.51E+11		Nb =	1.00E+13

Reactor Sizing

	Reactor P [W]	Nf [n/s]	Vs [m^3]	Vtotal [m^3]
Currently	1000	1.70E+05	8.50E+03	1.21E+06
	150000	1.70E+05	1.28E+06	1.82E+08
	500000	1.70E+05	4.25E+06	6.07E+08
	1000000	1.70E+05	8.50E+06	1.21E+09
Breakeven	1000	4.25E+14	2.76E-06	3.94E-04
	150000	6.37E+16	2.76E-06	3.94E-04
	500000	2.12E+17	2.76E-06	3.94E-04
	1000000	4.25E+17	2.76E-06	3.94E-04
Q = 100	1000	4.25E+16	2.76E-08	3.94E-06
	150000	6.37E+18	2.76E-08	3.94E-06
	500000	2.12E+19	2.76E-08	3.94E-06
	1000000	4.25E+19	2.76E-08	3.94E-06

P_aco   Nf

15	1.00E+05
30	1.00E+08
60	1.00E+11
80	1.00E+12
120	1.00E+14
160	1.00E+15
240	1.00E+17
320	1.00E+18
400	1.00E+19
480	1.00E+20

P_aco	T [keV]
15	8.6
30	17.2
60	34.4
80	68.8
120	137.6
160	275.2
240	550.4
320	1100.8
400	2201.6
480	4403.2

Power Lvl [W]	Breakeven	Q = 100
1	4.25E+11	4.25E+13
1.00E+03	4.25E+14	4.25E+16
1.50E+05	6.37E+16	6.37E+18
5.00E+05	2.12E+17	2.12E+19
1.00E+06	4.25E+17	4.25E+19

For Psv6 = 3.62E+10 [W/m^3]   Q=100

Power [W]	Vs [m^3]	Vtotal [m^3]
1000	2.76E-08	3.94E-06
10000	2.76E-07	3.94E-05
50000	1.38E-06	1.97E-04
100000	2.76E-06	3.94E-04
150000	4.14E-06	5.91E-04
200000	5.52E-06	7.89E-04
250000	6.90E-06	9.86E-04
300000	8.28E-06	1.18E-03
350000	9.66E-06	1.38E-03
400000	1.10E-05	1.58E-03

450000	1.24E-05	1.77E-03
500000	1.38E-05	1.97E-03
550000	1.52E-05	2.17E-03
600000	1.66E-05	2.37E-03
650000	1.79E-05	2.56E-03
700000	1.93E-05	2.76E-03
750000	2.07E-05	2.96E-03
800000	2.21E-05	3.15E-03
850000	2.35E-05	3.35E-03
900000	2.48E-05	3.55E-03
950000	2.62E-05	3.75E-03
1000000	2.76E-05	3.94E-03

For Psv5 =   3.62E+07 [W/m^3]   Q=100

Power [W]	Vs [m^3]	Vtotal [m^3]
1000	2.76E-05	3.94E-03
10000	2.76E-04	3.94E-02
50000	1.38E-03	1.97E-01
100000	2.76E-03	3.94E-01
150000	4.14E-03	5.91E-01
200000	5.52E-03	7.89E-01
250000	6.90E-03	9.86E-01
300000	8.28E-03	1.18E+00
350000	9.66E-03	1.38E+00
400000	1.10E-02	1.58E+00
450000	1.24E-02	1.77E+00
500000	1.38E-02	1.97E+00
550000	1.52E-02	2.17E+00
600000	1.66E-02	2.37E+00
650000	1.79E-02	2.56E+00
700000	1.93E-02	2.76E+00
750000	2.07E-02	2.96E+00
800000	2.21E-02	3.15E+00
850000	2.35E-02	3.35E+00
900000	2.48E-02	3.55E+00
950000	2.62E-02	3.75E+00
1000000	2.76E-02	3.94E+00

For Psv1 =   3.62E+05 [W/m^3]   Breakeven

Power [W]	Vs [m^3]	Vtotal [m^3]
1000	2.76E-03	3.94E-01
10000	2.76E-02	3.94E+00
50000	1.38E-01	1.97E+01
100000	2.76E-01	3.94E+01
150000	4.14E-01	5.91E+01
200000	5.52E-01	7.89E+01
250000	6.90E-01	9.86E+01
300000	8.28E-01	1.18E+02
350000	9.66E-01	1.38E+02
400000	1.10E+00	1.58E+02
450000	1.24E+00	1.77E+02
500000	1.38E+00	1.97E+02
550000	1.52E+00	2.17E+02
600000	1.66E+00	2.37E+02
650000	1.79E+00	2.56E+02
700000	1.93E+00	2.76E+02
750000	2.07E+00	2.96E+02
800000	2.21E+00	3.15E+02
850000	2.35E+00	3.35E+02
900000	2.48E+00	3.55E+02
950000	2.62E+00	3.75E+02
1000000	2.76E+00	3.94E+02

For Psv2 = 3.62E+08 [W/m^3]   Breakeven

Power [W]	Vs [m^3]	Vtotal [m^3]
1000	2.76E-06	3.94E-04
10000	2.76E-05	3.94E-03
50000	1.38E-04	1.97E-02
100000	2.76E-04	3.94E-02
150000	4.14E-04	5.91E-02
200000	5.52E-04	7.89E-02
250000	6.90E-04	9.86E-02
300000	8.28E-04	1.18E-01
350000	9.66E-04	1.38E-01
400000	1.10E-03	1.58E-01
450000	1.24E-03	1.77E-01
500000	1.38E-03	1.97E-01
550000	1.52E-03	2.17E-01
600000	1.66E-03	2.37E-01
650000	1.79E-03	2.56E-01
700000	1.93E-03	2.76E-01
750000	2.07E-03	2.96E-01

800000	2.21E-03	3.15E-01
850000	2.35E-03	3.35E-01
900000	2.48E-03	3.55E-01
950000	2.62E-03	3.75E-01
1000000	2.76E-03	3.94E-01

Power Level [W]	D -He3 Nf [n/s]	D-D
1	4.246E+11	2.548E+12
1000	4.246E+14	2.548E+15
150000	6.369E+16	3.822E+17
500000	2.123E+17	1.274E+18
1000000	4.246E+17	2.548E+18

Chamber Design 6

Chamber Sizing for a 1 MW Reactor at 1 W Q = 100 Power Density Level (Psv7)

Vnew1 =	9.91E+03	% Volume ratio of current to nominal designs
Rnew1 =	0.6337409 [m]	% New chamber radius
Hnew1 =	3.1264966 [m]	% New Chamber Height
Anew =	1.9813887 [m^2]	% 2-D Chamber Geom Area
Vnew1_check =	3.9428571 [m^3]	% Check to make sure correct volume is used
Paco =	100 [bars]	% Acoustic pressure required for Psv1
Scale1 =	21.482741	% Scaling factor applied to FEMLAB model

Appendix C

Supporting Publications

BUBBLE DYNAMICS AND TRITIUM EMISSION DURING BUBBLE FUSION EXPERIMENTS

Yiban Xu[1]
School of Nuclear Engineering, Purdue University, West Lafayette, IN 47907 USA
yiban@ecn.purdue.edu

Adam Butt
School of Aeronautical and Astronautical Engineering, School of Nuclear Engineering, Purdue
University, West Lafayette, IN 47907 USA
butt@purdue.edu

Shripad T. Revankar
School of Nuclear Engineering, Purdue University, West Lafayette, IN 47907 USA
shripad@ecn.purdue.edu

ABSTRACT

Neutron nucleated, transient bubble cluster dynamics has been studied through direct observations of shock wave and sonoluminescence (SL) signals. Confirmatory bubble fusion-related neutron-seeded acoustic cavitation experiments were conducted with deuterated acetone (C_3D_6O) and non-deuterated acetone (C_3H_6O). Tritium emission monitoring was performed systematically by using a calibrated state-of-the-art Beckman LS6500 beta spectrometer for the samples obtained from bubble fusion experiments of non-deuterated and deuterated acetone with and without cavitation. Statistically significant tritium emission was observed during neutron-seeded acoustic cavitation experiments with deuterated acetone, but not for control experiments involving non-deuterated acetone, nor with irradiation alone, thereby confirming reported observations for the occurrence of thermonuclear fusion reactions in deuterium-bearing imploding cavitation bubbles. Thermal hydraulic conditions of bubble implosions leading to robust SL emission are discussed.

KEYWORDS

Bubble fusion, bubble cluster dynamics, tritium counting.

1. INTRODUCTION

Thermonuclear fusion reactions in imploding bubbles (so called bubble fusion) were observed and reported by Taleyarkhan and his coworkers (Taleyarkhan et al., 2002,2004a; Nigmatulin et al., 2004) but so far have not been confirmed by others. Thermonuclear fusion in highly compressed bubbles is possible only when appropriate conditions are provided: high enough (~1000 Mbar) pressure and (~ 10^7K) temperature and the presence of deuterium (D) atoms which need to be forced close enough, and need to stay together for a sufficient time to permit them to become fused (Gross, 1984). Theoretically, these conditions have been predicted to occur (Moss, 1996; Nigmatulin et al., 2004; Wu, 1993; Taleyarkhan et al., 2004b) and highly depend on bubble dynamics: how these bubbles initiate, grow and implode. As is evident, implosions of spherical bubbles produce stronger shock wave compression than aspherical ones; the maximum bubble volume is not only a function of the acoustic pressure amplitude, but can also be affected by the timing of the bubble nucleation (Taleyarkhan, 2004b). Therefore, a comprehensive understanding of bubble dynamics as well as

---

[1] Corresponding author

related control variables will be crucial for successful bubble fusion experiments and for future development and optimization of bubble fusion technology.

The process of bubble nucleation, growth and collapse is nonlinear and complicated in general, involving thermal, mechanical, optical, chemical or even nuclear scale phenomena. Depending on the acoustic driving amplitude, a bubble could grow in volume in several acoustic cycles and collapse within one cycle. Huge potential energy accumulated during its growth time can be converted into thermal energy to heat up the bubble's internal contents by shock wave compression. The temperature inside the bubble could be more than 100 million degrees (Nigmatulin et al., 2004) and high enough to accelerate chemical reactions and even cause nuclear fusion reactions. This shock wave continues to propagate in the liquid after the bubble collapses and the evidence can be detected on the chamber walls by an ordinary microphone.

The issue of bubble nuclear fusion thermal-hydraulics becomes even more complicated when a nucleated single bubble grows from ~50 nm by factors of ~100,000 to a large (1000 μm) bubble then implodes and breaks into a cluster of tiny bubbles (Brennan, 1995). These tiny bubbles can stay together as clusters when an acoustic standing wave is applied. From experimental and numerical analyses (Taleyarkhan et al., 2004b) bubble cluster formation can lead to pressure intensification for inner bubbles, causing much higher temperatures and pressures for the bubbles in the center of the cluster than for a single individual bubble. This is attributed to acoustic streaming effects of the shock wave produced by the bubbles along the edge of the cluster (Matsumoto, 2004). Recent experiments (Camara et al; 2004) to evaluate temperatures below the surface of SL bubbles has revealed clearly that the emission spectra from the interior resemble those given out by Bremstrahhlung radiation composed of excited plasmas in the 10^6K range. Another study to directly demonstrate the existence of plasmas in SL bubbles has recently been published (Flanigan and Suslick, 2005). Evidently, the assessment of the relative effects of bubble cluster appears crucial for understanding conditions relevant for attaining bubble nuclear fusion, and scale-up of bubble fusion dynamics. This was therefore, attempted for which salient results are presented in this paper.

An important consideration in such experiments to evaluate the occurrence of nuclear fusion involves experimental evidence of key signatures. Notably, for bubble fusion experiments (Taleyarkhan et al., 2002, 2004a) the bubble collapse time is so short and the final bubble size during implosion is so small that any attempts of measuring the variables inside a bubble are extremely difficult, if not impossible. Therefore, indirect approaches must be used to identify the possible nuclear fusion reactions in a collapsing bubble. The well-known D-D nuclear fusion reaction proceeds in two branches of roughly equal probability as (Gross, 1984)

$$D + D = \begin{cases} n + {}^3He \\ p + T \end{cases} \qquad (1)$$

The products of D-D fusion reaction are: a neutron (n), a proton (p), Helium (He) and tritium (T). Helium (^{3}He) is a non-radioactive gas and it is difficult to detect and the MeV energy protons (due to them being charged particles) can travel no more than ~1 mm through the test fluid and before getting absorbed. On the other hand neutrons (being uncharged particles) can escape from the test cell, and tritium is a radioactive isotope readily detectable using beta-spectrometry. Therefore, neutrons and tritium become the candidates for fusion reaction detection in bubble fusion experiments as reported by Taleyarkhan et al. (2002, 2004a). However, in bubble fusion experiments, it is to be realized that neutron detection can become difficult due to the presence of large gamma ray fields resulting from the neutrons used to seed bubbles. This requires sensitive on-line detection equipment which can distinguish neutrons from gamma rays, and also distinguish neutrons from nuclear fusion from those neutrons used for seeding bubbles from an external neutron source (PNG or isotopic source). Such issues and complexities are non-existent when monitoring for the radioactive isotope tritium.

This paper focuses on reporting investigations on two aspects of bubble nuclear fusion: transient bubble dynamics along with SL light emission, and tritium production. These two topics are presented separately. The first part of this manuscript discusses observations of bubble thermal-hydraulics during the simulated bubble fusion experiments. These observations were obtained in a desktop test

apparatus with isotope neutron-seeding of cavitation nuclei in a test cell. The second part provides confirmatory evidence of tritium emission during neutron seeded acoustic cavitation of deuterated acetone, along with evidence of null results from control experiments.

2. EXPERIMENTAL APPARATUS AND APPROACH

The bubble dynamics experiments were performed in a test apparatus (see Figure 1) similar to what was used by Taleyarkhan et al. (2002, 2004a). The test chamber was placed in a chilled light-tight enclosure. A microphone (MIC) was attached to the outside wall of the chamber for shock wave detection (indicative of bubble implosions) for which the low frequency components were filtered out for counting of cavitation rate. A photomultiplier tube (PMT) was placed ~1 cm away from the test chamber for sonoluminescence (SL) light detection. The PMT was powered by a high voltage supply at -2000 volts and its output was first sent to a preamplifier (ORTEC 113) and then to an amplifier (ORTEC 570). The fluid (normal acetone) was driven and experienced positive and negative pressures at a frequency of ~20 kHz by the acoustic wave generated from a PZT ring epoxied on the chamber. An isotope neutron source (Cf-252 0.5 mCi) was used to seed nuclei in the fluid. A high speed video camera (Fastcam 10K) was used to visualize the bubble behavior.

Following the methods reported elsewhere (Taleyarkhan et al., 2002) before conducting bubble fusion experiments the test cell drive amplitude corresponding to about -7bar for nucleation from multi-MeV neutrons was evaluated after degassing. That is, no bubble nucleation would occur at this acoustic drive power over a waiting time of ~ 30s in the absence of the neutron source. Thereafter, after the baseline drive amplitude was doubled to be ~ +/- 15 bars for each of the cavitation runs (as used by Taleyarkhan et al., 2002, 2004a).

It is well-known that tritium is an extremely rare isotope and can only be produced by via nuclear reactions and hence, becomes a powerful indicator for possible thermonuclear fusion reactions during bubble fusion experiments. Tritium can be examined for its presence in the test fluid after the experiment, but this requires access to expensive and sensitive beta spectrometers. Fortunately, as part of the infrastructure we had access to a state-of-the-art beta spectrometer system, the Beckman LS6500^{TM} system at Purdue University, which was similar to that used in the reported bubble fusion studies at Oak Ridge National Laboratory (Taleyarkhan et al., 2002, 2004a). Therefore, we focused on monitoring for tritium emission during acoustic cavitation experiments to confirm the possible occurrence of bubble nuclear fusion. Along with D-D nuclear fusion producing tritium, it is well-known that D atoms in a deuterated liquid can become transmuted to T atoms in the presence of a very high flux of neutrons (as in a commercial power nuclear reactor). Fortunately, in bubble nuclear fusion experiments transmuting D atoms to T atoms by neutron bombardment is a second order effect, a fact which can be readily validated via conduct of control experiments (i.e., experiments conducted to note changes in tritium content of the test liquid by subjecting the test cell to the same experimental neutron fluence used for seeding bubbles, but without acoustic power turned on such that cavitation is not present). Control experiments were also to be performed under identical experimental conditions, but changing only one parameter at a time (e.g., cavitation on vs. off; alternately, change H bearing liquid to D bearing liquid). The control experiments include non-deuterated fluid tests along with cavitation on or off tests. Evidence for thermonuclear fusion reactions (from tritium emission) in a collapsed bubble needs to manifest only for neutron-seeded cavitation in a deuterated fluid. All tests with a non-deuterated fluid or a test with deuterated fluid without cavitation should not lead to tritium production.
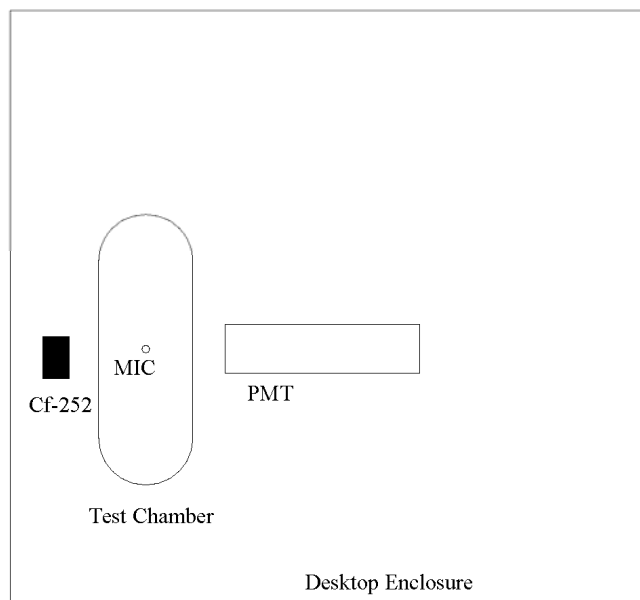
Figure 1: Schematic of experimental apparatus layout (not scaled). Cf-252 – Isotope Neutron Source (0.5 mCi); MIC – Microphone; PMT – Photomultiplier Tube.

3.   RESULTS OF BUBBLE DYNAMICS

Following the published approach by Taleyarkhan (Taleyarkhan et al., 2002 and 2004a), the fluid was first properly degassed for about 2 hrs until individual cavitation bubble clusters were achieved. During such evolution, sharp (N-shaped) shock traces were observed on the high-speed digital storage oscilloscope screen coming from the microphone and the PMT. The bubble dynamic behavior has been studied as follows: cavitation visualization by using a high speed video camera (Fastcam 10K), shock wave detection by using a microphone attached on the outside wall of the test chamber and sonoluminescence light emission by using a photomultiplier tube. Typical results are illustrated in the following subsections.

3.1 Cavitation Visualization

Figure 2 displays a typical image sequence of a cavitation bubble cluster of non-deuterated acetone nucleation seeded by neutrons from a Cf-252 isotope source (0.5 mCi of activity) and experienced pressures at ~+/- 17 bars driven by acoustic waves. Note that the images were taken at a speed of 5000 frames per second and 1/20000 s for shutter speed. Since the camera frame speed is smaller than that of the chamber driving frequency, it is believed that the bubble is actually a bubble cluster, which can be verified by quickly turning off the acoustic driving power. The bubble cluster which was otherwise held in place by the acoustic pressure field breaks apart and results in a dispersion of several tiny (~10^2 μm) bubbles. Also, direct numerical simulations for bubble growth using the well established Rayleigh-Plesset formulation indicates that an individual bubble that can reach a maximum of only ~400 μm (Nigmatulin et al., 2002), whereas the size of individual clusters is about 10 times

larger. The images were compensated for the distortion due to the optical deflection from a cylindrical surface and its scale is about 0.083 mm/pixel. The bubble cluster diameters in the first three images at t=0.0, 0.2 and 0.6 ms are about 0.6, 2.7 and 3.4 mm, respectively. The first appearance of contraction (perhaps because some of the bubbles in the cluster were imploded in this frame) is seen at t=0.8 ms. The cluster size did not vary much after the first contraction and was diffused out after 3 ms.

Figure3 shows another type of cavitation consisting of comet-like streamers. Unlike that of individual bubble clusters, the structure of a streamer appears continuous in space and time: bubbles were formed at one end (bottom end in this figure) and ejected outwards from the other end and could last as long as 10 s. Interestingly, and importantly, it was observed that streamers produce neither distinct shock wave peaks in the microphone nor SL light emission. This is described in the next section.
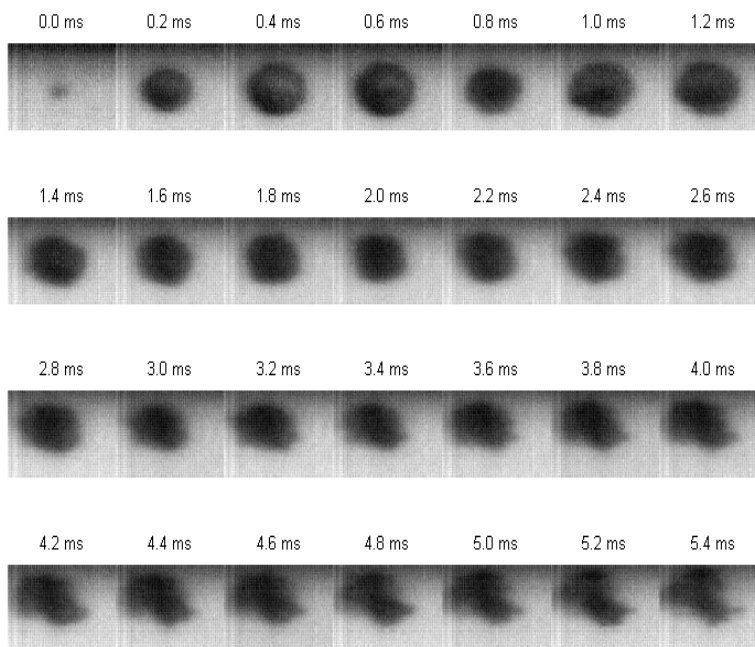
Figure 2: Individual bubble cluster (C_3H_6O, 4 ^oC, ~+/- 17 bars, 16.7 kPa)
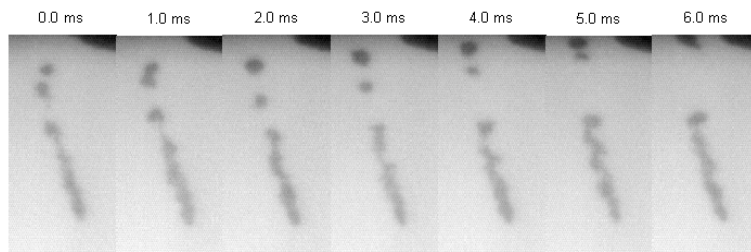
Figure 3: Comet-like streamers (C_3H_6O, 4 °C, ~+/- 17 bars, 16.0 kPa)

3.2 Signals from Microphone and PMT

Shock waves and light emissions from the imploding bubbles were detected by the attached microphone and the PMT respectively. Their signals were displayed and stored by a 100-MHz Agilent™ digital storage oscilloscope. Figure 4 depicts the typical results of these two signals under conditions involving individual clusters. Due to the propagation time required for the sound wave from the location of bubble collapse to the location of the attached microphone on the glass surface, there is a time delay between the microphone signal and the SL signal which is found to be about 30 μs for this chamber. This value corresponds nicely to the time required for a sound wave to travel from the center of the chamber to the walls of the chamber where the microphone is attached. On the other hand, Figure 5 indicates that the corresponding signals are much smaller and random for streamers.

The peak-to-peak amplitudes of the microphone signals were recorded under different driving amplitudes to the PZT ring. The results were depicted in Figure 6. These values indicate the intensities of shock waves generated by the bubble collapse. It can be seen that the shock wave intensity increases with the low acoustic driving amplitudes (implying enhanced levels of implosion) and becomes saturated with increasingly higher drive amplitude. This observation implies that the most intense implosion during cavitation does not necessarily correspond to the highest acoustic driving amplitude.

It was also observed that not every shock wave corresponds to a recorded light pulse. This was found to be especially true for conditions leading to the formation of streamers (which as mentioned earlier look like comets, and consist of thousands of tiny bubbles unlike bubbles in spherical clusters). It was distinctly noted that the presence of streamers did not produce detectable light emission at all, clearly indicating that the intensity of collapse is quite different and much lower (i.e., contents of imploding bubbles were not even hot enough to emit SL light flashes) than that from individual bubble clusters.
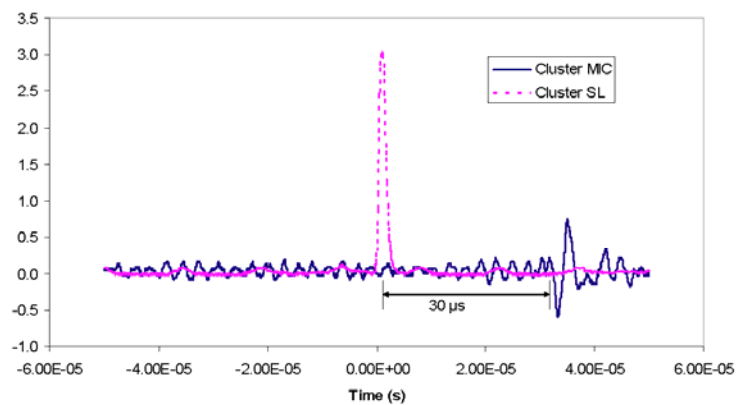
Figure 4: Signals from microphone and PMT of individual cluster
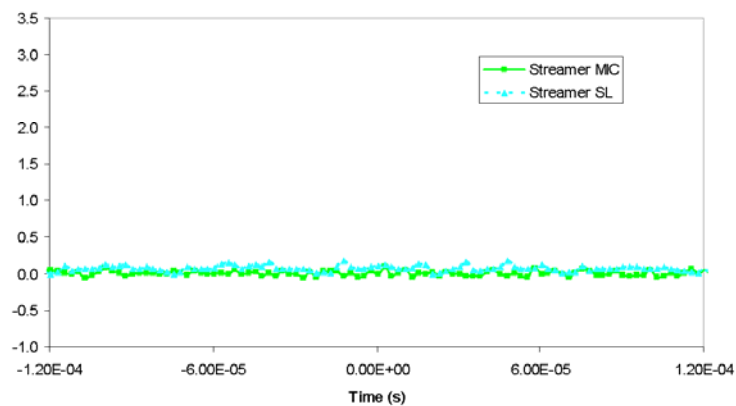
Figure 5: Signals from microphone and PMT of streamers
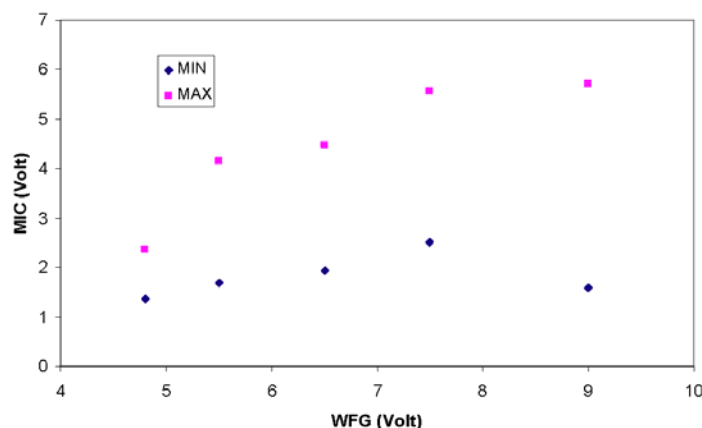
Figure 6: Amplitudes of microphone signals

4.   RESULTS OF TRITIUM EMISSION

Similar to the protocol followed for reported bubble fusion experiments (Taleyarkhan et al, 2002, 2004) tests were systematically conducted with deuterated and non-deuterated acetone over six hours duration (to accumulate significant quantities of tritium in the test fluid). The test chamber was positioned in a closed freezer with temperature control, and bubble nucleation was seeded by using a Plutonium-Beryllium (Pu-Be) isotope source (of 1 Ci activity). For each test run lasting for 6h, two samples were systematically prepared by extracting 1 ml of test fluid from the same test chamber before and after each cavitation run and mixing with 15 ml of Ultima Gold^{TM} scintillation cocktail in a 20-ml scintillation vial; therefore, four samples were available for each test run. These samples were analyzed in a scintillation counter for excess tritium emission. The Beckman LS6500^{TM} counter, a sophisticated state-of-the-art system similar to what was used by Taleyarkhan (Taleyarkhan, et al., 2002) was used for these studies. The counter was calibrated with NIST-certified quenched standards and the mass quench effect of acetone was investigated. Each sample was counted over 10 cycles and for 10 minutes during each cycle; therefore, each sample was counted for a total of 100 minutes. There was no interruption for each counting scheme and a sample with 15 ml Ultima Gold^{TM} cocktail alone was also counted simultaneously for validating and ensuring machine stability and for ensuring absence of any unusual background variations.

4.1 Calibration of the Beckman Counter

The Beckman scintillation counter (LS6500) does not directly provide the true measure of radioactive decay in the form of DPM (disintegration per minute). Instead, it conducts a calibration for quenching for each sample (during each cycle) and offers a so-called quench number "H#" along with the raw data for count-rate per minute, i.e., CPM (count per minute) values for each batch. This essentially requires the user to conduct a calibration using known standards (certified by NIST) to obtain the conversion factor from CPM to DPM.

The counter was calibrated with NIST-certified quenched tritium standard vials (procured from PerkinElmer^{TM}, 2003). The calibration data were systematically obtained in the same routine as that used for sample counting. The results are shown in Figure 7, where the H# was printed out from the counter accounting for the quenching effect and the efficiencies were calculated from the ratio of the machine CPM and the actual DPM derived from the standards (accounting for radioactive decay).

The equation shown in the figure is:

$$y = 2E\text{-}06x^3 - 0.0006x^2 - 0.162x + 59.093$$
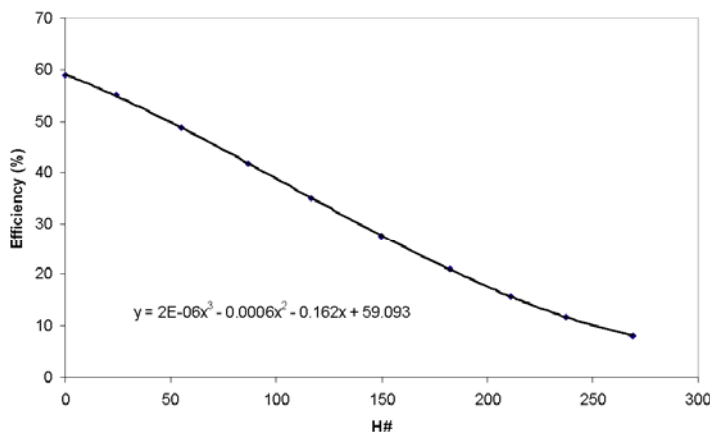
Figure 7: Beckman LS6500 scintillation counter calibration curve. The dots are calibration data points and the solid line is a curve fitting with a third-order polynomial as shown in the figure, which was used to convert the CPM into DPM in tritium counting

4.2 Tritium Counting

Several six-hour duration tests were conducted to confirm if statistically significant quantities of tritium are generated only when conducting neutron-seeded cavitation in C_3D_6O. For these experiments a 1 Ci Pu-Be neutron source (emitting about $2x10^6$ n/s) was available and therefore, utilized. The test cell (maintained at ~ 0°C temperature) was placed in a closed freezer, which was furthermore, surrounded with paraffin blocks for radiological safety. A schematic of the experimental arrangement is shown in Figure 8 along with the relative position of the Pu-Be neutron source. Tests were conducted with neutron irradiation alone, followed by tests with neutron seeded cavitation – systematically changing only one parameter at a time. Neutron-seeded acoustic cavitation was conducted for ~6 h duration. Liquid samples were taken before and after cavitation from the liquid poured into the test chamber. For each case 1 ml of acetone was pippetted and mixed with 15ml of Ultima Gold™ scintillation cocktail in a borosilicate glass vial. These vials were counted for 100 minute for each sample for tritium beta decay activity (5 to 19 keV energy emission window) in a Beckman LS6500™ liquid scintillation counter. Results of tritium activity changes are displayed in Figure 9. It is seen that a statistically significant increase (~ 4 to 6 SD) of tritium is only observed for tests with neutron-seeded cavitation of C_3D_6O. Null results are obtained for all other control experiments. For neutron-seeded cavitation tests with the control liquid C_3H_6O, as well as for tests with neutron irradiation only (without cavitation) of C_3D_6O the tritium activity changes are within 1 SD. Interestingly, one of the four 6h tests (where bubble activity was in the form of streamers, not individual large bubble clusters) with neutron-seeded cavitation of C_3D_6O also gave a null result. This appears to have been due to the occurrence of significant comet-like bubble formations during this particular test. As was mentioned earlier, the presence of streamers also does not give rise to any SL light emission. It is not clear why this particular test gave rise to streamers but the net effect of the change in thermal-hydraulic conditions is unmistakable and goes a long way towards underscoring the importance of attaining appropriate bubble cluster formations to attain bubble fusion.
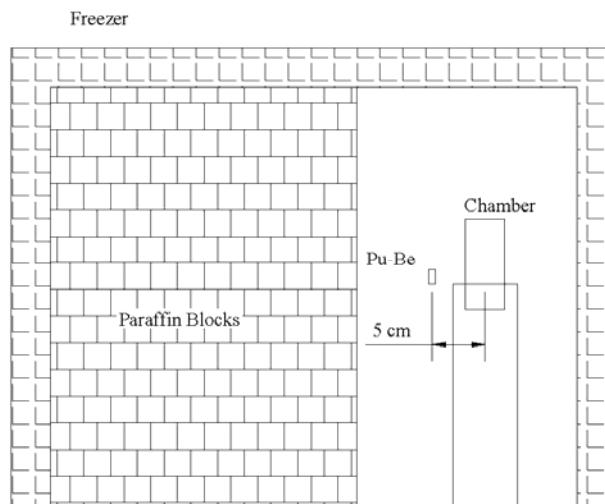
Figure 8: Schematic of experimental apparatus for tritium emission
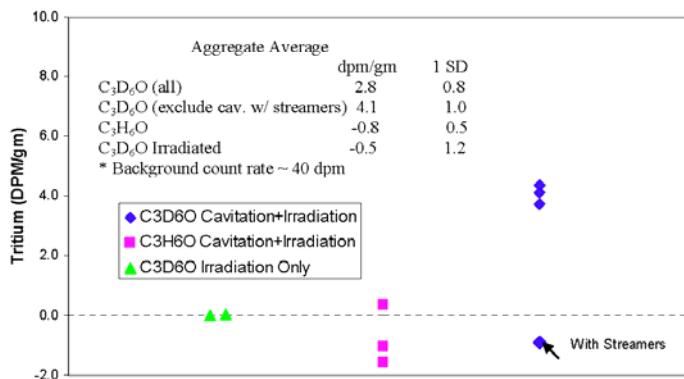
Figure 9: Results of tritium emission counting

5. DISCUSSION AND CONCLUSIONS

Bubble thermal-hydraulics was studied in relation to sonoluminescence light emission and shock wave signals. It was found that strong shock waves from spherical bubble cluster implosions correspond to the generation of significant sonoluminescence light emission, whereas streamer-like bubble formations produce neither distinct shock waves nor sonoluminescence light signals. The bubble cluster lifetime (typically 2 to 5 ms) was much longer than the acoustic driving cycle period ($\sim 50\,\mu s$) and a contraction was observed at ~0.8 ms, indicating the presence of complex thermal-hydraulic phenomena.

Tritium counting was conducted systematically by using a Beckman LS6500 scintillation counter for the samples obtained from the multiple 6-h bubble fusion experiments with deuterated acetone as well as for the control experiments with non-deuterated acetone. Irradiation only experiments were also performed for deuterated acetone in the presence of the neutron source, but without cavitation. Results of tritium measurements confirmed reported results (Taleyarkhan et al., 2002, 2004a) that the production of statistically significant emissions of tritium occurs only during neutron-seeded acoustic cavitation of deuterated acetone. Control experiments with irradiation alone, and neutron seeded cavitation of non-deuterated (H-bearing) acetone produced null results. The results indicate the possible occurrence of thermonuclear fusion reactions in neutron-seeded acoustic cavitation with deuterated acetone.

NOMENCLATURE

C_3D_6O	Deuterated Acetone
C_3H_6O	Non-deuterated Acetone
D	Deuterium
DPM	Disintegrations per minute
^{3}He	Helium-3
MIC	Microphone
n	Neutron
p	Proton
PNG	Pulse Neutron Generator
PZT	Lead-Zirconate-Titanate
SD	Standard Deviation
SL	Sonoluminescence
T	Tritium

ACKNOWLEDGEMENTS

REFERENCES

- Brennan, C. E., 1995. *Cavitation and Bubble Dynamics*, Oxford University Press, New York.

- Camara, C., Putterman, S., and Kirilov, E, Sonoluminescence from a single bubble driven at 1 Megahertz, Physical Review Letters, vol. 92, No. 12, 124301, March 2004.

- Flanigan, D. J., Suslick, K. S., Plasma formation and temperature measurement during single-bubble cavitation, Nature, vol. 434, pp. 52-55, March 2005.

- Gross, R. A., 1984. *Fusion Energy*, John Wiley and Sons.

- Matsumoto Y., 2000. Bubble and Cloud Dynamics, in *Non-Linear Acoustics and the turn of the Century*, edited by W. Lauterborn, New York.

- Moss, W. C., Clarke, D. B., White, J. W. and Young, D. A., 1996, Sonoluminescence and the prospects for table-top microthermonuclear fusion, *Phys. Lett.* **A 211**, 69-74.

- Nigmatulin, R. I., Taleyarkhan, R.P., and Lahey,Jr. R. T., 2004. Evidence for Nuclear Emissions During Acoustic Cavitation-Revisited, *Special Issue, Journal of Power and Energy, Proc. Inst. Mech. Engrs.*, **Vol. 218**, Part A, 345-364.

- Nigmatulin, R. I., Lahey,Jr. R. T., and Taleyarkhan, R. P., 2002. *The Analysis of Bubble Implosion Dynamics*, available at www.sciencemag.org/cgi/content/full/295/5561/1868/DC1/2.

- PerkinElmer, 2003. *^{3}H Quenched standards, Date of Assay: April 18, 2003*.

- Taleyarkhan, R. P., West, C. D., Cho, J. S., Lahey, Jr., R. T., Nigmatulin, R. I. and Block, R. C., 2002. Evidence of Nuclear Emissions During Acoustic Cavitation, *Science*, **295**, 1868-1873.

- Taleyarkhan, R. P., Cho, J. S., West, C. D., Lahey, Jr., R. T., Nigmatulin R. I. and Block, R. C., 2004. Additional Evidence of Nuclear Emissions During Acoustic Cavitation, *Phys. Rev. E*, **Vol. 69**, 036109.

- Taleyarkhan, R. P., Lahey, Jr., R. T. and Nigmatulin, R. I., 2004b. Bubble Nuclear Fusion Technology – Status and Challenges, *Proc. Of Japan-US Seminar on Two-Phase Flow Dynamics*, Nagahama, Japan, **Vol. 2**, 1-32, Dec. 6-11.

- Wu, C. C., and Roberts, P. H., 1993. Shock-wave propagation in a sonoluminescing gas bubble, *Phys. Rev. Lett.* **70**, 3424–3427.

ELSEVIER

Confirmatory experiments for nuclear emissions during acoustic cavitation

Yiban Xu [a,*], Adam Butt [a,b]

[a] *School of Nuclear Engineering, Purdue University, West Lafayette, IN 47907 USA*
[b] *School of Aeronautical and Astronautical Engineering, Purdue University, West Lafayette, IN 47907 USA*

Abstract

Confirmatory experiments were conducted to assess the potential for nuclear fusion related emissions of neutrons and tritium during neutron-seeded acoustic cavitation of deuterated acetone. Corresponding control experiments were conducted with normal acetone. Statistically significant (5–11 S.D. increased) emissions of 2.45 MeV neutrons and tritium were measured during cavitation experiments with chilled deuterated acetone. Control experiments with normal acetone and irradiation alone did not result in tritium activity or neutron emissions. Insights from imaging studies of bubble clusters and shock trace signals relating to bubble nuclear fusion are discussed.
Published by Elsevier B.V.

1. Introduction

It is well-known (Gross, 1984) that the thermonuclear fusion of deuterium (D) atoms requires high pressures, high temperatures and sufficient length of confinement time. The intense implosive collapse of bubbles, including acoustic cavitation bubbles, can lead to extremely high compressions and temperatures, and

to the generation of light flashes attributed to sonoluminescence and involves energy focusing of $\sim 10^{11}$ (Crum and Matula, 1997; Camara et al., 2004). The possibility of using the phenomenon of sonoluminescence for attaining thermonuclear fusion in collapsing gas–vapor cavities has been predicted theoretically as a possibility if appropriate techniques and methodologies were discovered and developed to lead to intense-enough compressions and heating (Moss et al., 1996; Nigmatulin et al., 2004; Taleyarkhan et al., 2004b). Taleyarkhan et al. (2002, 2004a) provided experimental evidence of such nuclear emissions using the novel experimental technique and approaches they developed. In this methodology, neutrons are used (much like in a conventional fission reactor where neutrons inter-

---

act with uranium nuclei and produce more neutrons) to seed nanometer size vapor bubbles in a tensioned organic liquid (acetone) which then grow by factors of ~100,000 and then intensely implode to produce flashes of sonoluminescence light accompanied with intense localized pressures, and temperatures for the compressed vapor molecules. In a deuterated liquid, the approach resulted in evidence of statistically significant neutron and tritium emissions (Taleyarkhan et al., 2002, 2004a,b).

The aim of the present study and experiments was to confirm if, by following the cited conditions and methodology by Taleyarkhan et al. (2002, 2004a) that nuclear fusion signatures (i.e., statistically significant ≤2.45 MeV neutrons and tritium emissions) can result during neutron-seeded acoustic cavitation of C_3D_6O at ~0 °C, but not with neutron irradiation alone, nor while conducting corresponding neutron-seeded acoustic cavitation experiments with C_3H_6O since thermonuclear fusion of H-atoms is not possible (Gross, 1984).

2. Experiment set-up

Following the methods and apparatus dimensions reported in the published literature (Taleyarkhan et al., 2002, 2004a), a test cell (~62 mm in diameter and ~200 mm in height) made of Pyrex™ driven with a cemented PZT piezoelectric driver ring was constructed. The system was driven with a 40 W PiezoSystems™ linear amplifier and a Agilent™ wave-form generator as shown schematically in Fig. 1. Experiments were conducted to assess if neutrons and/or tritium emissions occur when conducting neutron-seeded acoustic cavitation experiments with deuterated acetone (C_3D_6O, certified 99.92 at% D). Corresponding control experiments were also devised without cavitation (i.e., neutron irradiation alone) as well with neutron-seeded cavitation in normal acetone (C_3H_6O, 100% pure). The negative pressure threshold for bubble nucleation by fast neutrons in acetone is −7 to −8 bar (Hahn, 1961). A pressure map of the chamber was obtained by means of a calibrated hydrophone. The drive voltage corresponding to the onset of cavitation (defined herein as the onset of nucleation and collapse of bubbles within a 10 s observation period) in the presence of neutrons was first determined to get

a state point corresponding to ~±7 bar magnitude, and then doubled (as done by Taleyarkhan et al., 2002) to obtain the approximate drive pressure amplitudes of ±15 bar for conduct of the confirmatory experiments.

Unlike the experiments conducted by Taleyarkhan et al. (2002, 2004a) where precise time-based nucleation was performed with a 14 MeV pulse neutron generator (PNG), such apparatus was not available for the present study. Due to this unavailability seeding of bubbles was conducted using an available isotope neutron source. This is considered reasonable since the present study was not focused on timing of sonoluminescence flashes and time-correlation of emitted neutrons with sonoluminescence, etc., but to investigate if the key nuclear fusion signatures (2.45 MeV neutrons and tritium) are possible to detect in statistically significant quantities with neutron-seeded cavitation of C_3H_6O. The acoustic driving system, filtration (with 1 μm filters), degassing and system pressure (~10 kPa) were kept similar to that used in the Taleyarkhan et al. (2002, 2004a) experiments. Upon test cell construction, liquid degassing and performance characterization it was confirmed via counting microphone shock trace histories that ~10–20 bubble clusters could be generated per second with a drive amplitude of ~±15 bar and a resonance frequency of ~19.6 kHz for C_3D_6O and about 20.6 kHz for C_3H_6O. Although the bubble cluster activity was not as high as reported (Taleyarkhan et al., 2002, 2004a), this performance was considered adequate for overall confirmatory purposes.

As is well-known, the fusion of D atoms (Gross, 1984) results in the emission of a proton, helium-3, a neutron (of 2.45 MeV energy) and tritium. Protons (in the MeV range) are charged particles which cannot traverse more than ~1 mm in the liquid before getting absorbed, and therefore, cannot be measured with detectors outside of the apparatus. The same problem holds true for helium-3 atoms which are non-radioactive and difficult to detect in small quantities. Neutrons are uncharged particles which can leak out of the test chamber and can be detected with suitable instrumentation. Also, tritium being a radioactive gas which remains in the test liquid can be counted for beta-decay activity (if a suitable state-of-the-art beta spectrometer is available). Therefore, testing was initiated systematically for monitoring the key signatures consisting of tritium and neutron emissions.
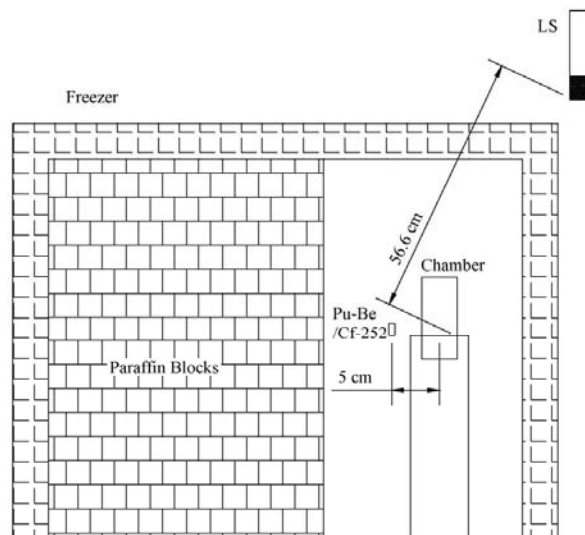
(a)   Layout of experimental apparatus
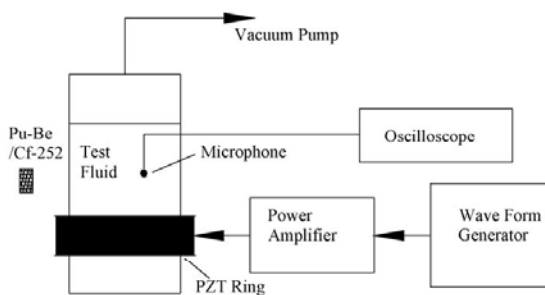
(b)   Test cell and acoustic drive chain

Fig. 1. Schematic of experimental apparatus.

3. Tritium detection experiments

Tests were first conducted to confirm if statistically significant quantities of tritium are generated only when conducting neutron-seeded cavitation in C_3D_6O. For these experiments a 1 Ci Pu–Be neutron source (emitting about 2×10^6 n/s) was available and therefore, utilized. The test cell (maintained at $\sim 0\,^\circ$C temperature) was placed in a closed freezer, which was furthermore, surrounded with paraffin blocks for radiological safety. A schematic of the experimental arrangement is shown in Fig. 1 along with the relative position of the Pu–Be neutron source. Tests were conducted with neutron irradiation alone, followed with tests

with neutron-seeded cavitation–systematically changing only one parameter at a time. Neutron-seeded acoustic cavitation was conducted for ∼6 h duration. Liquid samples were taken before and after cavitation from the liquid poured into the same test chamber. For each sample 1 cm³ of acetone was pippetted and mixed with 15 cm³ of Ultima Gold™ scintillation cocktail in a borosilicate glass vial. Each vial was counted for 100 min for tritium beta decay activity (i.e., in the 5–19 keV energy emission window) in a calibrated Beckman LS6500™ liquid scintillation counter. Results of tritium activity changes are displayed in Fig. 2. As the legend indicates, tritium data for neutron-seeded cavitation tests for 6 h with C_3D_6O are displayed using solid diamond symbols, whereas solid triangles represent data obtained with 6 h neutron irradiation (without cavitation) for C_3D_6O. Data obtained for the 6 h control tests with neutron-seeded cavitation of C_3H_6O are displayed with solid square symbols. It is seen that a statistically significant increase (∼4–5S.D.) of tritium is only observed for tests with neutron-seeded cavitation of C_3D_6O. For neutron-seeded cavitation tests with the control liquid C_3H_6O, as well as for tests with neutron irradiation of C_3D_6O the tritium activity changes are within 1S.D. One of the four 6 h tests with neutron-seeded cavitation of C_3D_6O resulted in no increase of tritium activity. This appears to have been due to the occurrence of significant and persistent (>30 ms) comet-like (see discussion in a later section) bubble streams composed of tiny (≪1 mm)

bubble clouds during this particular test alone and not the intensely imploding short-lived (<5 ms) individual and large (∼6 mm) spherical bubble clusters required for high-temperature and compression states as was the case for the other remaining three tests. Notably, for the other three remaining 6 h tests with C_3D_6O large bubble cluster implosions were present not comet-like bubble streams. Therefore, it appears that small-dimension collapsing cavitation bubbles in a comet-like configuration are not conducive for generating intense-enough nuclear fusion conditions and is in line with proposed theory (Nigmatulin et al., 2004).

4. Neutron emission measurements

Upon acquisition of neutron detection equipment tests were also initiated for monitoring changes in neutron activity with and without cavitation using the same closed freezer compartment and acoustic drive train. However, a short while after completing the experiments for tritium monitoring the experiment location had to be shifted to a new building off-campus where the 1 Ci Pu–Be isotope neutron source could not be relocated. Instead, a 0.5 mCi Cf-252 isotope neutron source was available for use. Also, a new test cell (which could produce a relatively lower approximately <10 bubble clusters per second) had to be constructed due to mechanical breakage that developed in the first test cell. A liquid scintillation
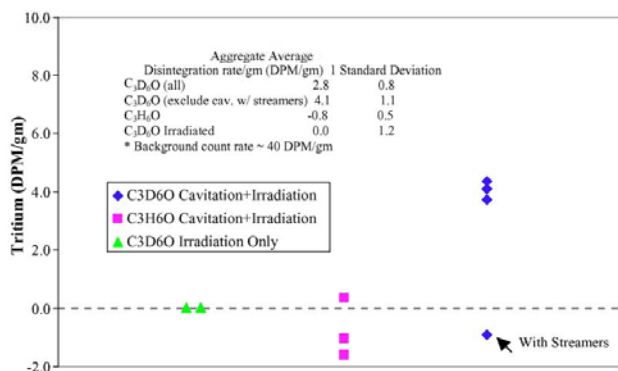
Fig. 2. Results of tritium counting.
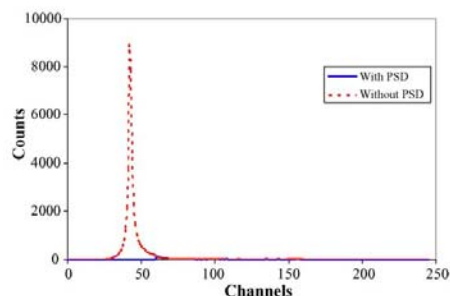
Fig. 3. Pulse shape discrimination (PSD) for gating out gamma ray emissions (using mono-energetic Co-60 source).

(LS) detector from Eljen Technologies Inc. (NE-213 type liquid-based, 5 cm × 5 cm) was procured and used for neutron detection with data acquisition electronics as reported earlier (Taleyarkhan et al., 2004a). Standard pulse shape discrimination (PSD) techniques (Harvey and Hill, 1979) were utilized using an Ortec-552 pulse shape analyzer to gate out gamma rays, as shown in Fig. 3 (where it is seen that the gamma rays component can be convincingly discriminated). For evaluating the proton recoil edge corresponding to 2.45 MeV neutron energy during pulse-height data acquisition calibration was conducted using Co-60 and Cs-137 monoenergetic gamma sources. The

respective pulse height spectra are shown in Fig. 4 from which the 2.45 MeV proton recoil edge was estimated (Harvey and Hill, 1979) to lie around channel 85. The neutron pulses from the LS detector were recorded by a UCS-20^{TM} multichannel analyzer (from Spectrum Techniques Inc.). Typical raw pulse-height data (for total counts collected in individual channels) are depicted in Fig. 5 for C_3H_6O and C_3D_6O, respectively, with and without cavitation in the presence of the neutron source—keeping all parameters the same between the control experiment and experiments with the deuterated liquid. Notably, it is seen from Fig. 5c that ~50% excess counts (over background) increase takes place only for neutron-seeded cavitation tests with C_3D_6O; this mainly occurs at and below channel 85, implying that the neutrons being emitted during cavitation are ≤2.45 MeV. The variation of counts difference between cavitation on and off for the control liquid C_3H_6O was found to be random in nature around the zero line. In relation to Fig. 5c for over 25 s of collection time, 2391 counts, and 1629 counts were collected with and without cavitation, respectively, using C_3D_6O as the test fluid in the presence of a 0.5 mCi Cf-252 source at the same position. Assuming Poisson statistics, 1 S.D. of counts $= (2391 + 1629)^{1/2} = \sim 63$. Therefore, the change in counts of about 762 (=2391 − 1629) amounts to a statistically significant increase of ~11 S.D. (= 762/63).
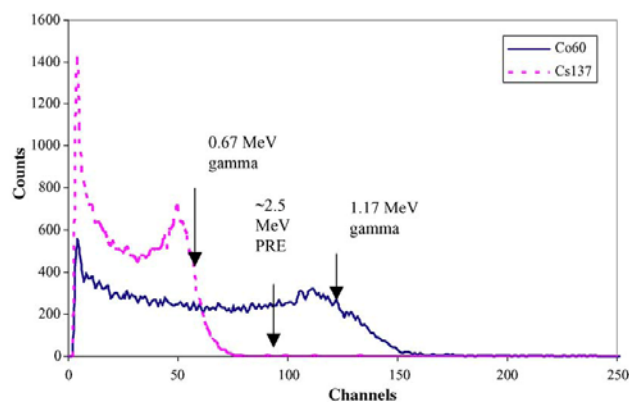
Fig. 4. Calibration of liquid scintillation detector to determine the 2.5 MeV proton recoil edge.

Y. Xu, A. Butt / Nuclear Engineering and Design 235 (2005) 1317–1324
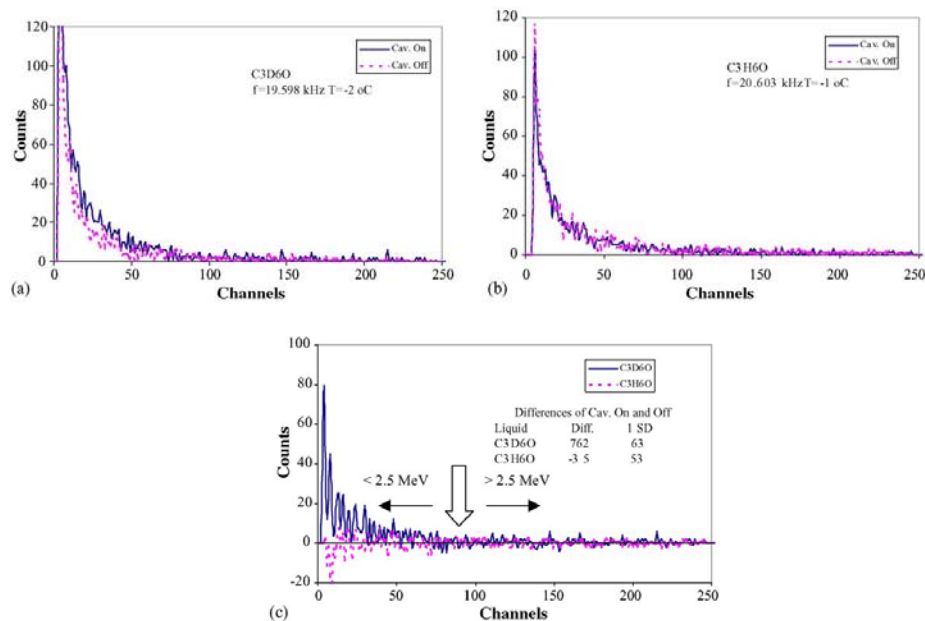
Fig. 5. (a) Representative neutron gated counts below and above 2.5 MeV proton recoil edge for tests with C_3D_6O at $\sim 0\,^{\circ}\text{C}$ with and without cavitation; (b) representative neutron gated counts below and above 2.5 MeV proton recoil edge for tests with C_3H_6O at $\sim 0\,^{\circ}\text{C}$ with and without cavitation; (c) representative neutron gated counts below and above 2.5 MeV proton recoil edge for tests with C_3D_6O and C_3H_6O at $\sim 0\,^{\circ}\text{C}$ with and without cavitation.

5. Insights into bubble dynamics behavior and possible influence on bubble fusion

During system characterization testing imaging of bubble formation and evolution was also conducted. In addition, a microphone was attached to the test cell walls to record the amplitude of shock waves generated during implosion of the bubbles (which in effect send acoustic perturbations in the liquid and can be picked up when they reach the glass walls of the test chamber). It has been postulated (Brennan, 1995) that large bubbles in the 1 mm range can break apart into clusters of tiny bubbles if the implosive collapse is violent-enough. Clearly, bubble cluster shape and form can change in a complex manner if the drive amplitude or if the pressure amplitude of the test chamber changes. It has been reported (Nigmatulin et al., 2004; Taleyarkhan et al., 2004b) that spherical bubble collapse can lead to sig-

nificantly more intensified implosions than other configurations involving aspherical collapses of bubbles. Therefore, scoping efforts were made to image the evolution of bubble clusters (using a 5000 fps camera) and relate the behavior with shock trace magnitudes to develop possible insights into the complexities involved. It was found that under nominal operating conditions (at ± 15 bar drive amplitude and test liquid at $\sim 0\,^{\circ}\text{C}$) the bubble cluster formation is largely spherical and lasts for about 5 ms. The higher the test liquid temperature, the longer is the life time for the bubbles before they re-dissolve into the bulk liquid (Taleyarkhan et al., 2004b). Fig. 6 shows a typical evolution of bubble clusters under nominal operating conditions for normal acetone (for which the temperature was $\sim 4\,^{\circ}\text{C}$). It is seen that the bubble cluster shape is largely spherical for up to about 3.6 ms, after which the bubble cluster starts to lose its spherical shape and tends to dis-
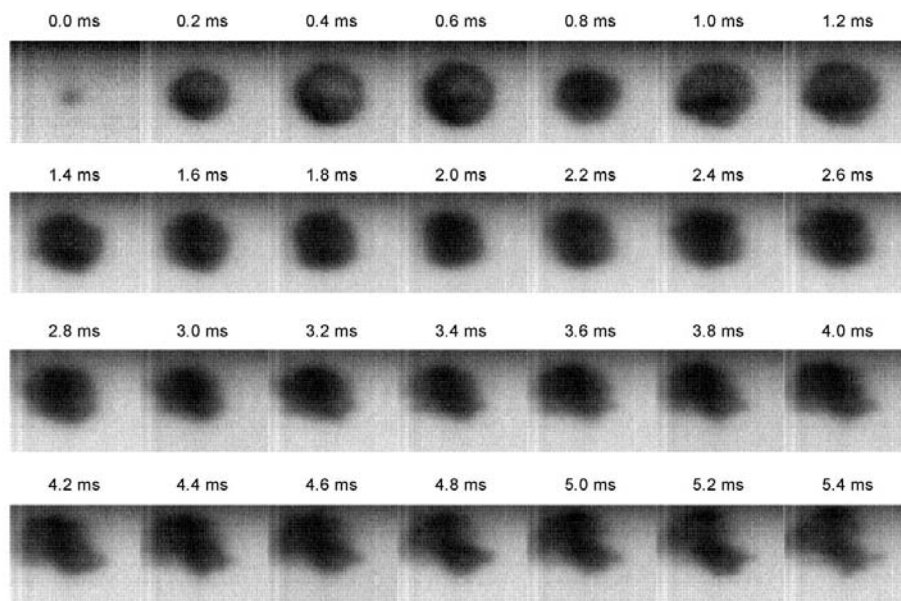
Fig. 6. Individual bubble cluster (C_3H_6O, 4 °C, ~±17 bars, 16.7 kPa).

perse and condenses back into the liquid. On the other hand, experience also indicated that under certain operating conditions the formation of imploding spherical bubble clusters can change radically to form streamers (comet-like structures) shown in Fig. 7. Such comet-like structures can last for several tens of milliseconds and appear to play a critical role in terms of their ability to induce bubble nuclear fusion.

The transition from spherical bubble cluster shape to the formation of comet-like structures was accompanied with stark changes in the recorded intensity of the shock waves (recorded by the glass-wall mounted
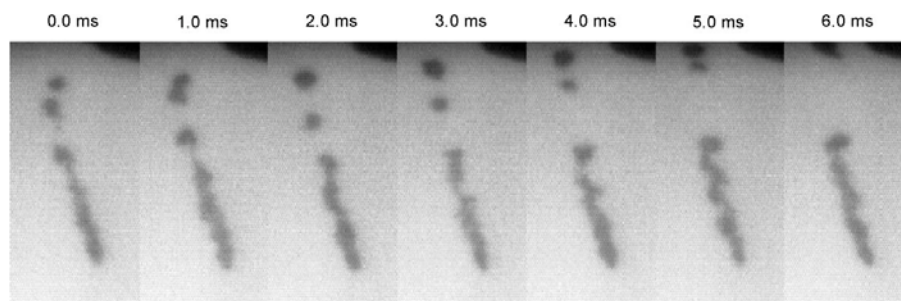
Fig. 7. Comet-like streamers (C_3H_6O, 4 °C, ~±17 bars, 16.0 kPa).
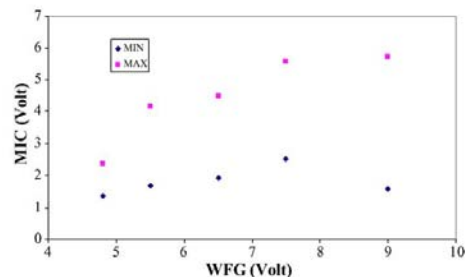
Fig. 8. Amplitudes of microphone signals with increase in drive amplitude.

microphone)—an indirect indication of implosion intensity. Fig. 8 depicts the behavior of mechanical impact-induced shock trace amplitude recorded by the microphone attached to the glass walls of the test chamber. As clearly noted, increasing the drive power from the amplifier initially increases the recorded shock trace magnitude. However, the process is non-linear. Beyond a certain power level the magnitude of shock waves levels off, and indeed, if the bubble clusters turned to comet-like structures no shock traces were recorded and the amplitude of the microphone signals dropped precipitously. These observations provide engineering insights into the tritium emission data from neutron-seeded acoustic cavitation with C_3D_6O wherein the presence of streamers also resulted in a null-result. However, this conclusion can only be considered as preliminary and more work is clearly needed to understand all the complexities of bubble cluster formation and evolution.

6. Conclusions

Statistically significant emissions of tritium and neutrons were measured during neutron-seeded acoustic cavitation experiments with chilled deuterated acetone. Excess neutrons were found to be ≤ 2.45 MeV in energy. Control experiments with normal acetone and experiments with neutron irradiation alone did not re-sult in statistically significant neutron nor tritium emissions.

References

Brennan, C.E., 1995. Cavitation & Bubble Dynamics. Oxford University Press, New York.

Camara, C., Putterman, S., Kirilov, E., 2004. Sonoluminescence from a Single Bubble Driven at 1 MHz, vol. 92. PRL, p. 12.

Crum, L., Matula, T., 1997. Shocking revelations. Science 276, 1348.

Gross, R.A., 1984. Fusion Energy. John Wiley and Sons.

Hahn, B., 1961. Nuovo Cimento, 22, pp. 650.

Harvey, J., Hill, N., 1979. Nucl. Instrm. Methods 162, 507.

Moss, W.C., Clarke, D.B., White, J.W., Young, D.A., 1996. Sonoluminescence and the prospects for table-top microthermonuclear fusion. Phys. Lett. A 211, 69–74.

Nigmatulin, R.I., Taleyarkhan, R.P., Lahey Jr., R.T., 2004. Evidence for nuclear emissions during acoustic cavitation—revisited. Proc. Inst. Mech. Eng.. Journal of Power and Energy, Part A 218, 345–364, Special Issue.

Taleyarkhan, R.P., West, C.D., Cho, J.S., Lahey Jr., R.T., Nigmatulin, R.I., Block, R.C., 2002. Evidence of nuclear emissions during acoustic cavitation. Science 295, 1868–1873.

Taleyarkhan, R.P., Cho, J.S., West, C.D., Lahey Jr., R.T., Nigmatulin, R.I., Block, R.C., 2004a. Additional evidence of nuclear emissions during acoustic cavitation. Phys. Rev. E 69, 036109.

Taleyarkhan, R.P., Lahey Jr., R.T., Nigmatulin, R.I., 2004b. Bubble Nuclear Fusion Technology—Status and Challenges. In: Proceeding of Japan-US Seminar on Two-Phase Flow Dynamics, vol. 2, Nagahama, Japan, December 6–11, pp. 1–32.

Appendix D

FEMLAB™ Final Chamber Model Report

File name: ChamberFinal.fl

Application modes and modules used in this model:

- Geom1 (Axial symmetry (2D))
  - Axial Symmetry, Stress-Strain (Structural Mechanics Module)
  - Incompressible Navier-Stokes
  - Acoustics

1. Model Properties

Property	Value
Model name	
Author	
Company	
Department	
Reference	
Saved date	Dec 1, 2005 1:46:38 AM
Creation date	Jul 25, 2005 11:13:29 AM
FEMLAB version	FEMLAB 3.1.0.163

2. Geometry

Number of geometries: 1

2.1. Geom1
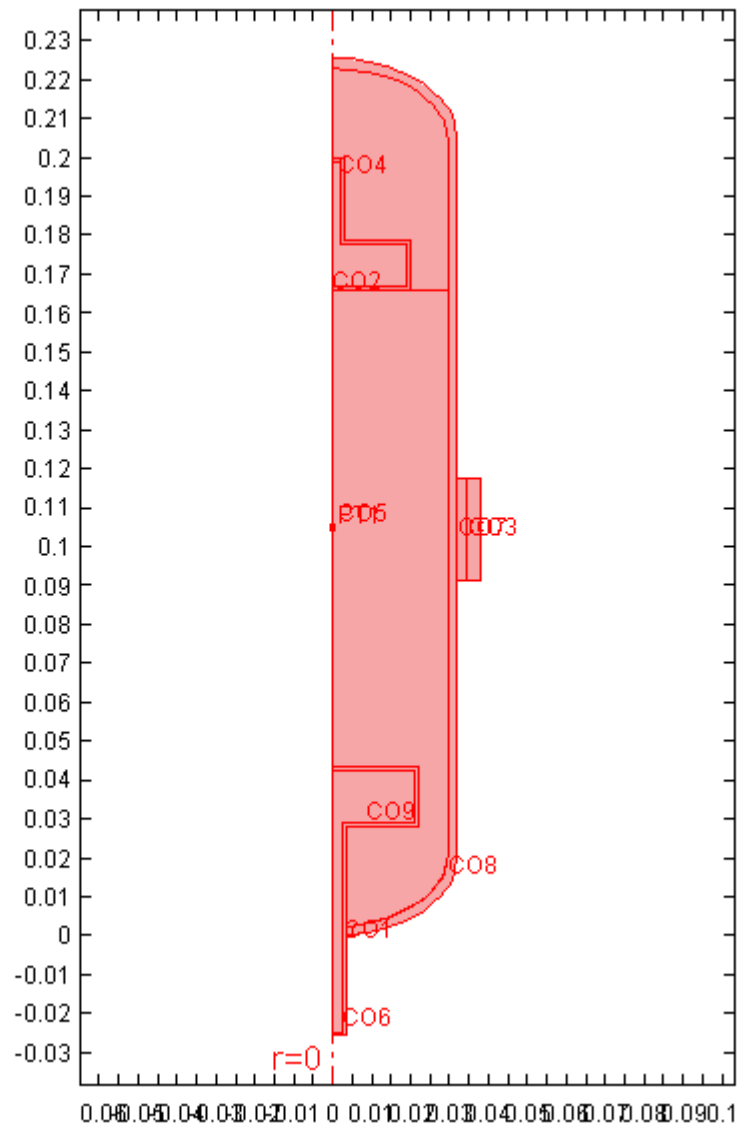
2.1.1. Point Mode
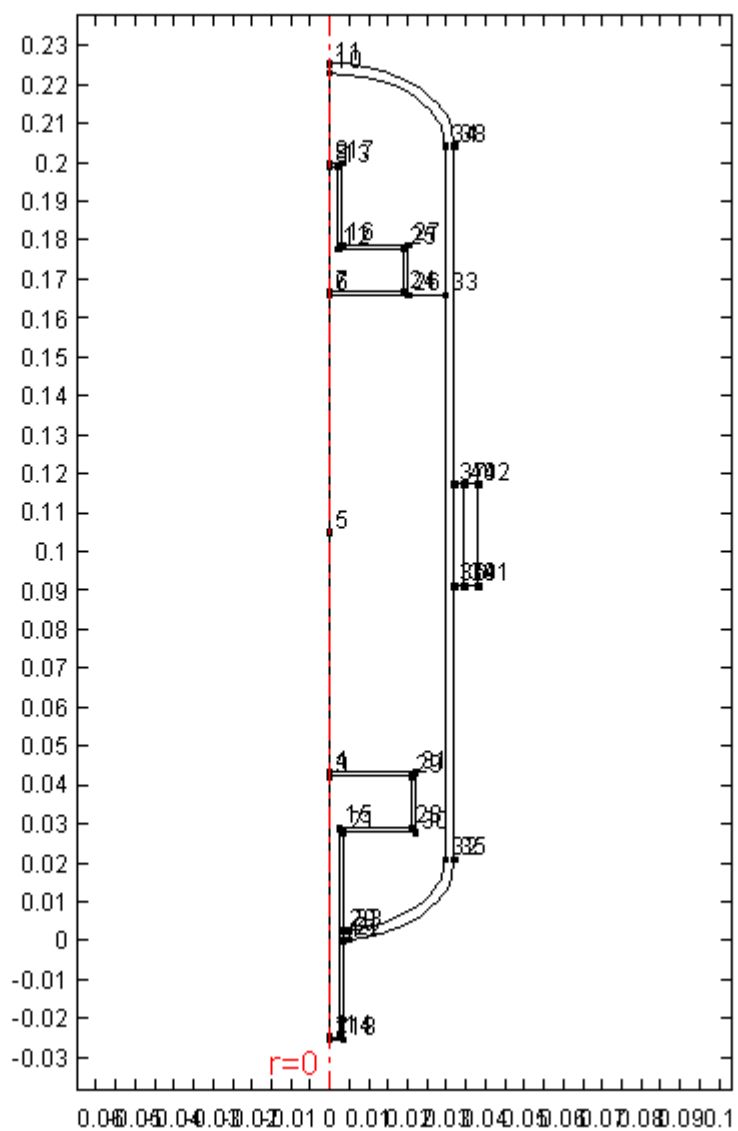
2.1.2. Boundary Mode
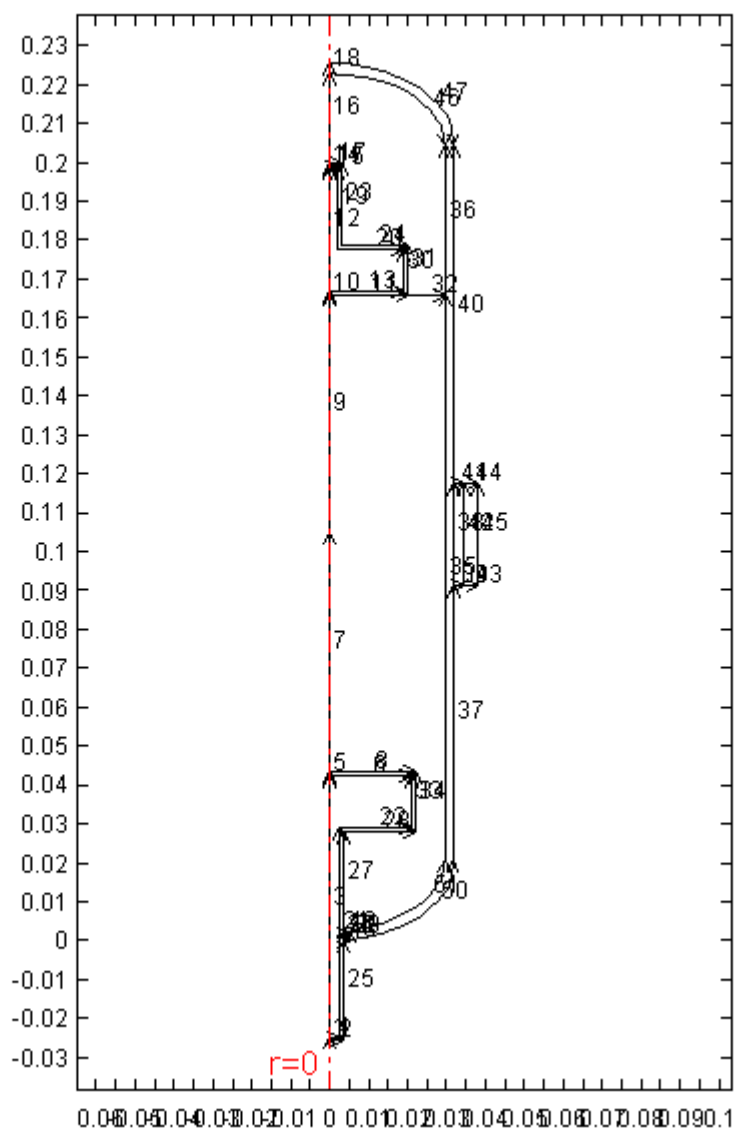
2.1.3. Subdomain Mode
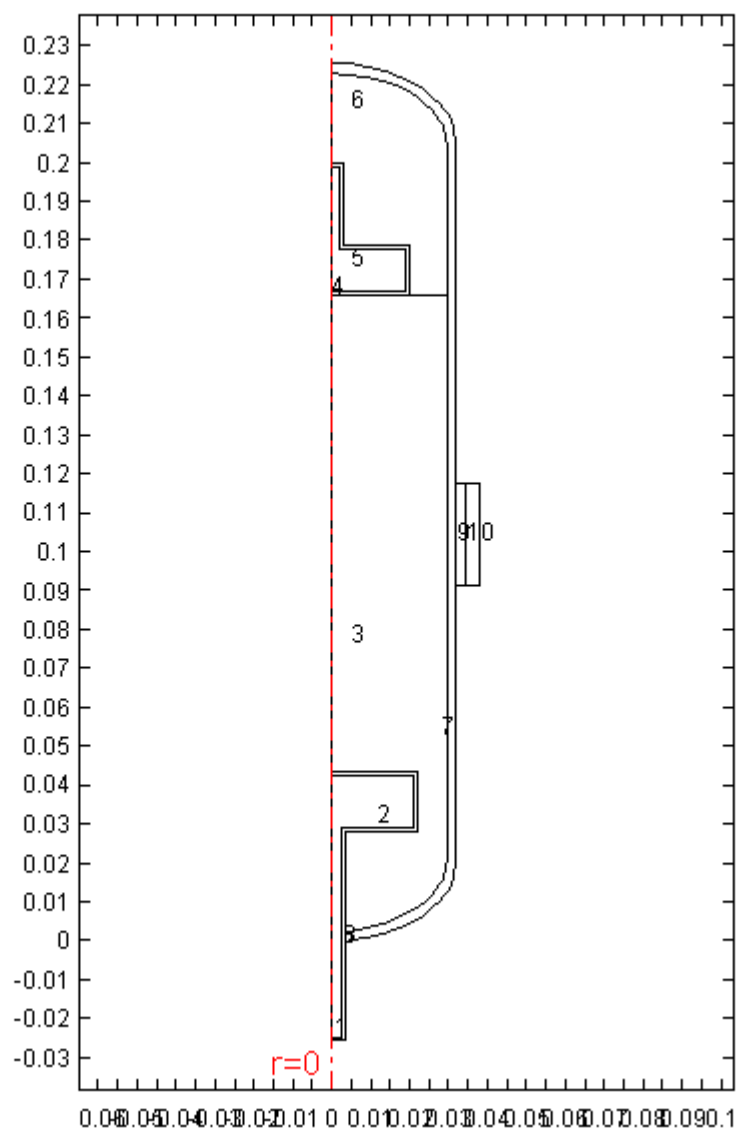
3. Geom1

Space dimensions: Axial symmetry (2D)

3.1. Scalar Expressions

Name Expression

Force $0.5*(0.1174*(frq/1000)^4 - 10.135*(frq/1000)^3 + 324*(frq/1000)^2 - 4545.4*(frq/1000) + 23640)$

3.2. Expressions

3.2.1. Boundary Expressions

Boundary	4, 13, 19, 21-22, 30, 33	5	6, 15, 20	8, 35-36, 49, 51	11, 23, 31	17, 24	27-28, 34, 46
Nr	-nr		nr	-nr	nr	-nr	nr
Nz	-nz		nz	-nz	nz	-nz	nz
acc_normal	uaxi_tt_axi*Nr+w_tt_axi*Nz	uaxi_tt_axi*Nr+w_tt_axi*Nz	uaxi_tt_axi*Nr+w_tt_axi*Nz	uaxi_tt_axi*Nr+w_tt_axi*Nz	uaxi_tt_axi*Nr+w_tt_axi*Nz	uaxi_tt_axi*Nr+w_tt_axi*Nz	uaxi_tt_axi*Nr+w_tt_axi*Nz

3.3. Mesh

3.3.1. Extended mesh

Number of degrees of freedom 19482

3.3.2. Base mesh

Number of boundary elements 536
Number of elements   2889
Minimum element quality   0.5500
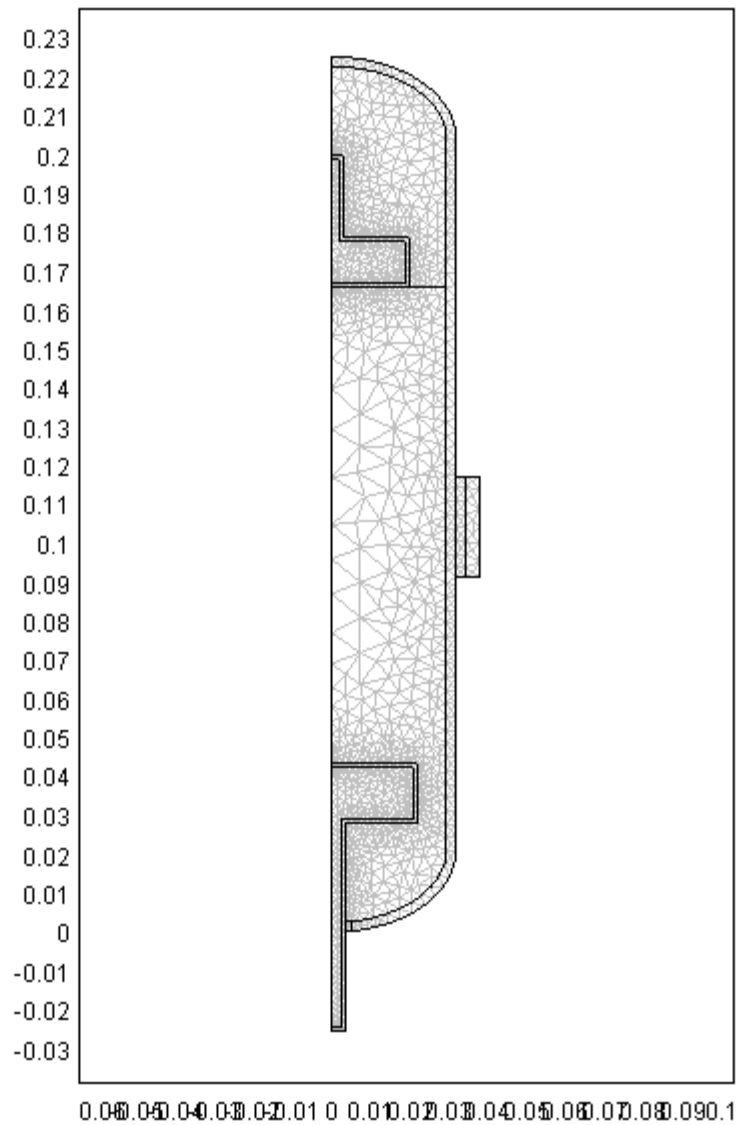
3.4. Application Mode: Axial Symmetry, Stress-Strain

Application mode type: Axial Symmetry, Stress-Strain (Structural Mechanics Module)

Application mode name: axi

3.4.1. Scalar Variables.

Name Variable Value Description
freq   freq_axi frq   Excitation frequency

3.4.2. Application Mode Properties

Property	Value
Default element type	Lagrange - Quadratic
Analysis type	Frequency response
Large deformation	off
Implementation	Principle of virtual work
Specify eigenvalues using	Eigenfrequency
Weak constraints	Off

3.4.3. Variables

Dependent variables: uor, w, uor_t, w_t

Independent variables: r, phi, z

Shape functions: shlag(2,'uor'), shlag(2,'w')

Interior boundaries not active

3.4.4. Point Settings

Point	1-42
Point load (force) r-dir. (Fr)	0
Amp. factor point load r-dir. (FrAmp)	1
Phase angle point load r-dir. (FrPh)	0
Point load (force) z-dir. (Fz)	0
Amp. factor point load z-dir. (FzAmp)	1
Phase angle point load z-dir. (FzPh)	0
loadcoord	'global'
constrcoord	'global'
constrtype	'standard'
H Matrix (H)	{0,0;0,0}
R Vector (R)	{0;0}

Constraint r-dir. (Rr)	0
Hr	0
Constraint z-dir. (Rz)	0
Hz	0
weakconstr	1
Shape functions (wcshape)	[]
Initial value (wcinit)	{0;0;0;0}

3.4.5. Boundary Settings

Locked Boundaries: 4, 6, 13, 15, 19-22, 30, 33

Boundary	1-2, 5, 10, 14, 18, 25, 37, 39-41, 43-45, 47-48, 50	4, 6, 8, 11, 13, 15, 17, 19-24, 27-28, 30-31, 33-36, 46, 49, 51
Edge load (force/area) r-dir. (Fr)	0	**-p*Nr**
Amp. factor edge load r-dir. (FrAmp)	1	1
Phase angle edge load r-dir. (FrPh)	0	0
Edge load (force/area) z-dir. (Fz)	0	**-p*Nz**
Amp. factor edge load z-dir. (FzAmp)	1	1
Phase angle edge load z-dir. (FzPh)	0	0
loadcoord	global	global
constrcoord	global	global
constrtype	standard	standard
H Matrix (H)	{0,0;0,0}	{0,0;0,0}
R Vector (R)	{0;0}	{0;0}
Constraint r-dir. (Rr)	0	0
Hr	0	0
Constraint z-dir. (Rz)	0	0
Hz	0	0
weakconstr	1	1
Shape functions (wcshape)	[]	[]

Integration order (wcgporder)	2		2	
Initial value (wcinit)	{0;0;0;0}		{0;0;0;0}	

3.4.6. Subdomain Settings

Subdomain	1, 4, 7	8	9
Shape functions (shape)	shlag(2,'uor') shlag(2,'w') shlag(2,'u') shlag(2,'v') shlag(1,'p') shlag(2,'p2')	shlag(2,'uor') shlag(2,'w') shlag(2,'u') shlag(2,'v') shlag(1,'p') shlag(2,'p2')	shlag(2,'uor') shlag(2,'w') shlag(2,'u') shlag(2,'v') shlag(1,'p') shlag(2,'p2')
Integration order (gporder)	4 4	4 4	4 4
Constraint order (cporder)	2 2	2 2	2 2
Young's modulus (E)	**73.1e9 (Boron Silica Glass)**	**9e7 (RTV Silicone)**	**1e9 (Epoxy)**
Density (rho)	**2230 (Boron Silica Glass)**	**1040 (RTV Silicone)**	**1215 (Epoxy)**
Mass damping parameter (alphadM)	1	1	1
Stiffness damping parameter (betadK)	**0.5e-7**	**0.5e-7**	**0.5e-7**
materialcoord	global	global	global
materialmodel	Isotropic material	Isotropic material	Isotropic material
hardeningmodel			
yieldtype			
isodata			
Kinematic tangent modulus (ETkin)			
Isotropic tangent modulus (ETiso)			
Yield stress level (Sys)			
Yield function (Syfunc)			
Yield function			

(Syfunc_kin) Hardening function (Shard)			
ini_stress	0	0	0
ini_strain	0	0	0
Initial shear stress srz (srzi)	0	0	0
Initial shear strain erz (erzi)	0	0	0
Initial normal stress sr (sri)	0	0	0
Initial normal strain er (eri)	0	0	0
Initial normal stress sphi (sphii)	0	0	0
Initial normal strain ephi (ephii)	0	0	0
Initial normal stress sz (szi)	0	0	0
Initial normal strain ez (ezi)	0	0	0
Thermal expansion coeff. (alpha)	**0.55e-6**	**0.55e-6**	**0.55e-6**
Poisson's ratio (nu)	**0.17 (Boron Silica Glass)**	**0.485 (RTV Silicone)**	**0.3 (Epoxy)**
Shear_modulus rz plane (Grz)			
Poisson's ratio rphi plane (nurphi)			
Thermal expansion coeff. r-dir. (alphar)			
Young's modulus r-dir. (Er)			
Poisson's ratio phiz plane (nuphiz)			
Thermal expansion coeff. phi-dir. (alphaphi)			
Young's modulus phi-dir. (Ephi)			

Poisson's ratio rz plane (nurz)			
Thermal expansion coeff. z-dir. (alphaz)			
Young's modulus z-dir. (Ez)			
Elasticity matrix (D)			
Thermal expansion vector (alphavector)			
Body load (force/volume) r-dir. (Fr	0	0	0
Amp. factor body load r-dir. (FrAmp)	1	1	1
Phase angle body load r-dir. (FrPh)	0	0	0
Body load (force/volume) z-dir. (Fz)	0	0	0
Amp. factor body load z-dir. (FzAmp)	1	1	1
Phase angle body load z-dir. (FzPh)	0	0	0
loadcoord	global	global	global
Tflag	0	0	0
Strain temperature (Temp)	0	0	0
Strain ref. temperature (Tempref)	0	0	0
constrcoord	global	global	global
constrtype	Standard notation	Standard notation	Standard notation
H Matrix (H)	{0,0;0,0}	{0,0;0,0}	{0,0;0,0}
R Vector (R)	{0;0}	{0;0}	{0;0}
Constraint r-dir. (Rr)	0	0	0
Hr	0	0	0
Constraint z-dir.	0	0	0

(Rz)

Hz	0	0	0
weakconstr	1	1	1

Subdomain	10
Shape functions (shape)	shlag(2,'uor') shlag(2,'w') shlag(2,'u') shlag(2,'v') shlag(1,'p') shlag(2,'p2')
Integration order (gporder)	4 4
Constraint order (cporder)	2 2
Young's modulus (E)	**6e10 (Type 5800 Piezoceramic)**
Density (rho)	**7368.5 (Type 5800 Piezoceramic)**
Mass damping parameter (alphadM)	1
Stiffness damping parameter (betadK)	**0.5e-7**
materialcoord	global
materialmodel	Isotropic material
hardeningmodel	
yieldtype	
isodata	
Kinematic tangent modulus (ETkin)	
Isotropic tangent modulus (ETiso)	
Yield stress level (Sys)	
Yield function (Syfunc)	
Yield function (Syfunc_kin)	
Hardening function (Shard)	
ini_stress	0
ini_strain	0
Initial shear stress srz (srzi)	0
Initial shear strain erz (erzi)	0
Initial normal stress sr (sri)	0
Initial normal strain er (eri)	0
Initial normal stress sphi (sphii)	0
Initial normal strain ephi (ephii)	0
Initial normal stress sz (szi)	0
Initial normal strain ez (ezi)	0
Thermal expansion coeff.	**0.55e-6**

(alpha)	
Poisson's ratio (nu)	**0.25 (Type 5800 Piezoceramic)**
Shear_modulus rz plane (Grz)	
Poisson's ratio rphi plane (nurphi)	
Thermal expansion coeff. r-dir. (alphar)	
Young's modulus r-dir. (Er)	
Poisson's ratio phiz plane (nuphiz)	
Thermal expansion coeff. phi-dir. (alphaphi)	
Young's modulus phi-dir. (Ephi)	
Poisson's ratio rz plane (nurz)	
Thermal expansion coeff. z-dir. (alphaz)	
Young's modulus z-dir. (Ez)	
Elasticity matrix (D)	
Thermal expansion vector (alphavector)	
Body load (force/volume) r-dir. (Fr)	**2.58e7**
Amp. factor body load r-dir. (FrAmp)	1
Phase angle body load r-dir. (FrPh)	0
Body load (force/volume) z-dir. (Fz)	0
Amp. factor body load z-dir. (FzAmp)	1
Phase angle body load z-dir. (FzPh)	0
loadcoord	global
Tflag	0
Strain temperature (Temp)	0
Strain ref. temperature (Tempref)	0
constrcoord	global
constrtype	Standard notation

H Matrix (H)	{0,0;0,0}
R Vector (R)	{0;0}
Constraint r-dir. (Rr)	0
Hr	0
Constraint z-dir. (Rz)	0
Hz	0
weakconstr	1
Subdomain initial value	1, 4, 7 8 9 10
r-displacement divided by r (uor) 0	0 0 0
z-displacement (w)	0 0 0 0

3.5. Application Mode: Incompressible Navier-Stokes

Application mode type: Incompressible Navier-Stokes

Application mode name: ns

3.5.1. Application Mode Properties

Property	Value
Default element type	Lagrange - P_2 P_1
Stress tensor	Total
Weak constraints	Off

3.5.2. Variables

Dependent variables: u, v, w2, p

Independent variables: r, phi, z

Shape functions: shlag(2,'u'), shlag(2,'v'), shlag(1,'p')

Interior boundaries active

3.5.3. Point Settings

Point	1-42
Pressure (p0)	0
pnton	0

3.5.4. Boundary Settings

Locked Boundaries: 4, 6, 13, 15, 19-22, 30, 33

Boundary	3, 7, 9, 12, 16	8, 27-28, 34-36, 46, 49, 51	11, 17, 23-24, 31
Type	Axial symmetry	Normal flow/Pressure	Normal flow/Pressure
r-velocity (u0)	0	0	**uaxi_t_axi**
z-velocity (v0)	0	0	**w_t**
phi-velocity (w0)	0	0	0
Pressure (p0)	0	**-p2**	**-p2**
weakconstr	1	1	1
Shape functions (wcshape)	[]	[]	[]
wcgporder	2	2	2
wcinit	{0;0}	{0;0}	{0;0}

Boundary	4, 6, 13, 15, 19-22, 30, 33
Type	Inflow/Outflow velocity
r-velocity (u0)	**uaxi_t_axi**
z-velocity (v0)	**w_t**
phi-velocity (w0)	0
Pressure (p0)	**-p2**
weakconstr	1
Shape functions (wcshape)	[]
wcgporder	2
wcinit	{0;0}

3.5.5. Subdomain Settings

Subdomain	2, 5-6	3
Shape functions (shape)	shlag(2,'uor') shlag(2,'w') shlag(2,'u') shlag(2,'v') shlag(1,'p') shlag(2,'p2')	shlag(2,'uor') shlag(2,'w') shlag(2,'u') shlag(2,'v') shlag(1,'p') shlag(2,'p2')
Integration order (gporder)	**4 4 2**	**4 4 2**
Constraint order (cporder)	**2 2 1**	**2 2 1**
Density (rho)	**1.23**	**789**

	17e-6	0.326e-3
Dynamic viscosity (eta)	**17e-6**	**0.326e-3**
Volume force, r-dir. (F_r)	0	0
Volume force, z-dir. (F_z)	0	0
Volume force, phi-dir. (F_phi)	0	0
Isotropic diffusion switch (idon)	0	0
Tuning parameter (delid)	0.5	0.5
Streamline diffusion switch (sdon)	0	0
Streamline diffusion type (sdtype)	pgc	pgc
Tuning parameter (delsd)	0.25	0.25
Crosswind diffusion switch (cdon)	0	0
Crosswind diffusion type (cdtype)	sc	sc
Tuning parameter (delcd)	0.35	0.35
Pressure stabilization switch (pson)	0	0
Tuning parameter (delps)	1	1

Subdomain initial value	2, 5-6	3
r-velocity (u)	0	0
z-velocity (v)	0	0
Pressure (p)	0	0

3.6. Application Mode: Acoustics

Application mode type: Acoustics

Application mode name: aco

3.6.1. Scalar Variables.

Name Variable   Value Description
freq   freq_aco   frq   Frequency
p_ref   p_ref_aco 20e-6 Pressure reference

3.6.2. Application Mode Properties

Property	Value
Default element type	Lagrange - Quadratic
Analysis type	Time-harmonic
Weak constraints	Off

3.6.3. Variables

Dependent variables: p2, p2_t

Independent variables: r, phi, z

Shape functions: shlag(2,'p2')

Interior boundaries active

3.6.4. Boundary Settings

Locked Boundaries: 4, 6, 13, 15, 19-22, 30, 33

Boundary	3, 7, 9, 12, 16	4, 6, 8, 11, 13, 15, 17, 19-24, 27-28, 30-31, 33-36, 46, 49, 51
Type	Axial symmetry	Normal acceleration
Pressure source (p0)	0	0
Input impedance (Z)	1.25*343	1.25*343
Normal acceleration (nacc)	0	**-acc_normal**
Source location, # coordinate (x0)	0	0
Source location, # coordinate (y0)	0	0

Dipole source (qs0)	{0;0}	{0;0}
Wave direction (kdir)	{'-nr';'-nz'}	{'-nr';'-nz'}
wavetype	PL	PL
weakconstr	1	1
Shape functions (wcshape)	[]	[]
Integration order (wcgporder)	2	2
Initial value (wcinit)	{0;0}	{0;0}

3.6.5. Subdomain Settings

Subdomain	2, 5-6	3
Shape functions (shape)	shlag(2,'uor') shlag(2,'w') shlag(2,'u') shlag(2,'v') shlag(1,'p') shlag(2,'p2')	shlag(2,'uor') shlag(2,'w') shlag(2,'u') shlag(2,'v') shlag(1,'p') shlag(2,'p2')
Integration order (gporder)	4	4
Constraint order (cporder)	2	2
Fluid density (rho)	**1.23**	**789**
Speed of sound (cs)	343	**1170**
Dipole source (qs)	{0;0}	{0;0}

Subdomain initial value	2, 5-6	3
Pressure (p2)	0	0

4. Materials Library

4.1. Boron Silica Glass

Parameter	Value
Density (rho)	2230
Poisson's ratio (nu)	0.17
Young's modulus (E)	73.1e9

4.2. Type 5800 Piezoceramic

Parameter	Value
Density (rho)	7368.5
Poisson's ratio (nu)	0.25
Young's modulus (E)	6e10

4.3. Epoxy

Parameter	Value
Density (rho)	1215
Poisson's ratio (nu)	0.3
Young's modulus (E)	1e9

4.4. RTV Silicone

Parameter	Value
Density (rho)	1040
Poisson's ratio (nu)	0.485
Young's modulus (E)	9e7

5. Solver Settings

Solve using a script: off

Analysis	freq
Auto select solver	on
Solver	Parametric linear
Solution form	general
Symmetric	off
Adaption	off

5.1. Direct (UMFPACK)

Solver type: Linear system solver

Parameter	Value
Pivot threshold	0.1
Memory allocation factor	0.7

5.2. Parametric

Parameter	Value
Name of parameter	Frq
List of parameter values	17000:100:27000
Predictor	1
Manual tuning of parameter step size	Off
Initial step size	0.0
Minimum step size	0.0
Maximum step size	0.0

5.3. Advanced

Parameter	Value
Constraint handling method	Eliminate
Null-space function	Auto
Assembly block size	5000
Use Hermitian transpose	Off
Use complex functions with real input	Off
Type of scaling	Auto
Manual scaling	
Row equilibration	On
Manual control of reassembly	Off
Load constant	On
Constraint constant	On
Mass constant	On
Jacobian constant	On
Constraint Jacobian constant	On

6. Postprocessing

frq(8)=17700   Surface: Pressure   Max: 1.501
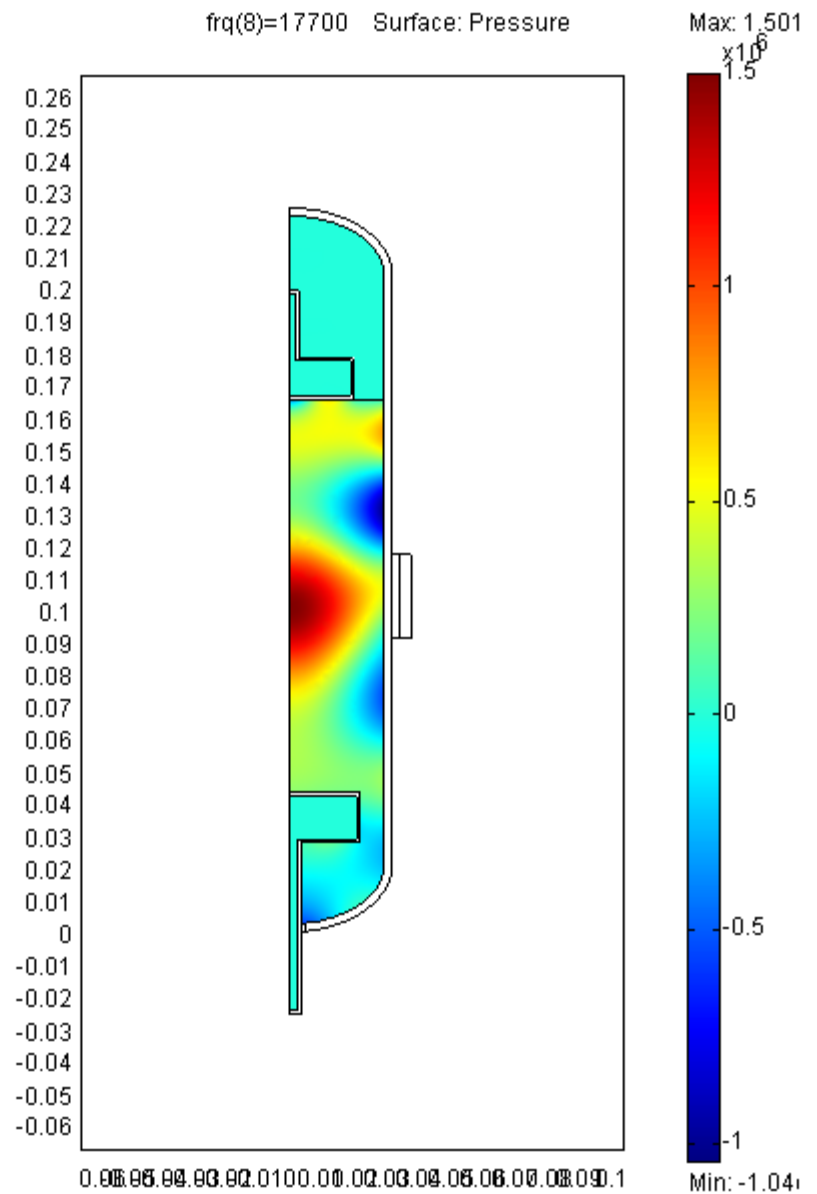
7. Equations

7.1. Point

Dependent variables: uor, w, u, v, p, p2

7.1.1. Point: 1, 11, 18-19, 22, 35-42

weak term

0

0

0

0

0

0

dweak term

0

0

0

0

0

0

constr term

0

0

0

0

0

0

7.1.2. Point: 2-4, 6-10, 12-17, 20-21, 23-34

weak term

0

0

0

0

0

0

dweak term

0

0

0

0

0

0

constr term

0

0

0

0

0

0

7.1.3. Point: 5

weak term

0

0

0

0

0

0

dweak term

0

0

0

0

0

0

constr term

0

0

0
0
0
0

7.2. Boundary

Dependent variables: uor, w, u, v, p, p2

7.2.1. Boundary: 1-2, 10, 14, 18, 25-26, 29, 37-45, 47-48, 50

q coefficient

uor	w	u	v	p	p2
0	0	0	0	0	0
0	0	0	0	0	0
0	0	0	0	0	0
0	0	0	0	0	0
0	0	0	0	0	0
0	0	0	0	0	0

g coefficient

0
0
0
0
0
0

h coefficient

uor	w	u	v	p	p2
0	0	0	0	0	0
0	0	0	0	0	0
0	0	0	0	0	0
0	0	0	0	0	0
0	0	0	0	0	0
0	0	0	0	0	0

r coefficient

0
0
0
0
0
0

weak term

0
0
0
0
0
0

dweak term

0
0
0
0
0
0

constr term

0
0
0
0
0
0

7.2.2. Boundary: 3, 7, 9, 12, 16

q coefficient

uor w u v p p2

0   0 0 0 0 0
0   0 0 0 0 0
0   0 0 0 0 0
0   0 0 0 0 0
0   0 0 0 0 0
0   0 0 0 0 0

g coefficient

0
0
0
0
0
0

h coefficient

uor	w	u	v	p	p2
0	0	0	0	0	0
0	0	0	0	0	0
-diff(-u,uor)	-diff(-u,w)	-diff(-u,u)	-diff(-u,v)	-diff(-u,p)	-diff(-u,p2)
0	0	0	0	0	0
0	0	0	0	0	0
0	0	0	0	0	0

r coefficient

0
0
-u
0
0
0

weak term

0

0
0
0
0
0

dweak term

0
0
0
0
0
0

constr term

0
0
0
0
0
0

7.2.3. Boundary: 4, 13, 19, 21-22, 30, 33 [locked]

q coefficient

uor	w	u	v	p	p2
0	0	0	0	0	0
0	0	0	0	0	0
0	0	0	0	0	0
0	0	0	0	0	0
0	0	0	0	0	0
-	-	-	-	-	-
diff(r*nacc_aco,uor)	diff(r*nacc_aco,w)	diff(r*nacc_aco,u)	diff(r*nacc_aco,v)	diff(r*nacc_aco,p)	diff(r*nacc_aco,p2)

g coefficient

0
0
0
0
0
r*nacc_aco

h coefficient

uor	w	u	v	p	p2
0	0	0	0	0	0
0	0	0	0	0	0
-diff(u0_ns-u,uor)	-diff(u0_ns-u,w)	-diff(u0_ns-u,u)	-diff(u0_ns-u,v)	-diff(u0_ns-u,p)	-diff(u0_ns-u,p2)
-diff(v0_ns-v,uor)	-diff(v0_ns-v,w)	-diff(v0_ns-v,u)	-diff(v0_ns-v,v)	-diff(v0_ns-v,p)	-diff(v0_ns-v,p2)
0	0	0	0	0	0
0	0	0	0	0	0

r coefficient

0
0
u0_ns-u
v0_ns-v
0
0

weak term

Frg_axi*uor_test*r^2
Fzg_axi*w_test*r
0
0
0
0

dweak term

w_time*p_test

0

0

0

0

0

constr term

0

0

0

0

0

0

7.2.4. Boundary: 5

q coefficient

uor w u v p p2

0   0 0 0 0 0

0   0 0 0 0 0

0   0 0 0 0 0

0   0 0 0 0 0

0   0 0 0 0 0

0   0 0 0 0 0

g coefficient

0

0

0

0

0

0

h coefficient

```
uor w u v p p2
0   0 0 0 0 0
0   0 0 0 0 0
0   0 0 0 0 0
0   0 0 0 0 0
0   0 0 0 0 0
0   0 0 0 0 0
```

r coefficient

0
0
0
0
0
0

weak term

0
0
0
0
0
0

dweak term

0
0
0
0
0
0

constr term

0
0

0
0
0
0

7.2.5. Boundary: 6, 15, 20 [locked]

q coefficient

uor	w	u	v	p	p2
0	0	0	0	0	0
0	0	0	0	0	0
0	0	0	0	0	0
0	0	0	0	0	0
0	0	0	0	0	0
-diff(r*nacc_aco,uor)	-diff(r*nacc_aco,w)	-diff(r*nacc_aco,u)	-diff(r*nacc_aco,v)	-diff(r*nacc_aco,p)	-diff(r*nacc_aco,p2)

g coefficient

0
0
0
0
0
r*nacc_aco

h coefficient

uor	w	u	v	p	p2
0	0	0	0	0	0
0	0	0	0	0	0
-diff(u0_ns-u,uor)	-diff(u0_ns-u,w)	-diff(u0_ns-u,u)	-diff(u0_ns-u,v)	-diff(u0_ns-u,p)	-diff(u0_ns-u,p2)
-diff(v0_ns-v,uor)	-diff(v0_ns-v,w)	-diff(v0_ns-v,u)	-diff(v0_ns-v,v)	-diff(v0_ns-v,p)	-diff(v0_ns-v,p2)
0	0	0	0	0	0
0	0	0	0	0	0

r coefficient

0
0
u0_ns-u
v0_ns-v
0
0

weak term

Frg_axi*uor_test*r^2
Fzg_axi*w_test*r
0
0
0
0

dweak term

w_time*p_test
0
0
0
0
0

constr term

0
0
0
0
0
0

7.2.6. Boundary: 8, 35-36, 49, 51

q coefficient

uor	w	u	v	p	p2
0	0	0	0	0	0
0	0	0	0	0	0
-diff(-r*nr_ns*p0_ns,uor)	-diff(-r*nr_ns*p0_ns,w)	-diff(-r*nr_ns*p0_ns,u)	-diff(-r*nr_ns*p0_ns,v)	-diff(-r*nr_ns*p0_ns,p)	-diff(-r*nr_ns*p0_ns,p2)
-diff(-r*nz_ns*p0_ns,uor)	-diff(-r*nz_ns*p0_ns,w)	-diff(-r*nz_ns*p0_ns,u)	-diff(-r*nz_ns*p0_ns,v)	-diff(-r*nz_ns*p0_ns,p)	-diff(-r*nz_ns*p0_ns,p2)
0	0	0	0	0	0
-diff(r*nacc_aco,uor)	-diff(r*nacc_aco,w)	-diff(r*nacc_aco,u)	-diff(r*nacc_aco,v)	-diff(r*nacc_aco,p)	-diff(r*nacc_aco,p2)

g coefficient

0
0
-r*nr_ns*p0_ns
-r*nz_ns*p0_ns
0
r*nacc_aco

h coefficient

uor	w	u	v	p	p2
0	0	0	0	0	0
0	0	0	0	0	0
-diff(-(u*tr+v*tz),uor)	-diff(-(u*tr+v*tz),w)	-diff(-(u*tr+v*tz),u)	-diff(-(u*tr+v*tz),v)	-diff(-(u*tr+v*tz),p)	-diff(-(u*tr+v*tz),p2)
0	0	0	0	0	0
0	0	0	0	0	0
0	0	0	0	0	0

r coefficient

0
0
-(u*tr+v*tz)

0
0
0

weak term

Frg_axi*uor_test*r^2
Fzg_axi*w_test*r
0
0
0
0

dweak term

0
0
0
0
0
0

constr term

0
0
0
0
0
0

7.2.7. Boundary: 11, 23, 31

q coefficient

uor	w	u	v	p	p2
0	0	0	0	0	0
0	0	0	0	0	0
-diff(-	-diff(-	-diff(-	-diff(-	-diff(-	-diff(-

r*nr_ns*p0_ns,uor)	r*nr_ns*p0_ns,w)	r*nr_ns*p0_ns,u)	r*nr_ns*p0_ns,v)	r*nr_ns*p0_ns,p)	r*nr_ns*p0_ns,p2)
-diff(-r*nz_ns*p0_ns,uor)	-diff(-r*nz_ns*p0_ns,w)	-diff(-r*nz_ns*p0_ns,u)	-diff(-r*nz_ns*p0_ns,v)	-diff(-r*nz_ns*p0_ns,p)	-diff(-r*nz_ns*p0_ns,p2)
0	0	0	0	0	0
-diff(r*nacc_aco,uor)	-diff(r*nacc_aco,w)	-diff(r*nacc_aco,u)	-diff(r*nacc_aco,v)	-diff(r*nacc_aco,p)	-diff(r*nacc_aco,p2)

g coefficient

0
0
-r*nr_ns*p0_ns
-r*nz_ns*p0_ns
0
r*nacc_aco

h coefficient

uor	w	u	v	p	p2
0	0	0	0	0	0
0	0	0	0	0	0
-diff(-(u*tr+v*tz),uor)	-diff(-(u*tr+v*tz),w)	-diff(-(u*tr+v*tz),u)	-diff(-(u*tr+v*tz),v)	-diff(-(u*tr+v*tz),p)	-diff(-(u*tr+v*tz),p2)
0	0	0	0	0	0
0	0	0	0	0	0
0	0	0	0	0	0

r coefficient

0
0
-(u*tr+v*tz)
0
0
0

weak term

Frg_axi*uor_test*r^2
Fzg_axi*w_test*r
0
0
0
0

dweak term

0
0
0
0
0
0

constr term

0
0
0
0
0
0

7.2.8. Boundary: 17, 24

q coefficient

uor	w	u	v	p	p2
0	0	0	0	0	0
0	0	0	0	0	0
-diff(-r*nr_ns*p0_ns,uor)	-diff(-r*nr_ns*p0_ns,w)	-diff(-r*nr_ns*p0_ns,u)	-diff(-r*nr_ns*p0_ns,v)	-diff(-r*nr_ns*p0_ns,p)	-diff(-r*nr_ns*p0_ns,p2)
-diff(-r*nz_ns*p0_ns,uor)	-diff(-r*nz_ns*p0_ns,w)	-diff(-r*nz_ns*p0_ns,u)	-diff(-r*nz_ns*p0_ns,v)	-diff(-r*nz_ns*p0_ns,p)	-diff(-r*nz_ns*p0_ns,p2)

0	0	0	0	0	0
-diff(r*nacc_aco,uor)	-diff(r*nacc_aco,w)	-diff(r*nacc_aaco,u)	-diff(r*nacc_aco,v)	-diff(r*nacc_aco,p)	-diff(r*nacc_aco,p2)

g coefficient

0
0
-r*nr_ns*p0_ns
-r*nz_ns*p0_ns
0
r*nacc_aco

h coefficient

uor	w	u	v	p	p2
0	0	0	0	0	0
0	0	0	0	0	0
-diff(-(u*tr+v*tz),uor)	-diff(-(u*tr+v*tz),w)	-diff(-(u*tr+v*tz),u)	-diff(-(u*tr+v*tz),v)	-diff(-(u*tr+v*tz),p)	-diff(-(u*tr+v*tz),p2)
0	0	0	0	0	0
0	0	0	0	0	0
0	0	0	0	0	0

r coefficient

0
0
-(u*tr+v*tz)
0
0
0

weak term

Frg_axi*uor_test*r^2
Fzg_axi*w_test*r

0
0
0
0

dweak term

0
0
0
0
0
0

constr term

0
0
0
0
0
0

7.2.9. Boundary: 27-28, 34, 46

q coefficient

uor	w	u	v	p	p2
0	0	0	0	0	0
0	0	0	0	0	0
-diff(-r*nr_ns*p0_ns,uor)	-diff(-r*nr_ns*p0_ns,w)	-diff(-r*nr_ns*p0_ns,u)	-diff(-r*nr_ns*p0_ns,v)	-diff(-r*nr_ns*p0_ns,p)	-diff(-r*nr_ns*p0_ns,p2)
-diff(-r*nz_ns*p0_ns,uor)	-diff(-r*nz_ns*p0_ns,w)	-diff(-r*nz_ns*p0_ns,u)	-diff(-r*nz_ns*p0_ns,v)	-diff(-r*nz_ns*p0_ns,p)	-diff(-r*nz_ns*p0_ns,p2)
0	0	0	0	0	0
-diff(r*nacc_aco,uor)	-diff(r*nacc_aco,w)	-diff(r*nacc_aco,u)	-diff(r*nacc_aco,v)	-diff(r*nacc_aco,p)	-diff(r*nacc_aco,p2)

g coefficient

0
0
-r*nr_ns*p0_ns
-r*nz_ns*p0_ns
0
r*nacc_aco

h coefficient

uor	w	u	v	p	p2
0	0	0	0	0	0
0	0	0	0	0	0
-diff(-(u*tr+v*tz),uor)	-diff(-(u*tr+v*tz),w)	-diff(-(u*tr+v*tz),u)	-diff(-(u*tr+v*tz),v)	-diff(-(u*tr+v*tz),p)	-diff(-(u*tr+v*tz),p2)
0	0	0	0	0	0
0	0	0	0	0	0
0	0	0	0	0	0

r coefficient

0
0
-(u*tr+v*tz)
0
0
0

weak term

Frg_axi*uor_test*r^2
Fzg_axi*w_test*r
0
0
0
0

dweak term

0
0
0
0
0
0

constr term

0
0
0
0
0
0

7.2.10. Boundary: 32

q coefficient

uor	w	u	v	p	p2
0	0	0	0	0	0
0	0	0	0	0	0
0	0	0	0	0	0
0	0	0	0	0	0
0	0	0	0	0	0
0	0	0	0	0	0

g coefficient

0
0
0
0
0
0

h coefficient

uor	w	u	v	p	p2
0	0	0	0	0	0
0	0	0	0	0	0
0	0	0	0	0	0
0	0	0	0	0	0
0	0	0	0	0	0
-diff(-p2,uor)	-diff(-p2,w)	-diff(-p2,u)	-diff(-p2,v)	-diff(-p2,p)	-diff(-p2,p2)

r coefficient

0
0
0
0
0
-p2

weak term

0
0
0
0
0
0

dweak term

0
0
0
0
0
0

constr term

0

0

0

0

0

0

7.3. Subdomain

Dependent variables: uor, w, u, v, p, p2

7.3.1. Subdomain: 1, 4, 7

Diffusion coefficient

uor w u v p p2

0   0 0 0 0 0

0   0 0 0 0 0

0   0 0 0 0 0

0   0 0 0 0 0

0   0 0 0 0 0

0   0 0 0 0 0

Absorption coefficient

uor w u v p p2

0   0 0 0 0 0

0   0 0 0 0 0

0   0 0 0 0 0

0   0 0 0 0 0

0   0 0 0 0 0

0   0 0 0 0 0

Source term

0

0

0

0

0
0

Mass coefficient

uor w u v p p2
0   0 0 0 0 0
0   0 0 0 0 0
0   0 0 0 0 0
0   0 0 0 0 0
0   0 0 0 0 0
0   0 0 0 0 0

Conservative flux convection coeff.

uor w   u   v   p   p2
0, 0 0, 0 0, 0 0, 0 0, 0 0, 0
0, 0 0, 0 0, 0 0, 0 0, 0 0, 0
0, 0 0, 0 0, 0 0, 0 0, 0 0, 0
0, 0 0, 0 0, 0 0, 0 0, 0 0, 0
0, 0 0, 0 0, 0 0, 0 0, 0 0, 0
0, 0 0, 0 0, 0 0, 0 0, 0 0, 0

Convection coefficient

uor w   u   v   p   p2
0, 0 0, 0 0, 0 0, 0 0, 0 0, 0
0, 0 0, 0 0, 0 0, 0 0, 0 0, 0
0, 0 0, 0 0, 0 0, 0 0, 0 0, 0
0, 0 0, 0 0, 0 0, 0 0, 0 0, 0
0, 0 0, 0 0, 0 0, 0 0, 0 0, 0
0, 0 0, 0 0, 0 0, 0 0, 0 0, 0

Conservative flux source term

0, 0
0, 0
0, 0
0, 0

0, 0
0, 0

weak term

(omega_axi^2-
j*omega_axi*alphadM_axi)*rho_axi*(uor_test*uor*r^3+w_test*w*r)-
(er_axi_test*sr_axi+ephi_axi_test*sphi_axi+ez_axi_test*sz_axi+2*erz_axi_test*srz_axi)*r-
betadK_axi*(er_axi_test*sr_t_axi+ephi_axi_test*sphi_t_axi+ez_axi_test*sz_t_axi+2*erz_axi_test*srz_t_axi)*r
0
0
0
0
0

dweak term

0
0
0
0
0
0

constr term

0
0
0
0
0
0

7.3.2. Subdomain: 2, 5-6

Diffusion coefficient

uor	w	u	v	p	p2

0	0	0	0	0	0
0	0	0	0	0	0
-diff(r*p-2*r*eta_ns*ur,uorr), -diff(-r*eta_ns*(uz+vr),uorr), -diff(r*p-2*r*eta_ns*ur,uorz), -diff(-r*eta_ns*(uz+vr),uorz)	-diff(r*p-2*r*eta_ns*ur,wr), -diff(-r*eta_ns*(uz+vr),wr), -diff(r*p-2*r*eta_ns*ur,wz), -diff(-r*eta_ns*(uz+vr),wz)	-diff(r*p-2*r*eta_ns*ur,ur), -diff(-r*eta_ns*(uz+vr),ur), -diff(r*p-2*r*eta_ns*ur,uz), -diff(-r*eta_ns*(uz+vr),uz)	-diff(r*p-2*r*eta_ns*ur,vr), -diff(-r*eta_ns*(uz+vr),vr), -diff(r*p-2*r*eta_ns*ur,vz), -diff(-r*eta_ns*(uz+vr),vz)	-diff(r*p-2*r*eta_ns*ur,pr), -diff(-r*eta_ns*(uz+vr),pr), -diff(r*p-2*r*eta_ns*ur,pz), -diff(-r*eta_ns*(uz+vr),pz)	-diff(r*p-2*r*eta_ns*ur,p2r), -diff(-r*eta_ns*(uz+vr),p2r), -diff(r*p-2*r*eta_ns*ur,p2z), -diff(-r*eta_ns*(uz+vr),p2z)
-diff(-r*eta_ns*(vr+uz),uorr), -diff(r*p-2*r*eta_ns*vz,uorr), -diff(-r*eta_ns*(vr+uz),uorz), -diff(r*p-2*r*eta_ns*vz,uorz)	-diff(-r*eta_ns*(vr+uz),wr), -diff(r*p-2*r*eta_ns*vz,wr), -diff(-r*eta_ns*(vr+uz),wz), -diff(r*p-2*r*eta_ns*vz,wz)	-diff(-r*eta_ns*(vr+uz),ur), -diff(r*p-2*r*eta_ns*vz,ur), -diff(-r*eta_ns*(vr+uz),uz), -diff(r*p-2*r*eta_ns*vz,uz)	-diff(-r*eta_ns*(vr+uz),vr), -diff(r*p-2*r*eta_ns*vz,vr), -diff(-r*eta_ns*(vr+uz),vz), -diff(r*p-2*r*eta_ns*vz,vz)	-diff(-r*eta_ns*(vr+uz),pr), -diff(r*p-2*r*eta_ns*vz,pr), -diff(-r*eta_ns*(vr+uz),pz), -diff(r*p-2*r*eta_ns*vz,pz)	-diff(-r*eta_ns*(vr+uz),p2r), -diff(r*p-2*r*eta_ns*vz,p2r), -diff(-r*eta_ns*(vr+uz),p2z), -diff(r*p-2*r*eta_ns*vz,p2z)
0	0	0	0	0	0
-diff(-r/rho_aco*p2r,uorr), -diff(-r/rho_aco*p2z,uorr), -diff(-r/rho_aco*p2r,uorz), -diff(-r/rho_aco*p2z,uorz)	-diff(-r/rho_aco*p2r,wr), -diff(-r/rho_aco*p2z,wr), -diff(-r/rho_aco*p2r,wz), -diff(-r/rho_aco*p2z,wz)	-diff(-r/rho_aco*p2r,ur), -diff(-r/rho_aco*p2z,ur), -diff(-r/rho_aco*p2r,uz), -diff(-r/rho_aco*p2z,uz)	-diff(-r/rho_aco*p2r,vr), -diff(-r/rho_aco*p2z,vr), -diff(-r/rho_aco*p2r,vz), -diff(-r/rho_aco*p2z,vz)	-diff(-r/rho_aco*p2r,pr), -diff(-r/rho_aco*p2z,pr), -diff(-r/rho_aco*p2r,pz), -diff(-r/rho_aco*p2z,pz)	-diff(-r/rho_aco*p2r,p2r), -diff(-r/rho_aco*p2z,p2r), -diff(-r/rho_aco*p2r,p2z), -diff(-r/rho_aco*p2z,p2z)

Absorption coefficient

uor	w	u	v	p	p2
0	0	0	0	0	0
0	0	0	0	0	0
-diff(p-r*rho_ns*(u*ur+v*uz)-2*eta_ns*u/r,	-diff(p-r*rho_ns*(u*ur+v*uz)-2*eta_ns*u/r	-diff(p-r*rho_ns*(u*ur+v*uz)-2*eta_ns*u/r	-diff(p-r*rho_ns*(u*ur+v*uz)-2*eta_ns*u/r	-diff(p-r*rho_ns*(u*ur+v*uz)-2*eta_ns*u/r	-diff(p-r*rho_ns*(u*ur+v*uz)-2*eta_ns*u/r,

uor)	,w)	,u)	,v)	,p)	p2)
-diff(-r*rho_ns*(u*vr+v*vz),uor)	-diff(-r*rho_ns*(u*vr+v*vz),w)	-diff(-r*rho_ns*(u*vr+v*vz),u)	-diff(-r*rho_ns*(u*vr+v*vz),v)	-diff(-r*rho_ns*(u*vr+v*vz),p)	-diff(-r*rho_ns*(u*vr+v*vz),p2)
-diff(-(r*(ur+vz)+u),uor)	-diff(-(r*(ur+vz)+u),w)	-diff(-(r*(ur+vz)+u),u)	-diff(-(r*(ur+vz)+u),v)	-diff(-(r*(ur+vz)+u),p)	-diff(-(r*(ur+vz)+u),p2)
-diff(r*omega_aco^2/(rho_aco*cs_aco^2)*p2,uor)	-diff(r*omega_aco^2/(rho_aco*cs_aco^2)*p2,w)	-diff(r*omega_aco^2/(rho_aco*cs_aco^2)*p2,u)	-diff(r*omega_aco^2/(rho_aco*cs_aco^2)*p2,v)	-diff(r*omega_aco^2/(rho_aco*cs_aco^2)*p2,p)	-diff(r*omega_aco^2/(rho_aco*cs_aco^2)*p2,p2)

Source term

```
0
0
p-r*rho_ns*(u*ur+v*uz)-2*eta_ns*u/r
-r*rho_ns*(u*vr+v*vz)
-(r*(ur+vz)+u)
r*omega_aco^2/(rho_aco*cs_aco^2)*p2
```

Mass coefficient

uor	w	u	v	p	p2
0	0	0	0	0	0
0	0	0	0	0	0
0	0	r*rho_ns	0	0	0
0	0	0	r*rho_ns	0	0
0	0	0	0	0	0
0	0	0	0	0	0

Conservative flux convection coeff.

uor	w	u	v	p	p2
0, 0	0, 0	0, 0	0, 0	0, 0	0, 0
0, 0	0, 0	0, 0	0, 0	0, 0	0, 0
-diff(r*p-2*r*eta_ns*ur,uor), -diff(-	-diff(r*p-2*r*eta_ns*ur,w), -diff(-	-diff(r*p-2*r*eta_ns*ur,u), -diff(-	-diff(r*p-2*r*eta_ns*ur,v), -diff(-	-diff(r*p-2*r*eta_ns*ur,p), -diff(-	-diff(r*p-2*r*eta_ns*ur,p2), -diff(-

r*eta_ns*(uz+vr),uor)	r*eta_ns*(uz+vr),w)	r*eta_ns*(uz+vr),u)	r*eta_ns*(uz+vr),v)	r*eta_ns*(uz+vr),p)	r*eta_ns*(uz+vr),p2)
-diff(-r*eta_ns*(vr+uz),uor), -diff(r*p-2*r*eta_ns*vz,uor)	-diff(-r*eta_ns*(vr+uz),w), -diff(r*p-2*r*eta_ns*vz,w)	-diff(-r*eta_ns*(vr+uz),u), -diff(r*p-2*r*eta_ns*vz,u)	-diff(-r*eta_ns*(vr+uz),v), -diff(r*p-2*r*eta_ns*vz,v)	-diff(-r*eta_ns*(vr+uz),p), -diff(r*p-2*r*eta_ns*vz,p)	-diff(-r*eta_ns*(vr+uz),p2), -diff(r*p-2*r*eta_ns*vz,p2)
0, 0	0, 0	0, 0	0, 0	0, 0	0, 0
-diff(-r/rho_aco*p2r,uor), -diff(-r/rho_aco*p2z,uor)	-diff(-r/rho_aco*p2r,w), -diff(-r/rho_aco*p2z,w)	-diff(-r/rho_aco*p2r,u), -diff(-r/rho_aco*p2z,u)	-diff(-r/rho_aco*p2r,v), -diff(-r/rho_aco*p2z,v)	-diff(-r/rho_aco*p2r,p), -diff(-r/rho_aco*p2z,p)	-diff(-r/rho_aco*p2r,p2), -diff(-r/rho_aco*p2z,p2)

Convection coefficient

uor	w	u	v	p	p2
0, 0	0, 0	0, 0	0, 0	0, 0	0, 0
0, 0	0, 0	0, 0	0, 0	0, 0	0, 0
-diff(p-r*rho_ns*(u*ur+v*uz)-2*eta_ns*u/r, uorr), -diff(p-r*rho_ns*(u*ur+v*uz)-2*eta_ns*u/r, uorz)	-diff(p-r*rho_ns*(u*ur+v*uz)-2*eta_ns*u/r,wr), -diff(p-r*rho_ns*(u*ur+v*uz)-2*eta_ns*u/r,wz)	-diff(p-r*rho_ns*(u*ur+v*uz)-2*eta_ns*u/r,ur), -diff(p-r*rho_ns*(u*ur+v*uz)-2*eta_ns*u/r,uz)	-diff(p-r*rho_ns*(u*ur+v*uz)-2*eta_ns*u/r,vr), -diff(p-r*rho_ns*(u*ur+v*uz)-2*eta_ns*u/r,vz)	-diff(p-r*rho_ns*(u*ur+v*uz)-2*eta_ns*u/r,pr), -diff(p-r*rho_ns*(u*ur+v*uz)-2*eta_ns*u/r,pz)	-diff(p-r*rho_ns*(u*ur+v*uz)-2*eta_ns*u/r,p2r), -diff(p-r*rho_ns*(u*ur+v*uz)-2*eta_ns*u/r,p2z)
-diff(-r*rho_ns*(u*vr+v*vz),uorr), -diff(-r*rho_ns*(u*vr+v*vz),uorz)	-diff(-r*rho_ns*(u*vr+v*vz),wr), -diff(-r*rho_ns*(u*vr+v*vz),wz)	-diff(-r*rho_ns*(u*vr+v*vz),ur), -diff(-r*rho_ns*(u*vr+v*vz),uz)	-diff(-r*rho_ns*(u*vr+v*vz),vr), -diff(-r*rho_ns*(u*vr+v*vz),vz)	-diff(-r*rho_ns*(u*vr+v*vz),pr), -diff(-r*rho_ns*(u*vr+v*vz),pz)	-diff(-r*rho_ns*(u*vr+v*vz),p2r), -diff(-r*rho_ns*(u*vr+v*vz),p2z)
-diff(-(r*(ur+vz)+u),uorr), -diff(-(r*(ur+vz)+u),uorz)	-diff(-(r*(ur+vz)+u),wr), -diff(-(r*(ur+vz)+u),wz)	-diff(-(r*(ur+vz)+u),ur), -diff(-(r*(ur+vz)+u),uz)	-diff(-(r*(ur+vz)+u),vr), -diff(-(r*(ur+vz)+u),vz)	-diff(-(r*(ur+vz)+u),pr), -diff(-(r*(ur+vz)+u),pz)	-diff(-(r*(ur+vz)+u),p2r), -diff(-(r*(ur+vz)+u),p2z)
-diff(r*omega_aco^2/(rho_	-diff(r*omega_aco^2/(rho	-diff(r*omega_aco^2/(rho	-diff(r*omega_aco^2/(rho	-diff(r*omega_aco^2/(rho	-diff(r*omega_aco^2/(rho_

aco*cs_aco^2)*p2,uorr), - diff(r*omega_aco^2/(rho_aco*cs_aco^2)*p2,uorz)	_aco*cs_aco^2)*p2,wr), - diff(r*omega_aco^2/(rho_aco*cs_aco^2)*p2,wz)	_aco*cs_aco^2)*p2,ur), - diff(r*omega_aco^2/(rho_aco*cs_aco^2)*p2,uz)	_aco*cs_aco^2)*p2,vr), - diff(r*omega_aco^2/(rho_aco*cs_aco^2)*p2,vz)	_aco*cs_aco^2)*p2,pr), - diff(r*omega_aco^2/(rho_aco*cs_aco^2)*p2,pz)	aco*cs_aco^2)*p2,p2r), - diff(r*omega_aco^2/(rho_aco*cs_aco^2)*p2,p2z)

Conservative flux source term

0, 0
0, 0
r*p-2*r*eta_ns*ur, -r*eta_ns*(uz+vr)
-r*eta_ns*(vr+uz), r*p-2*r*eta_ns*vz
0, 0
-r/rho_aco*p2r, -r/rho_aco*p2z

weak term

0
0
0
0
0
0

dweak term

0
0
0
0
0
0

constr term

0
0
0

0
0
0

7.3.3. Subdomain: 3

Diffusion coefficient

uor	w	u	v	p	p2
0	0	0	0	0	0
0	0	0	0	0	0
-diff(r*p-2*r*eta_ns*ur ,uorr), -diff(-r*eta_ns*(uz+vr),uorr), -diff(r*p-2*r*eta_ns*ur ,uorz), -diff(-r*eta_ns*(uz+vr),uorz)	-diff(r*p-2*r*eta_ns*ur,wr), -diff(-r*eta_ns*(uz+vr),wr), -diff(r*p-2*r*eta_ns*ur,wz), -diff(-r*eta_ns*(uz+vr),wz)	-diff(r*p-2*r*eta_ns*ur,ur), -diff(-r*eta_ns*(uz+vr),ur), -diff(r*p-2*r*eta_ns*ur,uz), -diff(-r*eta_ns*(uz+vr),uz)	-diff(r*p-2*r*eta_ns*ur,vr), -diff(-r*eta_ns*(uz+vr),vr), -diff(r*p-2*r*eta_ns*ur,vz), -diff(-r*eta_ns*(uz+vr),vz)	-diff(r*p-2*r*eta_ns*ur,pr), -diff(-r*eta_ns*(uz+vr),pr), -diff(r*p-2*r*eta_ns*ur,pz), -diff(-r*eta_ns*(uz+vr),pz)	-diff(r*p-2*r*eta_ns*ur,p2r), -diff(-r*eta_ns*(uz+vr),p2r), -diff(r*p-2*r*eta_ns*ur,p2z), -diff(-r*eta_ns*(uz+vr),p2z)
-diff(-r*eta_ns*(vr+uz),uorr), -diff(r*p-2*r*eta_ns*vz,uorr), -diff(-r*eta_ns*(vr+uz),uorz), -diff(r*p-2*r*eta_ns*vz,uorz)	-diff(-r*eta_ns*(vr+uz),wr), -diff(r*p-2*r*eta_ns*vz,wr), -diff(-r*eta_ns*(vr+uz),wz), -diff(r*p-2*r*eta_ns*vz,wz)	-diff(-r*eta_ns*(vr+uz),ur), -diff(r*p-2*r*eta_ns*vz,ur), -diff(-r*eta_ns*(vr+uz),uz), -diff(r*p-2*r*eta_ns*vz,uz)	-diff(-r*eta_ns*(vr+uz),vr), -diff(r*p-2*r*eta_ns*vz,vr), -diff(-r*eta_ns*(vr+uz),vz), -diff(r*p-2*r*eta_ns*vz,vz)	-diff(-r*eta_ns*(vr+uz),pr), -diff(r*p-2*r*eta_ns*vz,pr), -diff(-r*eta_ns*(vr+uz),pz), -diff(r*p-2*r*eta_ns*vz,pz)	-diff(-r*eta_ns*(vr+uz),p2r), -diff(r*p-2*r*eta_ns*vz,p2r), -diff(-r*eta_ns*(vr+uz),p2z), -diff(r*p-2*r*eta_ns*vz,p2z)
0	0	0	0	0	0
-diff(-r/rho_aco*p2r ,uorr), -diff(-r/rho_aco*p2z,uorr), -diff(-r/rho_aco*p2r ,uorz), -diff(-r/rho_aco*p2z,uorz)	-diff(-r/rho_aco*p2r,wr), -diff(-r/rho_aco*p2z,wr), -diff(-r/rho_aco*p2r,wz), -diff(-r/rho_aco*p2z,wz)	-diff(-r/rho_aco*p2r,ur), -diff(-r/rho_aco*p2z,ur), -diff(-r/rho_aco*p2r,uz), -diff(-r/rho_aco*p2z,uz)	-diff(-r/rho_aco*p2r,vr), -diff(-r/rho_aco*p2z,vr), -diff(-r/rho_aco*p2r,vz), -diff(-r/rho_aco*p2z,vz)	-diff(-r/rho_aco*p2r,pr), -diff(-r/rho_aco*p2z,pr), -diff(-r/rho_aco*p2r,pz), -diff(-r/rho_aco*p2z,pz)	-diff(-r/rho_aco*p2r,p2r), -diff(-r/rho_aco*p2z,p2r), -diff(-r/rho_aco*p2r,p2z), -diff(-r/rho_aco*p2z,p2z)

Absorption coefficient

uor	w	u	v	p	p2
0	0	0	0	0	0
0	0	0	0	0	0
-diff(p-r*rho_ns*(u*ur+v*uz)-2*eta_ns*u/r, uor)	-diff(p-r*rho_ns*(u*ur+v*uz)-2*eta_ns*u/r ,w)	-diff(p-r*rho_ns*(u*ur+v*uz)-2*eta_ns*u/r ,u)	-diff(p-r*rho_ns*(u*ur+v*uz)-2*eta_ns*u/r ,v)	-diff(p-r*rho_ns*(u*ur+v*uz)-2*eta_ns*u/r ,p)	-diff(p-r*rho_ns*(u*ur+v*uz)-2*eta_ns*u/r, p2)
-diff(-r*rho_ns*(u*vr+v*vz),uor)	-diff(-r*rho_ns*(u*vr+v*vz),w)	-diff(-r*rho_ns*(u*vr+v*vz),u)	-diff(-r*rho_ns*(u*vr+v*vz),v)	-diff(-r*rho_ns*(u*vr+v*vz),p)	-diff(-r*rho_ns*(u*vr+v*vz),p2)
-diff(-(r*(ur+vz)+u), uor)	-diff(-(r*(ur+vz)+u) ,w)	-diff(-(r*(ur+vz)+u) ,u)	-diff(-(r*(ur+vz)+u) ,v)	-diff(-(r*(ur+vz)+u) ,p)	-diff(-(r*(ur+vz)+u) ,p2)
-diff(r*omega_aco^2/(rho_aco*cs_aco^2)*p2,uor)	-diff(r*omega_aco^2/(rho_aco*cs_aco^2)*p2,w)	-diff(r*omega_aco^2/(rho_aco*cs_aco^2)*p2,u)	-diff(r*omega_aco^2/(rho_aco*cs_aco^2)*p2,v)	-diff(r*omega_aco^2/(rho_aco*cs_aco^2)*p2,p)	-diff(r*omega_aco^2/(rho_aco*cs_aco^2)*p2,p2)

Source term

0
0
p-r*rho_ns*(u*ur+v*uz)-2*eta_ns*u/r
-r*rho_ns*(u*vr+v*vz)
-(r*(ur+vz)+u)
r*omega_aco^2/(rho_aco*cs_aco^2)*p2

Mass coefficient

uor	w	u	v	p	p2
0	0	0	0	0	0
0	0	0	0	0	0
0	0	r*rho_ns	0	0	0
0	0	0	r*rho_ns	0	0
0	0	0	0	0	0
0	0	0	0	0	0

Conservative flux convection coeff.

uor	w	u	v	p	p2
0, 0	0, 0	0, 0	0, 0	0, 0	0, 0
0, 0	0, 0	0, 0	0, 0	0, 0	0, 0
-diff(r*p-2*r*eta_ns*ur,uor), -diff(-r*eta_ns*(uz+vr),uor)	-diff(r*p-2*r*eta_ns*ur,w), -diff(-r*eta_ns*(uz+vr),w)	-diff(r*p-2*r*eta_ns*ur,u), -diff(-r*eta_ns*(uz+vr),u)	-diff(r*p-2*r*eta_ns*ur,v), -diff(-r*eta_ns*(uz+vr),v)	-diff(r*p-2*r*eta_ns*ur,p), -diff(-r*eta_ns*(uz+vr),p)	-diff(r*p-2*r*eta_ns*ur,p2), -diff(-r*eta_ns*(uz+vr),p2)
-diff(-r*eta_ns*(vr+uz),uor), -diff(r*p-2*r*eta_ns*vz,uor)	-diff(-r*eta_ns*(vr+uz),w), -diff(r*p-2*r*eta_ns*vz,w)	-diff(-r*eta_ns*(vr+uz),u), -diff(r*p-2*r*eta_ns*vz,u)	-diff(-r*eta_ns*(vr+uz),v), -diff(r*p-2*r*eta_ns*vz,v)	-diff(-r*eta_ns*(vr+uz),p), -diff(r*p-2*r*eta_ns*vz,p)	-diff(-r*eta_ns*(vr+uz),p2), -diff(r*p-2*r*eta_ns*vz,p2)
0, 0	0, 0	0, 0	0, 0	0, 0	0, 0
-diff(-r/rho_aco*p2r,uor), -diff(-r/rho_aco*p2z,uor)	-diff(-r/rho_aco*p2r,w), -diff(-r/rho_aco*p2z,w)	-diff(-r/rho_aco*p2r,u), -diff(-r/rho_aco*p2z,u)	-diff(-r/rho_aco*p2r,v), -diff(-r/rho_aco*p2z,v)	-diff(-r/rho_aco*p2r,p), -diff(-r/rho_aco*p2z,p)	-diff(-r/rho_aco*p2r,p2), -diff(-r/rho_aco*p2z,p2)

Convection coefficient

uor	w	u	v	p	p2
0, 0	0, 0	0, 0	0, 0	0, 0	0, 0
0, 0	0, 0	0, 0	0, 0	0, 0	0, 0
-diff(p-r*rho_ns*(u*ur+v*uz)-2*eta_ns*u/r,uorr), -diff(p-r*rho_ns*(u*ur+v*uz)-2*eta_ns*u/r,uorz)	-diff(p-r*rho_ns*(u*ur+v*uz)-2*eta_ns*u/r,wr), -diff(p-r*rho_ns*(u*ur+v*uz)-2*eta_ns*u/r,wz)	-diff(p-r*rho_ns*(u*ur+v*uz)-2*eta_ns*u/r,ur), -diff(p-r*rho_ns*(u*ur+v*uz)-2*eta_ns*u/r,uz)	-diff(p-r*rho_ns*(u*ur+v*uz)-2*eta_ns*u/r,vr), -diff(p-r*rho_ns*(u*ur+v*uz)-2*eta_ns*u/r,vz)	-diff(p-r*rho_ns*(u*ur+v*uz)-2*eta_ns*u/r,pr), -diff(p-r*rho_ns*(u*ur+v*uz)-2*eta_ns*u/r,pz)	-diff(p-r*rho_ns*(u*ur+v*uz)-2*eta_ns*u/r,p2r), -diff(p-r*rho_ns*(u*ur+v*uz)-2*eta_ns*u/r,p2z)
-diff(-r*rho_ns*(u*vr+v*vz),uorr), -diff(-r*rho_ns*(u*v	-diff(-r*rho_ns*(u*vr+v*vz),wr), -diff(-r*rho_ns*(u*	-diff(-r*rho_ns*(u*vr+v*vz),ur), -diff(-r*rho_ns*(u*	-diff(-r*rho_ns*(u*vr+v*vz),vr), -diff(-r*rho_ns*(u*	-diff(-r*rho_ns*(u*vr+v*vz),pr), -diff(-r*rho_ns*(u*	-diff(-r*rho_ns*(u*vr+v*vz),p2r), -diff(-r*rho_ns*(u*

r+v*vz),uorz)	vr+v*vz),wz)	vr+v*vz),uz)	vr+v*vz),vz)	vr+v*vz),pz)	vr+v*vz),p2z)
-diff(-(r*(ur+vz)+u)uorr), -diff(-(r*(ur+vz)+u),uorz)	-diff(-(r*(ur+vz)+u),wr), -diff(-(r*(ur+vz)+u),wz)	-diff(-(r*(ur+vz)+u),ur), -diff(-(r*(ur+vz)+u),uz)	-diff(-(r*(ur+vz)+u),vr), -diff(-(r*(ur+vz)+u),vz)	-diff(-(r*(ur+vz)+u),pr), -diff(-(r*(ur+vz)+u),pz)	-diff(-(r*(ur+vz)+u),p2r), -diff(-(r*(ur+vz)+u),p2z)
-diff(r*omega_aco^2/(rho_aco*cs_aco^2)*p2,uorr), -diff(r*omega_aco^2/(rho_aco*cs_aco^2)*p2,uorz)	-diff(r*omega_aco^2/(rho_aco*cs_aco^2)*p2,wr), -diff(r*omega_aco^2/(rho_aco*cs_aco^2)*p2,wz)	-diff(r*omega_aco^2/(rho_aco*cs_aco^2)*p2,ur), -diff(r*omega_aco^2/(rho_aco*cs_aco^2)*p2,uz)	-diff(r*omega_aco^2/(rho_aco*cs_aco^2)*p2,vr), -diff(r*omega_aco^2/(rho_aco*cs_aco^2)*p2,vz)	-diff(r*omega_aco^2/(rho_aco*cs_aco^2)*p2,pr), -diff(r*omega_aco^2/(rho_aco*cs_aco^2)*p2,pz)	-diff(r*omega_aco^2/(rho_aco*cs_aco^2)*p2,p2r), -diff(r*omega_aco^2/(rho_aco*cs_aco^2)*p2,p2z)

Conservative flux source term

0, 0
0, 0
r*p-2*r*eta_ns*ur, -r*eta_ns*(uz+vr)
-r*eta_ns*(vr+uz), r*p-2*r*eta_ns*vz
0, 0
-r/rho_aco*p2r, -r/rho_aco*p2z

weak term

0
0
0
0
0
0

dweak term

0
0
0
0

0

0

constr term

0

0

0

0

0

0

7.3.4. Subdomain: 8

Diffusion coefficient

uor	w	u	v	p	p2
0	0	0	0	0	0
0	0	0	0	0	0
0	0	0	0	0	0
0	0	0	0	0	0
0	0	0	0	0	0
0	0	0	0	0	0

Absorption coefficient

uor	w	u	v	p	p2
0	0	0	0	0	0
0	0	0	0	0	0
0	0	0	0	0	0
0	0	0	0	0	0
0	0	0	0	0	0
0	0	0	0	0	0

Source term

0

0

0

0
0
0

Mass coefficient

uor w u v p p2
0   0 0 0 0 0
0   0 0 0 0 0
0   0 0 0 0 0
0   0 0 0 0 0
0   0 0 0 0 0
0   0 0 0 0 0

Conservative flux convection coeff.

uor w   u   v   p   p2
0, 0 0, 0 0, 0 0, 0 0, 0 0, 0
0, 0 0, 0 0, 0 0, 0 0, 0 0, 0
0, 0 0, 0 0, 0 0, 0 0, 0 0, 0
0, 0 0, 0 0, 0 0, 0 0, 0 0, 0
0, 0 0, 0 0, 0 0, 0 0, 0 0, 0
0, 0 0, 0 0, 0 0, 0 0, 0 0, 0

Convection coefficient

uor w   u   v   p   p2
0, 0 0, 0 0, 0 0, 0 0, 0 0, 0
0, 0 0, 0 0, 0 0, 0 0, 0 0, 0
0, 0 0, 0 0, 0 0, 0 0, 0 0, 0
0, 0 0, 0 0, 0 0, 0 0, 0 0, 0
0, 0 0, 0 0, 0 0, 0 0, 0 0, 0
0, 0 0, 0 0, 0 0, 0 0, 0 0, 0

Conservative flux source term

0, 0
0, 0
0, 0

0, 0
0, 0
0, 0

weak term

(omega_axi^2-
j*omega_axi*alphadM_axi)*rho_axi*(uor_test*uor*r^3+w_test*w*r)-
(er_axi_test*sr_axi+ephi_axi_test*sphi_axi+ez_axi_test*sz_axi+2*erz_axi_test*sr
z_axi)*r-
betadK_axi*(er_axi_test*sr_t_axi+ephi_axi_test*sphi_t_axi+ez_axi_test*sz_t_axi
+2*erz_axi_test*srz_t_axi)*r
0
0
0
0
0

dweak term

0
0
0
0
0
0

constr term

0
0
0
0
0
0

7.3.5. Subdomain: 9

Diffusion coefficient

uor w u v p p2
0   0 0 0 0 0
0   0 0 0 0 0
0   0 0 0 0 0
0   0 0 0 0 0
0   0 0 0 0 0
0   0 0 0 0 0

Absorption coefficient

uor w u v p p2
0   0 0 0 0 0
0   0 0 0 0 0
0   0 0 0 0 0
0   0 0 0 0 0
0   0 0 0 0 0
0   0 0 0 0 0

Source term

0
0
0
0
0
0

Mass coefficient

uor w u v p p2
0   0 0 0 0 0
0   0 0 0 0 0
0   0 0 0 0 0
0   0 0 0 0 0
0   0 0 0 0 0
0   0 0 0 0 0

Conservative flux convection coeff.

uor w   u   v   p   p2
0, 0 0, 0 0, 0 0, 0 0, 0 0, 0
0, 0 0, 0 0, 0 0, 0 0, 0 0, 0
0, 0 0, 0 0, 0 0, 0 0, 0 0, 0
0, 0 0, 0 0, 0 0, 0 0, 0 0, 0
0, 0 0, 0 0, 0 0, 0 0, 0 0, 0
0, 0 0, 0 0, 0 0, 0 0, 0 0, 0

Convection coefficient

uor w   u   v   p   p2
0, 0 0, 0 0, 0 0, 0 0, 0 0, 0
0, 0 0, 0 0, 0 0, 0 0, 0 0, 0
0, 0 0, 0 0, 0 0, 0 0, 0 0, 0
0, 0 0, 0 0, 0 0, 0 0, 0 0, 0
0, 0 0, 0 0, 0 0, 0 0, 0 0, 0
0, 0 0, 0 0, 0 0, 0 0, 0 0, 0

Conservative flux source term

0, 0
0, 0
0, 0
0, 0
0, 0
0, 0

weak term

$(omega\_axi^2-j*omega\_axi*alphadM\_axi)*rho\_axi*(uor\_test*uor*r^3+w\_test*w*r)-(er\_axi\_test*sr\_axi+ephi\_axi\_test*sphi\_axi+ez\_axi\_test*sz\_axi+2*erz\_axi\_test*srz\_axi)*r-betadK\_axi*(er\_axi\_test*sr\_t\_axi+ephi\_axi\_test*sphi\_t\_axi+ez\_axi\_test*sz\_t\_axi+2*erz\_axi\_test*srz\_t\_axi)*r$
0
0
0
0

0

dweak term

0
0
0
0
0
0

constr term

0
0
0
0
0
0

7.3.6. Subdomain: 10

Diffusion coefficient

uor w u v p p2
0   0 0 0 0 0
0   0 0 0 0 0
0   0 0 0 0 0
0   0 0 0 0 0
0   0 0 0 0 0
0   0 0 0 0 0

Absorption coefficient

uor w u v p p2
0   0 0 0 0 0
0   0 0 0 0 0
0   0 0 0 0 0
0   0 0 0 0 0

```
0    0 0 0 0 0
0    0 0 0 0 0
```

Source term

```
0
0
0
0
0
0
```

Mass coefficient

```
uor w u v p p2
0    0 0 0 0 0
0    0 0 0 0 0
0    0 0 0 0 0
0    0 0 0 0 0
0    0 0 0 0 0
0    0 0 0 0 0
```

Conservative flux convection coeff.

```
uor w    u    v    p    p2
0, 0 0, 0 0, 0 0, 0 0, 0 0, 0
0, 0 0, 0 0, 0 0, 0 0, 0 0, 0
0, 0 0, 0 0, 0 0, 0 0, 0 0, 0
0, 0 0, 0 0, 0 0, 0 0, 0 0, 0
0, 0 0, 0 0, 0 0, 0 0, 0 0, 0
0, 0 0, 0 0, 0 0, 0 0, 0 0, 0
```

Convection coefficient

```
uor w    u    v    p    p2
0, 0 0, 0 0, 0 0, 0 0, 0 0, 0
0, 0 0, 0 0, 0 0, 0 0, 0 0, 0
0, 0 0, 0 0, 0 0, 0 0, 0 0, 0
0, 0 0, 0 0, 0 0, 0 0, 0 0, 0
```

0, 0 0, 0 0, 0 0, 0 0, 0 0, 0
0, 0 0, 0 0, 0 0, 0 0, 0 0, 0

Conservative flux source term

0, 0
0, 0
0, 0
0, 0
0, 0
0, 0

weak term

Frg_axi*uor_test*r^2-
(er_axi_test*sr_axi+ephi_axi_test*sphi_axi+ez_axi_test*sz_axi+2*erz_axi_test*sr
z_axi)*r-
betadK_axi*(er_axi_test*sr_t_axi+ephi_axi_test*sphi_t_axi+ez_axi_test*sz_t_axi
+2*erz_axi_test*srz_t_axi)*r+(omega_axi^2-
j*omega_axi*alphadM_axi)*rho_axi*(uor_test*uor*r^3+w_test*w*r)
0
0
0
0
0

dweak term

0
0
0
0
0
0

constr term

0
0
0

0
0
0

8. Variables

8.1. Point

Name	Description	Expression
Frg_axi	Point load in global r-dir.	0
Fzg_axi	Point load in global z-dir.	0
disp_axi	Total displacement	sqrt(real(uaxi_axi)^2+real(w)^2)
uaxi_axi	r-displacement	uor * r
uaxir_axi	r derivative of r displacement	uorr * r+uor
uaxiz_axi	z derivative of r displacement	uorz * r
uaxi_amp_axi	Disp. amplitude r-dir.	abs(uaxi_axi)
uaxi_ph_axi	Disp. phase r-dir.	180/pi * mod(angle(uaxi_axi),2 * pi)
uaxi_t_axi	r-velocity	omega_axi * j * uaxi_axi
uaxi_t_amp_axi	r-velocity amp.	omega_axi * uaxi_amp_axi
uaxi_t_ph_axi	r-velocity phase	mod(90+uaxi_ph_axi,360)
uaxi_tt_axi	r-acceleration	-omega_axi^2 * uaxi_axi
uaxi_tt_amp_axi	r-acceleration amp.	omega_axi^2 * uaxi_amp_axi
uaxi_tt_ph_axi	r-acceleration phase	mod(180+uaxi_ph_axi,360)
w_amp_axi	Disp. amplitude z-dir.	abs(w)
w_ph_axi	Disp. phase z-dir.	180/pi * mod(angle(w),2 * pi)
w_t	z-velocity	omega_axi * j * w
w_t_amp_axi	z-velocity amp.	omega_axi * w_amp_axi
w_t_ph_axi	z-velocity phase	mod(90+w_ph_axi,360)
w_tt_axi	z-acceleration	-omega_axi^2 * w
w_tt_amp_axi	z-acceleration amp.	omega_axi^2 * w_amp_axi
w_tt_ph_axi	z-acceleration phase	mod(180+w_ph_axi,360)

8.2. Boundary

Name	Description	Expression
Frg_axi	Edge load in global r-dir.	0
Fzg_axi	Edge load in global z-dir.	0
disp_axi	Total displacement	sqrt(real(uaxi_axi)^2+real(w)^2)
uaxi_axi	r-displacement	uor * r
uaxir_axi	r derivative of r displacement	uorr * r+uor
uaxiz_axi	z derivative of r displacement	uorz * r
uaxi_amp_axi	Disp. amplitude r-dir.	abs(uaxi_axi)
uaxi_ph_axi	Disp. phase r-dir.	180/pi * mod(angle(uaxi_axi),2 * pi)
uaxi_t_axi	r-velocity	omega_axi * j * uaxi_axi
uaxi_t_amp_axi	r-velocity amp.	omega_axi * uaxi_amp_axi
uaxi_t_ph_axi	r-velocity phase	mod(90+uaxi_ph_axi,360)
uaxi_tt_axi	r-acceleration	-omega_axi^2 * uaxi_axi
uaxi_tt_amp_axi	r-acceleration amp.	omega_axi^2 * uaxi_amp_axi
uaxi_tt_ph_axi	r-acceleration phase	mod(180+uaxi_ph_axi,360)
w_amp_axi	Disp. amplitude z-dir.	abs(w)
w_ph_axi	Disp. phase z-dir.	180/pi * mod(angle(w),2 * pi)
w_t	z-velocity	omega_axi * j * w
w_t_amp_axi	z-velocity amp.	omega_axi * w_amp_axi
w_t_ph_axi	z-velocity phase	mod(90+w_ph_axi,360)
w_tt_axi	z-acceleration	-omega_axi^2 * w
w_tt_amp_axi	z-acceleration amp.	omega_axi^2 * w_amp_axi
w_tt_ph_axi	z-acceleration phase	mod(180+w_ph_axi,360)
Tar_axi	Surface traction (force/area) in r-dir.	nr_axi * sr_axi+nz_axi * srz_axi
Tar_amp_axi	Surface traction amp. (force/area) in r-dir.	abs(Tar_axi)
Tar_ph_axi	Surface traction phase (force/area) in r-dir.	180/pi * mod(angle(Tar_axi),2 * pi)
Taz_axi	Surface traction (force/area) in z-dir.	nr_axi * srz_axi+nz_axi * sz_axi
Taz_amp_axi	Surface traction amp. (force/area) in z-dir.	abs(Taz_axi)
Taz_ph_axi	Surface traction phase (force/area) in z-dir.	180/pi * mod(angle(Taz_axi),2 * pi)
K_r_ns	Viscous force per area, r component	

T_r_ns	Total force per area, r component	
K_z_ns	Viscous force per area, z component	
T_z_ns	Total force per area, z component	
na_aco	Normal acceleration	
nv_aco	Normal velocity	

8.3. Subdomain

Name	Description	Expression
Frg_axi	Body load in global r-dir.	0
Fzg_axi	Body load in global z-dir.	0
disp_axi	Total displacement	sqrt(real(uaxi_axi)^2+real(w)^2)
uaxi_axi	r-displacement	uor * r
uaxir_axi	r derivative of r displacement	uorr * r+uor
uaxiz_axi	z derivative of r displacement	uorz * r
uaxi_amp_axi	Disp. amplitude r-dir.	abs(uaxi_axi)
uaxi_ph_axi	Disp. phase r-dir.	180/pi * mod(angle(uaxi_axi),2 * pi)
uaxi_t_axi	r-velocity	omega_axi * j * uaxi_axi
uaxi_t_amp_axi	r-velocity amp.	omega_axi * uaxi_amp_axi
uaxi_t_ph_axi	r-velocity phase	mod(90+uaxi_ph_axi,360)
uaxi_tt_axi	r-	-omega_axi^2 * uaxi_axi

		acceleration
uaxi_tt_amp_axi	r-acceleration amp.	omega_axi^2 * uaxi_amp_axi
uaxi_tt_ph_axi	r-acceleration phase	mod(180+uaxi_ph_axi,360)
w_amp_axi	Disp. amplitude z-dir.	abs(w)
w_ph_axi	Disp. phase z-dir.	180/pi * mod(angle(w),2 * pi)
w_t	z-velocity	omega_axi * j * w
w_t_amp_axi	z-velocity amp.	omega_axi * w_amp_axi
w_t_ph_axi	z-velocity phase	mod(90+w_ph_axi,360)
w_tt_axi	z-acceleration	-omega_axi^2 * w
w_tt_amp_axi	z-acceleration amp.	omega_axi^2 * w_amp_axi
w_tt_ph_axi	z-acceleration phase	mod(180+w_ph_axi,360)
sr_axi	sr normal stress global sys.	E_axi/((1+nu_axi) * (1-2 * nu_axi)) * (1-nu_axi) * er_axi+E_axi/((1+nu_axi) * (1-2 * nu_axi)) * nu_axi * ephi_axi+E_axi/((1+nu_axi) * (1-2 * nu_axi)) * nu_axi * ez_axi
sz_axi	sz normal stress global sys.	E_axi/((1+nu_axi) * (1-2 * nu_axi)) * nu_axi * er_axi+E_axi/((1+nu_axi) * (1-2 * nu_axi)) * nu_axi * ephi_axi+E_axi/((1+nu_axi) * (1-2 * nu_axi)) * (1-nu_axi) * ez_axi
sphi_axi	sphi normal stress	E_axi/((1+nu_axi) * (1-2 * nu_axi)) * nu_axi * er_axi+E_axi/((1+nu_axi) * (1-2 * nu_axi)) * (1-nu_axi) * ephi_axi+E_axi/((1+nu_axi) * (1-2 * nu_axi)) * nu_axi * ez_axi
srz_axi	srz shear stress global sys.	E_axi/(1+nu_axi) * erz_axi
sr_t_axi	Time der. of normal	E_axi/((1+nu_axi) * (1-2 * nu_axi)) * (1-nu_axi) * er_t_axi+E_axi/((1+nu_axi) * (1-2 * nu_axi)) *

	stress global sys. (sr)	nu_axi * ephi_t_axi+E_axi/((1+nu_axi) * (1-2 * nu_axi)) * nu_axi * ez_t_axi
sz_t_axi	Time der. of normal stress global sys. (sz)	E_axi/((1+nu_axi) * (1-2 * nu_axi)) * nu_axi * er_t_axi+E_axi/((1+nu_axi) * (1-2 * nu_axi)) * nu_axi * ephi_t_axi+E_axi/((1+nu_axi) * (1-2 * nu_axi)) * (1-nu_axi) * ez_t_axi
sphi_t_axi	Time der. of normal stress (sphi)	E_axi/((1+nu_axi) * (1-2 * nu_axi)) * nu_axi * er_t_axi+E_axi/((1+nu_axi) * (1-2 * nu_axi)) * (1-nu_axi) * ephi_t_axi+E_axi/((1+nu_axi) * (1-2 * nu_axi)) * nu_axi * ez_t_axi
srz_t_axi	Time der. of shear stress global sys. (srz)	E_axi/(1+nu_axi) * erz_t_axi
mises_axi	von Mises stress	sqrt(real(sr_axi)^2+real(sphi_axi)^2+real(sz_axi)^2-real(sr_axi) * real(sphi_axi)-real(sphi_axi) * real(sz_axi)-real(sr_axi) * real(sz_axi)+3 * real(srz_axi)^2)
Ws_axi	Strain energy density	0.5 * (er_axi * sr_axi+ephi_axi * sphi_axi+ez_axi * sz_axi+2 * erz_axi * srz_axi)
tresca_axi	Tresca stress	max(max(abs(s1_axi-s2_axi),abs(s2_axi-s3_axi)),abs(s1_axi-s3_axi))
er_axi	er normal strain global sys.	uorr * r+uor
ephi_axi	ephi normal strain	uor
ez_axi	ez normal strain global sys.	wz
erz_axi	erz shear strain global sys.	0.5 * (uorz * r+wr)
er_t_axi	er_t normal velocity strain global sys.	j * omega_axi * (uorr * r+uor)
ephi_t_axi	ephi_t normal velocity strain	j * omega_axi * uor

ez_t_axi	ez_t normal velocity strain global sys.	j * omega_axi * wz
erz_t_axi	erz_t shear velocity strain global sys.	0.5 * j * omega_axi * (uorz * r+wr)
sr_amp_axi	sr normal stress amp. global sys.	abs(sr_axi)
sz_amp_axi	sz normal stress amp. global sys.	abs(sz_axi)
sphi_amp_axi	sphi normal stress amp.	abs(sphi_axi)
sphi_ph_axi	sphi normal stress phase	180/pi * mod(angle(sphi_axi),2 * pi)
srz_amp_axi	srphi shear stress amp. global sys.	abs(srz_axi)
sr_ph_axi	sr normal stress phase global sys.	180/pi * mod(angle(sr_axi),2 * pi)
sz_ph_axi	sz normal stress phase global sys.	180/pi * mod(angle(sz_axi),2 * pi)
srz_ph_axi	srphi shear stress phase global sys.	180/pi * mod(angle(srz_axi),2 * pi)
er_amp_axi	er normal strain amp. global sys.	abs(er_axi)
ez_amp_axi	ez normal strain amp. global sys.	abs(ez_axi)
ephi_amp_axi	ephi normal strain amp.	abs(ephi_axi)
erz_amp_axi	erphi shear strain amp. global sys.	abs(erz_axi)
er_ph_axi	er normal	180/pi * mod(angle(er_axi),2 * pi)

	strain phase global sys.	
ez_ph_axi	ez normal strain phase global sys.	180/pi * mod(angle(ez_axi),2 * pi)
ephi_ph_axi	ephi normal strain phase	180/pi * mod(angle(ephi_axi),2 * pi)
erz_ph_axi	erphi shear strain phase global sys.	180/pi * mod(angle(erz_axi),2 * pi)
U_ns	Velocity field	
V_ns	Vorticity	
cellRe_ns	Cell Reynolds number	
res_u_ns	Equation residual for u	
res_sc_u_ns	Shock capturing residual for u	
res_v_ns	Equation residual for v	
res_sc_v_ns	Shock capturing residual for v	
beta_r_ns	Convective field, r component	
beta_z_ns	Convective field, z component	
Dm_ns	Mean diffusion coefficient	
da_ns	Total time scale factor	
ar_aco	Local acceleration, r component	
vr_aco	Local velocity, r	

	component
az_aco	Local acceleration, z component
vz_aco	Local velocity, z component
pdB_aco	Pressure (dB)
k_aco	Wave number
normv_aco	Local velocity, norm
norma_aco	Local acceleration, norm
normqs_aco	Dipole source, norm